High-performance adaptive optics control in strong turbulence scenarios for free space optical communication

Commande des systèmes d'optique adaptative pour les communications optiques en espace libre

Thèse de doctorat de l'université Paris-Saclay

École doctorale n°575 : electrical, optical, bio: physics and engineering (EOBE)
Spécialité de doctorat: Physique
Graduate School : Physique. Référent : Institut d'Optique

Thèse soutenue dans les unités de recherche **Université Paris-Saclay, Institut d'Optique Graduate School, CNRS, Laboratoire Charles Fabry, 91127, Palaiseau, France** et **Institute for Communication and Navigation, Deutsches Zentrum für Luft und Raumfahrt (DLR), Allemagne**
sous la direction de **Caroline KULCSÁR**, Professeure des Universités (LCF),
le co-encadrement de **Andrew P. REEVES**, Chercheur (DLR), **Henri-François RAYNAUD**, Maître de Conférences HDR (LCF), **Douglas LAIDLAW**, Chercheur (DLR)

Thèse soutenue à Paris-Saclay le 10 décembre 2025 par

Joana Sofia DO SUL DA MOTA TORRES

Composition du jury

Membres du jury avec voix délibérative

Sihem TEBBANI Professeure, CentraleSupélec, France	Présidente
Carlos CORREIA Chercheur Associé, Université de Porto, Portugal	Rapporteur
Elena MASCIADRI Directrice de Recherche, INAF, Arcetri, Italie	Rapportrice
Szymon GLADYSZ Chercheur, Fraunhofer Institute of Optronics, Ettlingen, Allemagne	Examinateur

THESE DE DOCTORAT

NNT : 2025UPAST150

Contents

Acknowledgements

This thesis would not have been possible without the knowledge and unwavering support of my supervision team. A massive thank you to Caroline, Henri-François and Andrew for all your time, effort and dedication, which have made the physical distance meaningless during the project. Your guidance and mentorship made me strive for higher scientific rigour. Thank you also to Dougie for your support and understanding through the last year of my thesis. To the members of the jury, a special thank you for your time and insightful feedback. The diverse perspectives have been instrumental in refining the final version of this thesis manuscript and the discussions we had will shape my future work. I look forward to any future interactions with each of you.

To the team at LCF: thank you for your hospitality and the engaging lunch discussions. Despite my short stays, your kindness ensured that time was both productive and memorable.

To my colleagues from KN-OSL at DLR, thank you for all the support and encouragement. What a pleasure to be able to continue contributing towards the missions in our institute. A heartfelt thank you to my teammates, past and current, who've all contributed to getting this project to fruition. A special mention to Lisa, for the support and encouragement through the finish line. A special thank you also to Janis and Andrea, I can't wait to celebrate you both as you cross your own approaching finish lines. Shoutout to Ilija, for turning the PhD journey delirium into a total riot. And to Jack and Mareen for the perfectly timed Paris rescue mission.

To my parents, friends and family: I am grateful beyond words for your continued support and belief in me. You have helped me through the lows and cheered on the highs of this journey. To everyone who has ever offered support, a kind word, listening ear, or much needed distraction: thank you, sincerely.

Lastly, thank you to my partner, for seeing me through. You've let me drone on endlessly on the topics I was working on, listening with interest and asking questions I had not thought of before. And of course, thank you to our fluffy companions Gaia and Tejföl, who kept me warm through late nights and continue to be the best alarm clocks every morning.

List of Figures

List of Tables

Table of Notations

Symbol	Meaning	Units
Re	Reynolds number	–
V	Characteristic velocity	m·s^{-1}
L	Characteristic length scale	m
ν	Kinematic viscosity	m^2·s^{-1}
$D_v(r)$	Second-order velocity structure function	m^2·s^{-2}
$v(x)$	Velocity field at position x	m·s^{-1}
r	Spatial separation between two points in space	m
ε	Turbulent kinetic energy dissipation rate per unit mass	m^2·s^{-3}
C_v^2	Velocity structure constant (Kolmogorov constant)	m$^{2/3}$·s^{-2}
l_0	Inner scale of turbulence	m
L_0	Outer scale of turbulence	m
$D_n(r)$	Refractive-index structure function	–
C_n^2	Refractive-index structure constant	m$^{-2/3}$
r_0	Fried coherence diameter	m
θ_0	Isoplanatic angle	rad
τ_0	Greenwood time constant	s
k	Optical wavenumber	rad·m^{-1}
λ	Wavelength of optical radiation	m
h	Altitude above ground level	m
w	High-altitude root-mean-square (rms) wind speed	m·s^{-1}
T	Turbulence strength at ground level	m$^{-2/3}$
$V(h)$	Wind velocity as a function of altitude	m·s^{-1}
V_g	Ground-level wind speed	m·s^{-1}
V_T	Tropopause wind speed	m·s^{-1}
w_s	Satellite slew rate (apparent angular velocity across the sky)	rad·s^{-1}
ζ	Zenith angle	rad
H_T	Height of the tropopause layer	m
L_T	Thickness of the tropopause layer	m
φ	Wind direction relative to the telescope azimuth	rad
f	Temporal frequency	Hz
σ_R^2	Rytov variance, measure of log-amplitude fluctuation strength due to turbulence	–
L	Propagation path length	m

$E(r)$	Complex amplitude envelope of the optical field	a. u.
A_0	Amplitude constant of the complex field	V·m^{-1} or a.u.
W_0	Beam waist radius at the focus ($z = 0$)	m
$W(z)$	Beam radius at distance z	m
z	Axial propagation distance from the beam waist	m
z_0	Rayleigh range	m
$R(z)$	Radius of curvature of the beam's wavefront at distance z	m
$\zeta(z)$	Gouy phase shift	rad
ρ	Radial coordinate in cylindrical coordinates	m
M_{int}	Interaction matrix	–
M_{com}	Command matrix	–
u_k	command vector at iteration k	–
y_k	Wavefront sensor measurement vector at iteration k	–
g	Integrator gain	–
ϕ^{res}	Residual wavefront phase after correction	rad
ϕ	Incoming (uncorrected) wavefront phase	rad
ϕ^{cor}	Corrected phase generated by the deformable mirror	rad
$J_k^d(u_k)$	Discrete-time cost function (performance criterion at step k)	–
N	Deformable mirror influence function matrix	–
P_u	Phase-to-command projection (pseudo-inverse of N)	–
$\hat{\phi}_{k+1\mid k}$	One-step-ahead predicted phase estimate	rad
X_k	State vector of the dynamic model at time k	–
A	State-transition matrix in the state-space model	–
C	Measurement matrix	–
v_k	Process noise vector at time k	–
w_k	Measurement noise vector at time k	–
y_k	Wavefront sensor measurement vector at time k	–
T_s	Sampling period of the AO control loop	s
u_k	Command vector at time k	–

Acronyms

AO	Adaptive optics
ARn	Autoregressive of order n
ARTES	Advanced Research in Telecommunications Systems
ASP	Angular Spectrum Propagation
CL	Closed loop
DLR	German aerospace centre
DLR-KN	Institute for communication and navigation
DM	Deformable mirror
ELT	extremely large telescope
ESA	European space agency
ESO	European southern observatory
FCAS	Future air combat system
FPS	Frames per second
FSOC	Free space optical communication
FT	Fourier Transform
FWHM	Full width at half maximum
GPI	Gemini Planet Imager
HydRON	High thRoughput Optical Network
JAXA	Japan Aerospace Exploration Agency
KIODO	Kirari optical downlinks to Oberpfaffenhofen
Laser	Light amplification by stimulated emission of radiation
LGS	Laser guide star
LCT	Laser communication terminal
LEO	Low-earth orbit
NASA	National aeronautics and space administration
PAT	Pointing, acquisition and tracking
OGS	Optical ground station
OOMAO	Object-Oriented Matlab Adaptive Optics
OSIRIS	Optical Space Infrared Downlink System
QKD	Quantum key distribution
RF	Radio frequency
ScyLight	Strategic Programme Line on Optical and Quantum Communication
SH-WFS	Shack-Hartmann wavefront sensor
SPHERE	Spectro-Polarimetric High-contrast Exoplanet REsearch instrument
TDP-1	Technology Demonstrator Payload 1

THRUST	Terabit-throughput optical satellite system
WFS	Wavefront sensor
xAO	extreme adaptive optics
ZOH	Zero-order hold

ÉCOLE DOCTORALE
Physique et ingénierie :
Electrons, Photons,
Sciences du vivant (EOBE)

Titre : Commande des Systèmes d'Optique Adaptative pour les Communications Optiques en Espace Libre

Mots Clés : communications optiques en espace libre, optique adaptative, turbulence, commande par retour d'état

Résumé : Les communications par satellites devenant limitées par la saturation du spectre radio, les communications en espace libre (FSOC) apparaissent comme la solution pour les prochaines générations de systèmes de télécommunications spatiaux.

Les FSOC permettent des liaisons satellitaires plus sûres et à plus haut débit. Cependant, leurs performances sont limitées par la turbulence atmosphérique, qui déforme le faisceau laser et induit des variations de phase et d'amplitude au niveau du récepteur, réduisant le débit de données. L'optique adaptative (OA), utilisée depuis longtemps en astronomie pour atténuer les effets de la turbulence, emploie des miroirs déformables (DM) pour corriger celle-ci en temps réel à l'aide de mesures d'analyseurs de front d'onde (WFS) filtrées par un algorithme de contrôle. L'OA a été proposée pour les FSOC afin d'améliorer la robustesse des liaisons optiques, mais les boucles d'OA peuvent devenir instables sous forte et rapide turbulence, typique des opérations diurnes. Les techniques de contrôle optimal basées sur des modèles stochastiques peuvent alors anticiper le comportement de la turbulence et améliorer les performances des FSOC.

Cette recherche vise à concevoir, simuler et mettre en œuvre des régulateurs linéaires quadratiques gaussiens (LQG), déjà validés avec succès en astronomie. Les modèles et schémas de contrôle sont adaptés aux FSOC, ciblant les liaisons en orbite basse (LEO). Les profils de turbulence atmosphérique pour une liaison LEO diurne correspondant aux pires conditions au-dessus de la station optique au sol (OGS-OP) du DLR à Oberpfaffenhofen sont utilisés pour simuler les régulateurs LQG à trois élévations. Les simulations incluent les effets de diffraction dus à la propagation de la turbulence afin d'obtenir des effets de scintillation réalistes, et les fonctions de structure de von Kármán sont utilisées pour obtenir les statistiques de turbulence. Le système est décrit par une base zonale avec une phase suréchantillonnée par un facteur deux à l'aide d'une moyenne pondérée sur les bords des sous-pupilles. Dans ce cadre, nous étudions l'impact de la modélisation de la scintillation, de la fréquence de boucle et de l'élévation d'observation sur les performances de l'OA en comparant un contrôleur intégrateur classique et un contrôleur LQG. Le suréchantillonnage des points de phase par un facteur deux a permis d'améliorer les performances de 34,5 % par rapport à une grille suivant la géométrie de Fried. La robustesse des régulateurs LQG face à des erreurs dans le modèle d'élévation a également été évaluée. Les résultats montrent une grande résistance aux imprécisions du modèle, avec des performances systématiquement supérieures à celles de l'intégrateur. Le meilleur régulateur LQG a réduit de manière significative le taux d'erreur binaire, permettant un débit plus élevé avec moins de post-traitement, et a amélioré le taux de clé secrète (SKR) jusqu'à 70 % dans des conditions de faible altitude, forte turbulence et scintillation. Les effets de la scintillation ont été évalués plus en détail pour les liaisons LEO en comparant une propagation géométrique et physique du spectre à 2 et 5 kHz. La propagation physique a introduit plus d'événements d'évanouissement, dégradant la performance globale et démontrant quantitativement le rôle critique de la scintillation dans la simulation FSOC. Cependant, le régulateur LQG à 2 kHz s'est montré plus performant que l'intégrateur à 5 kHz, atténuant efficacement les fluctuations d'intensité. Enfin, une première tentative d'atténuation de la scintillation à l'aide d'une stratégie de remplacement des mesures dégradées a été menée. Bien que peu concluants, les résultats indiquent que les configurations dynamiques méritent d'être approfondies.

En somme, ces travaux montrent que le contrôle prédictif LQG renforce la stabilité et le débit des liaisons FSOC-AO, soutenant la communication quantique européenne et les missions futures.

Title : High-Performance Adaptive Optics Control in Strong Turbulence Scenarios for Free Space Optical Communications

Keywords : free space optical communications, adaptive optics, turbulence, control

Abstract : Current satellite communication is limited by the highly saturated radio frequency spectrum. Free Space Optical Communication (FSOC) enables higher-throughput data links to satellites. However, its performance is limited by atmospheric turbulence, which distorts the laser beam and induces scintillation at the receiver, reducing data rates. Adaptive optics (AO), widely used in astronomy to mitigate turbulence effects, employs Deformable Mirrors (DMs) for real-time correction using measurements from Wavefront Sensors (WFSs) and a control algorithm. AO has been proposed for FSOC to enhance link robustness, but AO loops can become unstable under rapidly varying turbulence typical of daytime operations. Optimal control techniques based on stochastic models can anticipate turbulence behaviour and improve FSOC performance.

This research aims to design, simulate, and implement high-performance AO control strategies, starting from Linear Quadratic Gaussian (LQG) regulators successfully tested in astronomy. Models and control schemes were adapted for FSOC, with emphasis on low-Earth orbit (LEO) links. Diffraction effects were included for accurate simulation. A zonal-based approach was chosen, naturally encoding frozen flow as wind translation. Theoretical covariances from the von Kármán structure function were used to generate auto-regressive turbulence models. A predictive control library was developed in Python and integrated into DLR's ELSiE simulator. The phase grid was oversampled by a factor of two using weighted averaging across subaperture edges. A horizontal testbed link was used in preliminary simulations comparing tuned LQG regulators with a tuned integrator. Under identical conditions, coupling efficiency dropped by 56.4% for the integrator and 69.8% for the LQG controller when scintillation was included. These results provide the first quantitative evidence of the critical role of scintillation in FSOC simulations.

Atmospheric turbulence profiles for a worst-case daytime LEO link over DLR's Oberpfaffenhofen Optical Ground Station (OGS-OP) were used to simulate LQG regulators at three elevations. Oversampling phase points by a factor of two improved performance by 34.5% compared to a simplified Fried geometry grid. The robustness of LQG regulators to elevation model mismatch was also evaluated. Results show high resilience to model inaccuracies, consistently outperforming the integrator. The best LQG regulator significantly reduced the bit error rate (BER), enabling higher throughput with less post-processing, and improved the secret key rate (SKR) by up to 70% under low-elevation, strong-turbulence, and scintillation conditions. Scintillation effects were further assessed for LEO links by comparing geometric and angular spectrum propagation at 2 and 5 kHz. Physical propagation introduced more fade events, degrading overall performance, yet the LQG regulator at 2 kHz outperformed the integrator at 5 kHz, effectively mitigating intensity fluctuations. Finally, an initial attempt to mitigate scintillation using a degraded-measurement replacement strategy was conducted. Although inconclusive, the results indicate that dynamic configurations warrant further investigation.

Overall, this work demonstrates that FSOC-AO systems using predictive LQG control can substantially enhance link stability and throughput, supporting Europe's secure quantum communication infrastructure and enabling higher data rates for next-generation missions such as HydRON and EAGLE-1.

ÉCOLE DOCTORALE
Physique et ingénierie :
Electrons, Photons,
Sciences du vivant (EOBE)

Résumé en français

Introduction

Les communications radiofréquence (RF) deviennent moins adaptées aux besoins grandissants de connectivité mondiale. Les liaisons RF nécessitent une séparation stricte des fréquences. Le spectre est saturé et fortement réglementé. La disponibilité de la bande passante est donc limitée, et les débits de données ne peuvent suivre les exigences croissantes de la demande. De plus, les antennes RF sont volumineuses et sensibles aux interférences, ce qui les rend inefficaces pour les systèmes de communication à haut débit. Ces contraintes freinent considérablement le développement d'une infrastructure mondiale de communication à haute vitesse, notamment dans les régions où les réseaux terrestres sont peu fiables ou impossibles à déployer.

Les communications optiques en espace libre (FSOC, pour *Free Space Optical Communications*) permettent de contourner ces limitations. En utilisant la lumière au lieu des ondes radio, les liaisons FSOC peuvent atteindre des débits de données supérieurs de plusieurs ordres de grandeur tout en opérant dans des bandes spectrales non réglementées. Les faisceaux optiques, grâce à leur faible divergence, rendent l'interception difficile, ce qui accroît la sécurité des communications. De plus, leur intégration avec la distribution quantique de clés (QKD, *Quantum Key Distribution*) offre un chiffrement au niveau physique capable de détecter toute tentative d'écoute. Les constellations de satellites FSOC peuvent ainsi constituer l'épine dorsale d'un réseau de communication véritablement mondial, garantissant un accès Internet sécurisé et à haut débit jusque dans les régions les plus isolées.

La commande en OA pour les FSOC

Malgré ses avantages, la performance en FSOC est fortement affectée par la turbulence atmosphérique. Lorsqu'un faisceau optique se propage dans l'atmosphère, les variations de température induisent des fluctuations de l'indice de réfraction qui déforment le front d'onde. Ces distorsions dégradent sévèrement la qualité du lien. L'optique adaptative (OA) est une technique clé pour compenser ces effets en temps réel (Figure 1). La boucle d'asservissement en OA a pour objectif de rejeter les perturbations en compensant les déformations du front d'onde grâce à un miroir déformable commandé à partir des mesures d'un analyseur de front d'onde (WFS, pour *WaveFront Sensor*). Le retard de boucle typique est de deux périodes d'échantillonnage (une période d'intégration pour permettre la mesure de front d'onde et une autre pour l'ensemble des calculs).

Les systèmes d'OA classique reposent généralement sur une simple loi de commande à action intégrale pour piloter les miroirs déformables. Bien que cette approche soit efficace en astronomie, où les conditions de turbulence sont faibles à modérées, elle peut s'avérer insuffisante en conditions de jour où la turbulence est forte et de dynamique temporelle élevée. En particulier, lors de liaisons descendantes à faible élévation avec des satellites LEO (*Low Earth Orbit*), la scintillation entraîne des fluctuations d'intensité et dégrade les mesures de l'analyseur de front d'onde. Ceci vient s'ajouter à l'erreur temporelle induite par la présence de retards dans la boucle d'asservissement. Les commandes prédictives telles que la commande linéaire quadratique gaussienne (LQG) permettent de limiter l'effet de ce retard temporel en prédisant la phase turbulente à partir de modèles dynamiques stochastiques grâce à un filtre de Kalman. Le critère de commande optimale étant la variance de la phase résiduelle après correction, la commande LQG gère mieux la propagaton du bruit de mesure dans la boucle tout en prédisant le front d'onde, ce qui améliore le couplage dans la fibre.

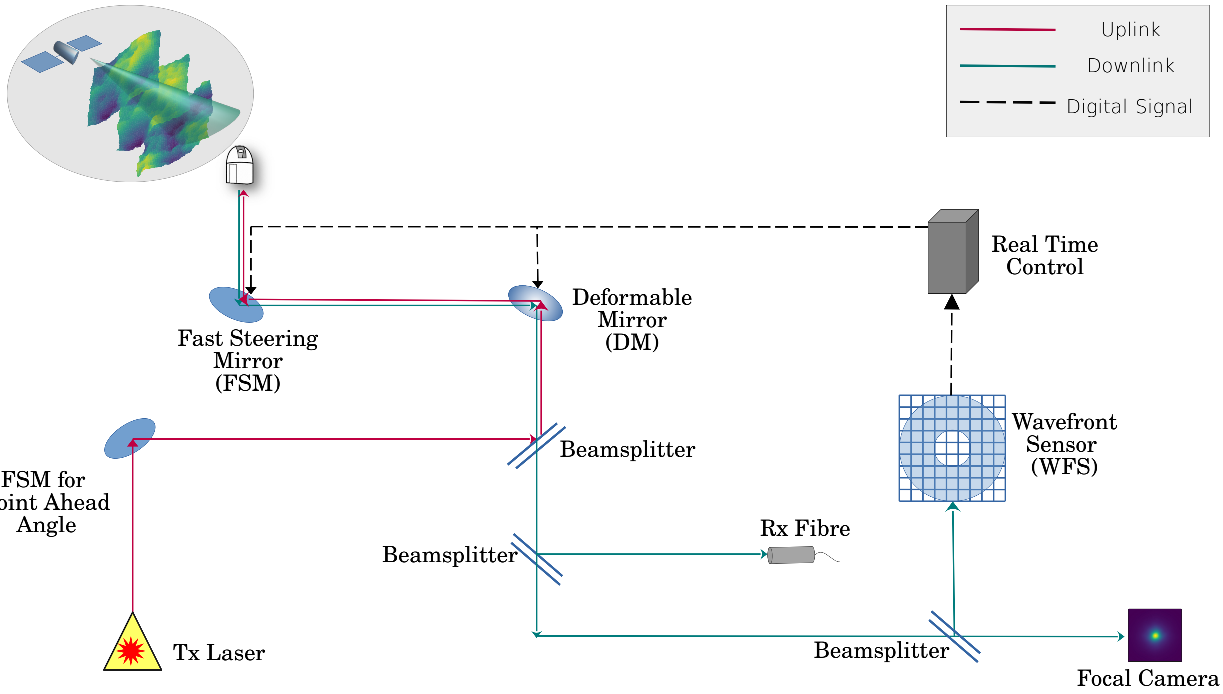

Figure 1 : Schéma d'un système FSOC avec OA montrant les chemins aller, retour et la boucle d'asservissement de l'OA.

Les commandes prédictives apparaissent donc essentielles pour maintenir des liaisons FSOC stables et à haut débit dans des conditions atmosphériques réalistes et contraignantes, telles que celles rencontrées lors de liaisons satellites en orbite basse (LEO).

Les travaux présentés dans cette thèse s'appuient sur les résultats de recherche publiés récemment (Prengère et al. 2020) sur la commande LQG en base zonale pour l'OA, et l'étendent à des applications FSOC, en considérant pour la première fois des liaisons LEO à faible élévation et sous forte scintillation. L'approche LQG zonale a été choisie pour sa capacité à préserver les structures spatio-temporelles de la turbulence, avec un avantage spécifique pour les effets dominants en FSOC de type « flux gelé » dus à la vitesse du vent apparent créé par le mouvement orbital. Dans ces conditions, la perturbation est donc principalement translatée entre deux instants de correction et la prédiction devient cruciale. Un package Python a été développé pour faciliter la conception et la synthèse de régulateurs LQG, intégré à un outil de simulation d'OA existant. L'environnement de simulation résultant a été validé par comparaison avec des résultats publiés. Différentes configurations LQG ont été simulées et comparées à un intégrateur dont le gain a été bien réglé. L'inclusion de la diffraction dans l'environnement de simulation a également été évaluée.

Synthèse LQG et performance en propagation physique

Les simulations initiales ont été menées avec un régulateur LQG zonal utilisant des matrices de covariance obtenues par résolution des équations de Yule-Walker pour un modèle autorégressif d'ordre deux (Correia et al. 2015 ; Prengère et al. 2020), incluant un suréchantillonnage de la phase (Prengère et al. 2020). Ce régulateur, noté LQG22 dans la suite, a été testé sur un lien horizontal soumis à une turbulence intense dans un contexte de lien horizontal et comparé à un intégrateur, avec et sans prise en compte de la diffraction, soit en propagation physique (méthode du spectre angulaire) ou en propagation géométrique. Il a été démontré (voir la figure 2) que même si le régulateur LQG surpassait l'intégrateur dans le cas géométrique, il devenait seulement à peine meilleur dans le cas avec propagation physique. L'inclusion des effets de scintillation entraîne comme on peut le voir une chute spectaculaire de l'efficacité de couplage. Le fait que le régulateur LQG soit plus affecté que l'intégrateur est dû à un choix de modèle qui n'a pas été calé sur les données. Ces résultats démontrent en tout état de cause que négliger la scintillation dans les simulations d'OA pour les FSOC conduit à des évaluations bien trop optimistes des performances de correction.

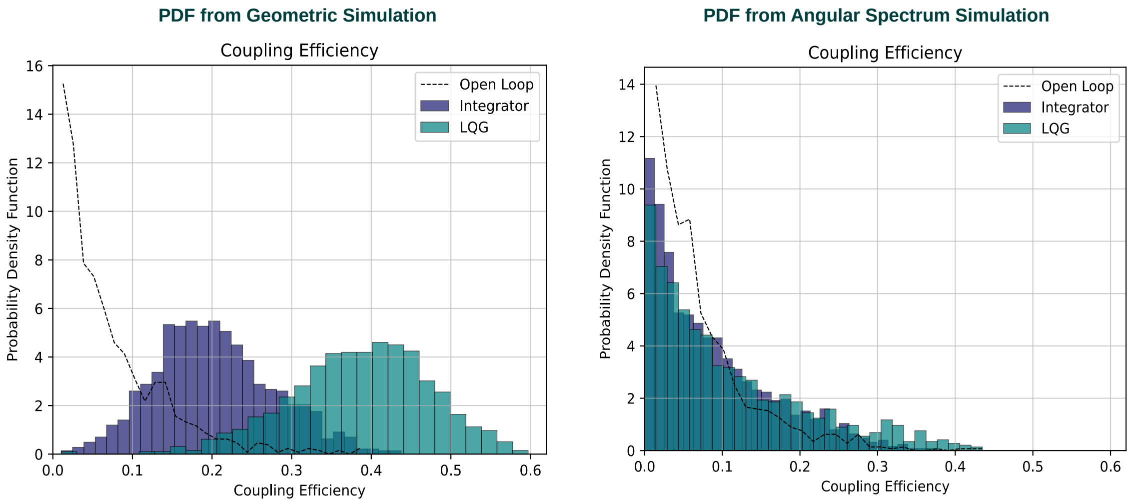

Figure 2 : Résultats de simulation pour un lien horizontal : histogrammes de l'efficacité de couplage corrigée par OA pour un intégrateur et un régulateur LQG en propagation géométrique (à gauche) ou physique (à droite).

Des simulations réalistes ont ensuite été menées pour une liaison LEO (HyDRON) passant au-dessus de l'OGS-OP, la station sol de DLR, correspondant au pire cas diurne (Torre et al. 2024). Trois régulateurs LQG ont été synthétisés avec de potentielles améliorations de modèle de turbulence et de représentation de la phase : un modèle autorégressif d'ordre 1, un modèle autorégressif d'ordre 2 et un modèle autorégressif d'ordre 2 avec une phase représentée dans le filtre de Kalman sur une grille deux fois plus fine. Ces trois régulateurs ont été comparées à un intégrateur pour un scénario de très forte turbulence (cas d'une élévation de 30°) pour décider de la synthèse à retenir pour la suite dans l'ensemble des scénarios. Le suréchantillonnage de la grille améliore le couplage moyen de 1,38 ± 0,02 dB et réduit de 85 % les occurrences d'affaiblissement à –3 dB. Étendre la grille au-delà de la pupille apporte une très légère amélioration supplémentaire. La finesse de l'espace zonal utilisé pour représenter la phase dans le filtre de Kalman est donc un élément essentiel dans la conception de régulateurs LQG d'OA en base zonale pour les FSOC, notamment pour les liaisons LEO à faible élévation.

La performance de ce régulateur combinant suréchantillonnage et extension au-delà de la pupille, et noté LQG22 dans la suite, a ensuite été évaluée pour les deux autres scénarios (élévations de 50° et 80°), voir la figure 3. Le régulateur LQG22 a surpassé l'intégrateur dans tous les scénarios. Pour le cas le plus difficile (élévation de 30°), le nombre d'affaiblissements à –3 dB est réduite de 93 % et leur durée moyenne de 45 %, tandis que les affaiblissements plus profonds sont totalement compensés, voir le tableau 3. Ces résultats originaux confirment la performance de la commande LQG pour les liaisons LEO à faible élévation.

La question de la robustesse à une erreur de modèle se pose, et un régulateur LQG synthétisé avec des *a priori* pour le cas de basse élévation a été déployé également sur les élévations moyenne et haute. Là encore, les performances sont meilleures qu'avec l'intégrateur, comme montré en figure 4.

Impact de la scintillation

Concernant l'impact de la scintillation sur le scénario de liaison descendante LEO, une étude a été effectuée entre la propagation géométrique et la propagation physique pour le cas de basse élévation. Il a été montré que cet impact provient vraisemblablement des variations d'intensité induites sur le WFS Shack-Hartmann,

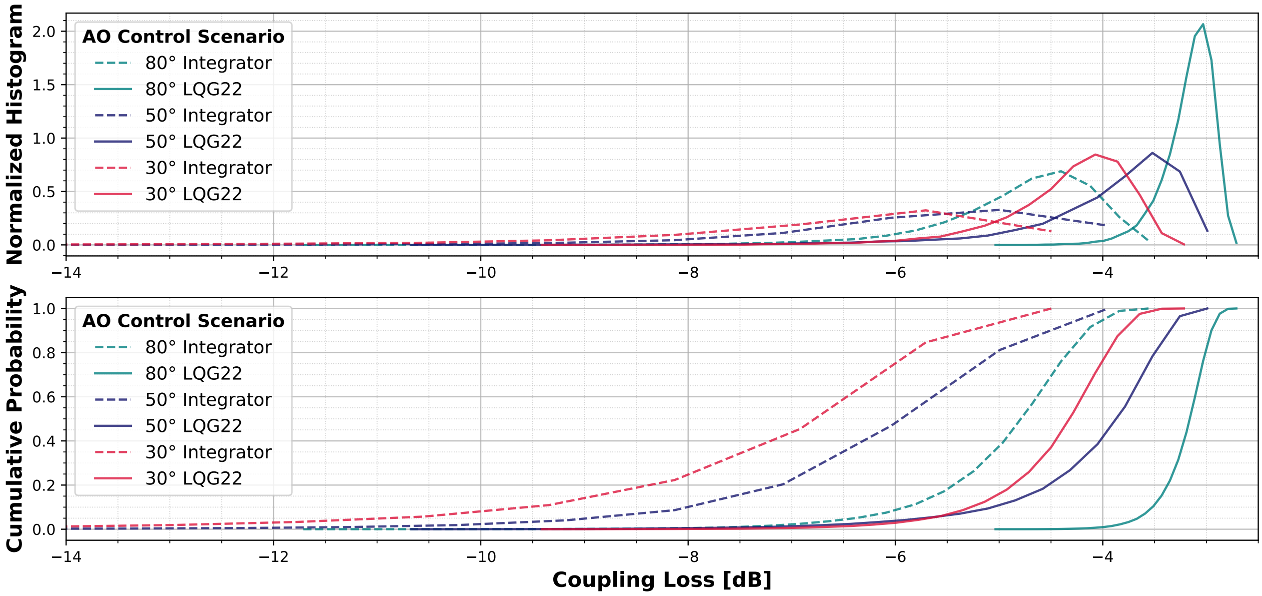

Figure 3 : Histogrammes normalisés (haut) et probabilités cumulées (bas) comparant LQG22 et intégrateur à différentes élévations simulées.

Table 3 : Coupling loss and fading statistics for LQG22 on SimID 80° (SE±0.01 dB).

	Coupling Loss (dB)		−3 dB		−6 dB		−10 dB	
	Mean	**Med.**	**F/s**	**ms**	**F/s**	**ms**	**F/s**	**ms**
SimID 80°								
Integrator	−4.80	−4.64	3	1.76	< 1	1.00	0	–
LQG22	−3.17	−3.12	0	–	0	–	0	–
SimID 50°								
Integrator	−5.69	−5.42	19	2.35	3	1.84	< 1	1.88
LQG22	−3.96	−3.73	6	2.39	< 1	0.63	0	–
SimID 30°								
Integrator	−6.65	−6.15	42	1.86	15	1.33	4	1.08
LQG22	−4.35	−4.21	3	1.02	0	–	0	–

entraînant une dégradation des mesures. Ces résultats vont de pair avec les résultats théoriques (Fried et al. 1992). Une amélioration potentielle supplémentaire a donc été testée, visant spécifiquement à contrebalancer l'effet négatif de la scintillation en remplaçant simplement les mesures dégradées par la prédiction donnée par le filtre de Kalman. Cette méthode n'a montré aucune amélioration notable, mais il faudrait étudier une modification de la méthode pour permettre de tenir compte des mesures dégradées au niveau du gain de Kalman.

L'hypothèse selon laquelle il suffirait d'augmenter la fréquence de boucle pour se passer de commande prédictive a également été étudiée. Pour évaluer cette affirmation, la fréquence de boucle a été augmentée de 2 à 5 kHz, avec et sans effet de scintillation. Comme attendu, une augmentation de la fréquence à 5 kHz améliore la performance pour tous les régulateurs. Cependant, le régulateur LQG augmente considérablement le couplage médian et réduit le nombre d'affaiblissements, sans plus aucun affaiblissement inférieur à -3 dB par rapport au niveau moyen dans le cas à 5 kHz. Pour l'intégrateur, des affaiblissements à plus de -3 dB sont encore largement présents. Il est intéressant de noter que le régulateur LQG à 2 kHz surpasse l'intégrateur à 5 kHz, montrant qu'une simple augmentation de la fréquence de boucle ne suffit pas à compenser l'effet de la scintillation. Ces résultats sont cohérents avec des résultats de longue date en OA astronomique selon lesquels le déploiement d'un régulateur LQG améliore la performance sans qu'il soit nécessaire d'augmenter

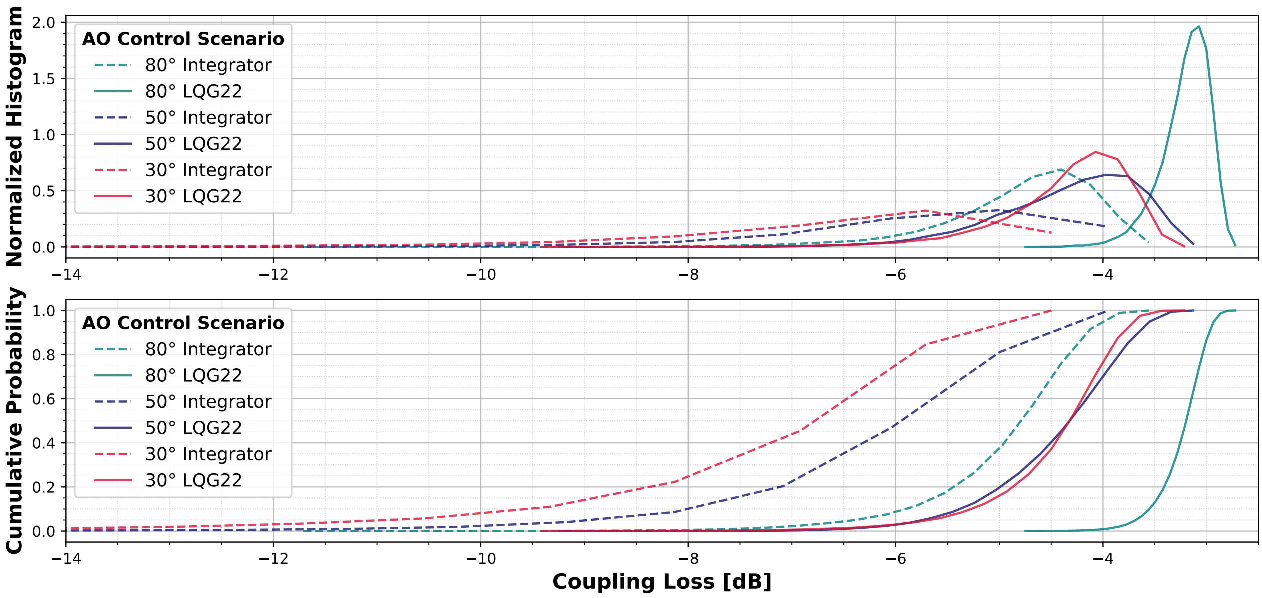

Figure 4 : Régulateur LQG22 synthétisé avec les *a priori* du cas SimID 30° comparé avec l'intégrateur pour les scénarios SimID 50° et SimID 80°.

la fréquence de boucle (Conan et al. 2011). Cela est évidemment donc vrai également pour l'efficacité de couplage dans les simulations de propagation géométrique, comme on peut le voir dans la figure 5, et également dans (Robles et al. 2022). Il a donc été démontré que même avec une boucle fonctionnant à 5 kHz, le recours à un régulateur LQG présente des avantages significatifs.

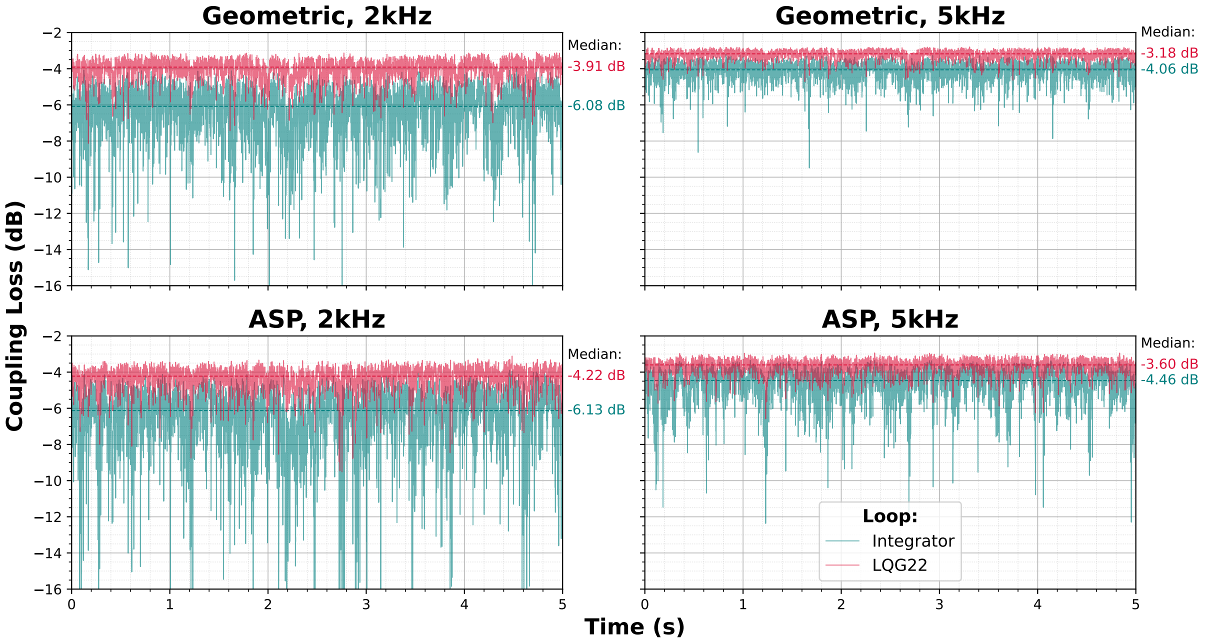

Figure 5 : Comparaison des pertes de couplage entre un intégrateur réglé (bleu) et LQG22 (rouge) pour SimID 30° à 2 et 5 kHz, avec les méthodes de propagation géométrique et de spectre angulaire.

Une analyse des statistiques de la phase a également été effectuée. Les spectres de puissance temporels de la turbulence simulée en boucle ouverte ont été calculés pour les cas d'élévation basse et haute, avec et sans scintillation. Il a été montré que l'inclusion de la scintillation provoque une déviation du spectre de puissance temporel par rapport au cas géométrique aux hautes fréquences, effet particulièrement marqué pour la basse élévation. En outre, la différence quadratique entre les points de l'écran de phase a été comparée à la fonction de structure de von Kármán. Il a été constaté que le cas de basse élévation avec scintillation s'écarte de la loi de décroissance théorique de Kolmogorov et la dépasse largement aux hautes fréquences spatiales.

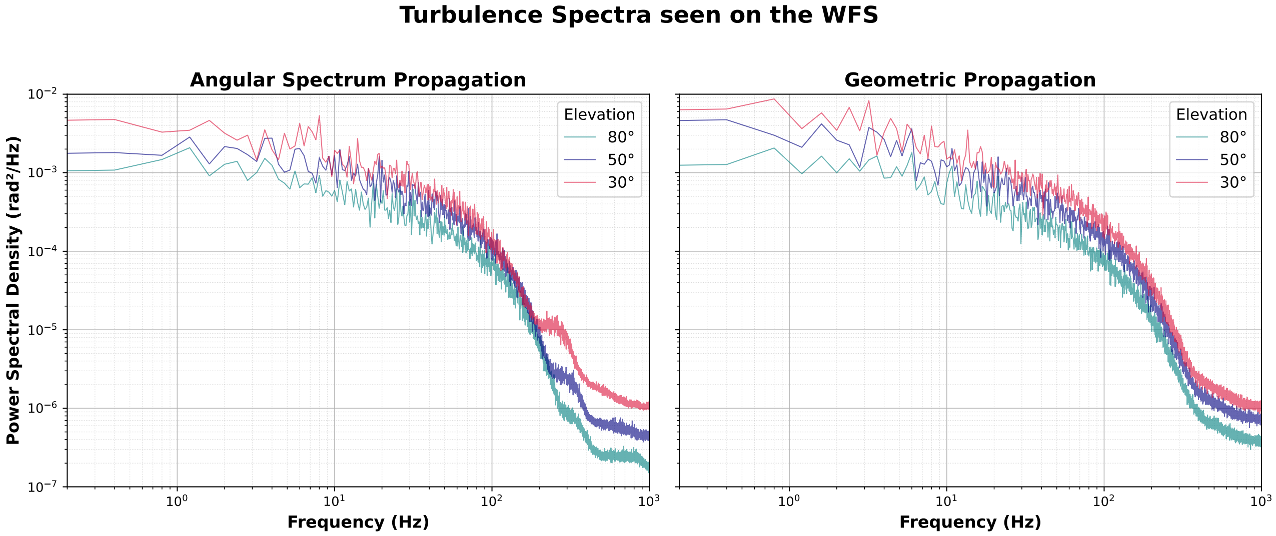

Figure 6 : Densité spectrale de puissance pour toutes les élévations considérées, en propagation par spectre angulaire (gauche) et en propagation géométrique (droite).

Cette analyse a été complétée par une étude sur les mesures de front d'onde afin d'évaluer l'implication de l'utilisation d'un analyseur Shack-Hartmann en présence de forte scintillation. Une comparaison a été faite entre mesures en boucle ouverte et reconstruction de phase. Il a été observé que les fluctuations d'intensité dues à la diffraction affectent principalement la reconstruction de phase aux basses élévations, entraînant une erreur accrue. Ces résultats confirment l'hypothèse selon laquelle les fluctuations d'intensité dues à la diffraction par propagation en spectre angulaire sont les plus critiques aux faibles élévations.

Impact sur les canaux de communication

L'impact d'un régulateur LQG pour les canaux de communication en termes de BER (*Bit Error Rate*) est ici abordé pour la première fois, tant pour les canaux classiques que quantiques. Pour le canal classique, il a été montré que le déploiement du régulateur LQG permet une diminution plus rapide et très importante du BER avec l'augmentation du SNR (figure 7) par rapport à l'intégrateur, atteignant un niveau de BER dit « quasi nul » avant correction d'erreur, ce qui réduit considérablement la dépendance au post-traitement. Concernant l'impact potentiel sur le canal de communication quantique, il a été constaté que le déploiement d'un régulateur LQG permet une amélioration modeste du Quantum-BER (QBER), mais qui entraîne de fait une amélioration très significative du SKR (*Secret Key Rate*), avec une augmentation du débit de clé de 70 % (voir le tableau 4). Il s'agit d'une première étape fondamentale vers la mise en œuvre du QKD (*Quantum Key Distribution*) en observation réelle avec des satellites LEO, où les budgets de liaison stricts devraient limiter la capacité quantique. Ces études suggèrent que les applications QKD en FSOC bénéficieront fortement du déploiement d'une OA avec régulateur LQG.

Table 4 : Comparaison des performances QBER et SKR entre les régulateurs LQG et intégrateur, obtenue avec la simulation et la méthodologie décrites dans (Häusler et al. 2023).

SimID 30°	QBER (%)	SKR (kbit/s)
Intégrateur	0,793	24,84
LQG22	0,779	42,26

Conclusion et perspectives

Dans le contexte des liaisons descendantes de satellites LEO, le suréchantillonnage de la grille de phase s'est avéré être l'amélioration de modèle la plus significative. Dans le cadre de ce travail, seul un suréchantillonnage par un facteur 2 a été envisagé. Cela augmente le nombre de points de phase et donc la charge

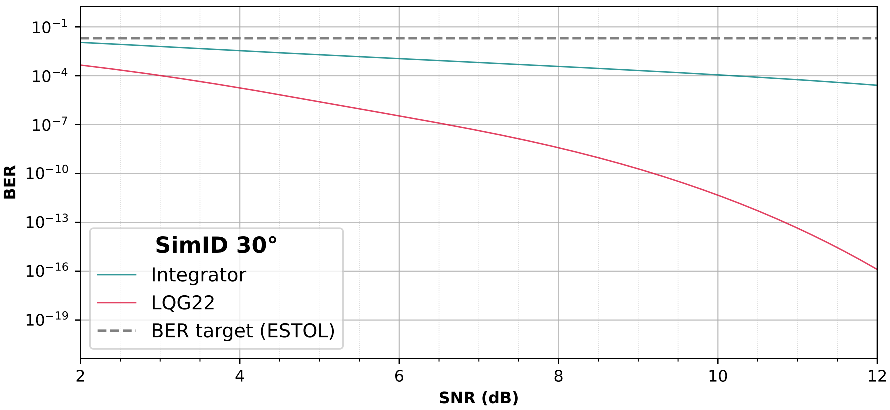

Figure 7 : BER en fonction du rapport signal-bruit (SNR) pour l'intégrateur et le régulateur LQG, avec la cible BER issue d'ESTOL (European Space Agency 2023) indiquée pour référence en tirets.

de calcul des matrices. Un suréchantillonnage plus élevé pourrait être bénéfique et mérite une étude plus approfondie du compromis performance-temps de calcul. Outre les améliorations de modèle proposées, une stratégie de remplacement a été testée, consistant à remplacer les mesures dégradées par leur prédiction fournie par le filtre de Kalman. Cela n'a pas conduit à une amélioration notable des performances.

Les résultats du régulateur LQG pour l'OA dans le cadre des FSOC en liaisons descendantes LEO illustrent une robustesse accrue face aux affaiblissements et une amélioration du couplage médian. Ces améliorations importantes motivent les étapes vers la démonstration en laboratoire puis en conditions réelles. Alors que les conditions de laboratoire sont contrôlées, une expérimentation avec un LQG basé sur un modèle en Zernique a par exemple été réalisée récemment (Robert et al. 2025), les conditions ciel varient elles rapidement. Les régulateurs LQG considérés ici reposent sur des paramètres invariants dans le temps avec un critère de commande à horizon infini (variance de phase résiduelle), permettant l'utilisation d'un gain de Kalman asymptotique sans perte d'optimalité. En pratique, l'évolution des conditions turbulentes nécessite des mises à jour régulières du modèle d'état pour maintenir des performances élevées. Un régulateur LQG autonome (avec mises à jour automatiques) a par exemple été validé avec succès sur le GTC (Gran Telescopio Canarias) sur le système GTCAO (Galland et al. 2024 ; Marquis et al. 2025). L'implémentation d'une mise à jour régulière des modèles a ainsi déjà été testée dans d'autres conditions et est donc une perspective logique à ce travail.

Dans les applications LEO, l'élévation joue un rôle crucial sur les performances de la commande en OA : à mesure que l'élévation diminue, la perte de couplage médian augmente et le nombre d'affaiblissements croît. L'inclusion de la scintillation dans les simulations s'est révélée particulièrement impactante aux faibles élévations. Afin d'évaluer la robustesse de la performance à une erreur de modèle, il a été montré que même avec des *a priori* d'élévation incorrects (calculés sur la base d'une élévation de 30°), le régulateur LQG surpassait systématiquement l'intégrateur. La mise à jour des modèles devrait donc s'effectuer en bénéficiant de cette robustesse intéressante.

Les simulations numériques présentées ici et les améliorations de performance obtenues par le régulateur LQG en termes de pertes de couplage constituent des preuves convaincantes pour poursuivre vers la validation sur banc, puis en conditions réelles. Les futurs développements devraient commencer par une validation en laboratoire de l'intégration du régulateur LQG dans le contrôleur temps réel à DLR. Cette validation initiale devrait permettre une intégration fluide dans l'OGS-OP, avec pour objectif final la réalisation de liaisons satellites performantes. Une validation en ciel réel devrait ainsi confirmer davantage le rôle essentiel de la commande prédictive en OA pour les FSO, notamment pour permettre des communications sécurisées via le QKD en soutenant des taux élevés de génération de clés secrètes. D'autres applications pourraient également être intéressées par la synthèse LQG proposée dans ce mémoire, telles que l'imagerie satellitaire ou le suivi des débris spatiaux.

En définitive, le travail présenté ici apporte des preuves solides que les FSOC avec une OA implémentant une commande LQG a un fort potentiel pour aider l'Europe à sécuriser son infrastructure de communication spatiale grâce au QKD et à permettre des débits de données plus élevés pour la prochaine génération de missions spatiales stratégiques telles que HyDRON (Vasko et al. 2022) et EAGLE-1 (Calistro-Rivera et al. 2024).

Chapter 1

Introduction

1.1 Context, state-of-the-art and motivation

Today's increasingly interconnected global landscape has resulted in surging demand for high-capacity communication links and robust networks. From mundane tasks to critical services, communication systems play a fundamental role in the contemporary world. Internet access has become an essential tool to support health, education, career, economy and leisure activities. Moreover, robust communication networks are especially critical in times of crisis. During natural disasters and humanitarian emergencies, ground infrastructure is often affected, compromising communications. It is also important to note that it is not always possible to develop a reliable ground infrastructure, whether due to political, socio-economical reasons or terrain conditions. As a result, a significant percentage of the population is still without internet access (Figure 1.1).

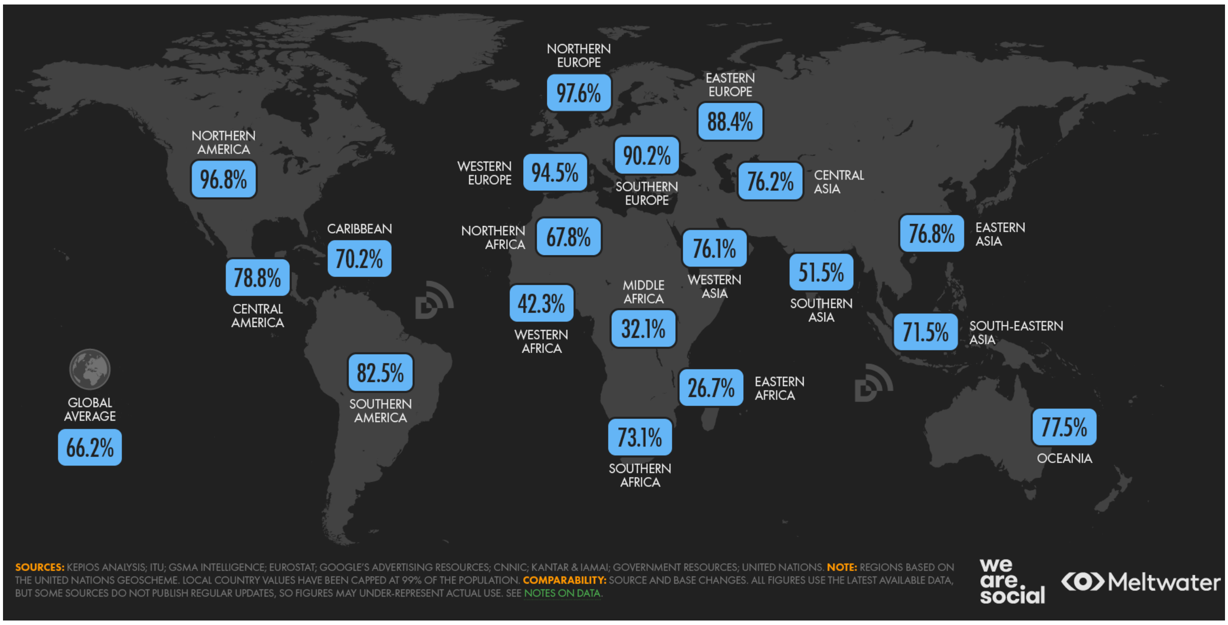

SOURCES: KEPIOS ANALYSIS; ITU; GSMA INTELLIGENCE; EUROSTAT; GOOGLE'S ADVERTISING RESOURCES; CNNIC; KANTAR & IAMAI; GOVERNMENT RESOURCES; UNITED NATIONS. **NOTE:** REGIONS BASED ON THE UNITED NATIONS GEOSCHEME. LOCAL COUNTRY VALUES HAVE BEEN CAPPED AT 99% OF THE POPULATION. **COMPARABILITY:** SOURCE AND BASE CHANGES. ALL FIGURES USE THE LATEST AVAILABLE DATA, BUT SOME SOURCES DO NOT PUBLISH REGULAR UPDATES, SO FIGURES MAY UNDER-REPRESENT ACTUAL USE. SEE NOTES ON DATA.

Figure 1.1: Map displaying percentage of individuals using the internet, data reported in January of 2024. (Credit: DataReportal, Meltwater)

Reports from the GSMA Intelligence state that close to 400 million people remain excluded from the infrastructure required to provide internet access, adding that improvements are likely dependant on a major technological shift (GSMA 2023). Moreover, the growing bandwidth needs cannot be addressed on current technology. Addressing these issues in a sustainable way is only possible by building a global communication network that ensures connectivity to even the most remote locations. Global coverage can be achieved with the use of satellite networks. Free space optical communication (FSOC) is an enticing way forward.

In present day, satellite communication mostly relies on radio frequency (RF). However, RF signal separation is only possible using different frequencies and the RF spectrum is increasingly congested and heavily regulated, whilst also not supporting higher bandwidth connection. FSOC-enabled satellite links could provide real-time, high-speed communication that supports the ever growing bandwidth needs of modern society. By leveraging the use of FSOC technology, low-Earth orbit (LEO) satellite constellations can achieve unprecedented data rates and become a backbone to a global connectivity solution. Additionally, optical communications have the potential to enable quantum encryption, which paired with strict Pointing, Acquisition and Tracking (PAT) requirements make it not only difficult to intercept but also possible to flag eavesdropping with schemes like quantum key distribution (QKD) (Häusler et al. 2024). Europe has dedicated efforts onto Eagle-1, a LEO mission aiming to be the first space-based quantum key distribution system (Fuchs et al. 2023). It will initially use the optical ground station (OGS) DLR-KN, presently being upgraded in order to support this mission (Figure 4.3).

Figure 1.2: The Optical Ground Station at DLR-KN, Oberpfaffenhoffen. (Credit: DLR)

Space agencies all over the world have released specifications (ESA 2023) and reports (NASA 2019) contemplating FSOC links for applications like global connectivity and communication systems for a variety of airbourne objects. The European Space Agency (ESA) has been developing HydRON (High thRoughput Optical Network) (Vasko et al. 2022), a project within the Advanced Research in Telecommunications Systems (ARTES) 4.0 (ESA 2020) Strategic Programme Line on Optical and Quantum Communication (ScyLight) aiming towards global connectivity supported by optical feederlinks. Kepler Communications, TESAT-Spacecom and Airbus Defence and Space have partnered to develop a LEO satellite network that is expected to support the HydRON vision (TESAT 2024). The National Aeronautical and Space Administration (NASA) issued a report with plans for low-Earth-orbit (LEO) commercialization relying FSOC links for communication with varied space systems (NASA 2019). Airbus constellation OneAtlas counts both optical and radar satellites. It is mostly used for Earth Observation and is expected to help support the communication cloud needs of the Future Air Combat System (FCAS) program, an European initiative led by Germany, France and Spain (Airbus Defence and Space 2020). SpaceX's Starlink constellation mostly operates in Ku Band, although including optical terminals for inter-satellite links. Beyond the space sector, publicly traded tech companies such as Alphabet (Taara 2024) and Amazon (Amazon 2024) have programs dedicated to FSOC and/or planned satellite constellations, further contributing for R&D acceleration specifically in the FSOC field.

1.1.1 A brief background on Free Space Optical Communication (FSOC)

In 1960, Theodore H. Maiman successfully demonstrated the first laser, standing for "light amplification by stimulated emission of radiation" (Maiman 1960). This invention marked a significant contribution to the field of optics, leading to groundbreaking discoveries in a varied array of applications, including communications, at a time of significant geo-political tension. This drove technological competition, particularly between the United States and the Soviet Union. Finding new, fast and secure communication methods was paramount to military operations and intelligence gathering, and FSOC had the potential to address these concerns. In early 60s, russian researchers made significant contributions to the field with books on the propagation of waves through random and turbulent media (Chernov 1960; Tatarskij 1961). In the second half of the decade, an extensive study on processing optical images propagated through the atmosphere was published, relying on the calculations and assumptions taken by Tatarskij and Chernov (Harger 1967). Initial theoretical studies and consequent discussions can be found on the IEEE Proceedings Archive through the decade. These focused particularly on optical propagation without resorting to physical cables and listed both potential benefits and challenges of the technology, with turbulence being a highlighted difficulty to overcome (Taylor et al. 1966; Miller et al. 1966; Strohbehn 1968). Historical evidence points to both sides of the Iron Curtain actively researching FSOC throughout the 60s and 70s (Gaddis 2006; Andrews et al. 2005). In 1965, a first demonstration of a spacecraft-to-Earth optical downlink was carried out during the Gemini 7 mission, with the unclassified reports stating the experiment was successful, but partially hindered by ground technological problems and cloud coverage (Gemini VII Mission Evaluation Team 1966). This marked the first successful demonstration of laser communications in space. Later, an uplink was succesfully demonstrated using a laser with the Starlab project (Koepf et al. 2002). Early systems were very significantly affected by atmospheric influence, and practical use was limited to specific military applications. Beyond military use, global interest slowly shifted onto fiber optics systems. At the time, this solution presented a more stable, efficient method of data transmission without facing the losses caused by atmospheric turbulence. Continued advances in laser technology and amplifiers for fiber systems further contributed to making fibre optics the primary choice for terrestrial global communication networks.

FSOC R&D saw significant resurgence in the early 2000s. In 2006, DLR in cooperation with the JAXA successfully demonstrated an optical satellite downlink in the scope of the KIODO project (Kirari Optical Downlinks to Oberpfaffenhofen), which constituted a very important stepping stone into verifying optical data transfer (Perlot et al. 2007), paving the way to other important projects like the Terabit-throughput optical satellite system technology (THRUST) project, which established two world records for optical bandwidth (Poliak et al. 2018). DLR has also significant contributions to the space segment of FSOC, for instance with OSIRIS (Optical Space Infrared Downlink System) (Rödiger et al. 2021), an optical terminal developed for small satellites, research that contributed to LCT (Figure 1.4) which has been used in several satellite missions since.

Despite the successes, propagating a laser through the atmosphere exposes the light to several adverse physical effects such as attenuation, scattering and especially turbulence induced distortions. Common weather phenomena like cloud coverage, fog and rain disrupt the line of sight and render the link impossible at that time and location. This problem can easily be mitigated by carefully choosing locations for OGSs that are uncorrelated in terms of historic weather data in such a way that ensures ground to network continuous uptime. A caveat to consider is that optimal OGS locations in the context of FSOC happen to be near urban centers, where ground optical infrastructure is the most developed, in order to ensure efficient data distribution. Ultimately this means the adverse effects from atmospheric turbulence are not avoidable and instead need to be actively mitigated.

1.1.2 Wavefront correction with Adaptive Optics (AO)

Adaptive optics (AO) is a technique idealized in 1953 by Horace Babcock for correcting the phase induced distortions on astronomical imaging (Babcock 1953). This idea was then further supported by Linnick in 1957 (Linnik 1957), who also introduced the concept of a continuous deformable surface. Whilst both Babcock and Linnik had incredible foresight, it was simply not possible to manufacture such advanced optical components at the time. It wouldn't be until mid to late 70s when deformable mirrors (DMs) and wavefront sensors (WFSs) became a reality and initial successful laboratory demonstrations could take place (Pearson 1976). Initial systems came to be in a defense context for laser communication systems, and these were made possible thanks to the work of Hardy, Fried and Tyler (Hardy 1978; Fried et al. 1981). The first AO system is attributed to Hardy who was working at a key contractor for the US military at the time. After the Cold War, FSOC research and funding slowed down, and relevant AO systems were mostly developed in the scope of astronomy. Hardy pioneered developments on both DM and WFS, work which would later become a foundation on modern astronomical observations (Hardy 1998). The first astronomical AO to become operational was the prototype for COME-ON on the Observatoire de Haute

Provence in 1989 (Kern et al. 1989). This setup would then be moved to ESO's La Silla (European Southern Observatory in Chile). Several other observatories followed such as the Canada-France-Hawaii in Mauna Kea and the William-Herschel Telescope in the Canary Islands. The 90s brought about the introduction of laser guide stars (LGS) for observations where natural light was insufficient, which further revolutionised the field. The Keck Observatory in Hawaii was one of the first to implement an LGS AO system (Figure 1.3).

Figure 1.3: Keck Observatory's LGS AO system creating an artificial star to measure for atmospheric distortions. (Credit: Billy Doaner, via Keck Observatory)

AO has become a staple component for ground astronomical seeing, having evolved to the point of enabling images to be taken from Earth that are on par with space telescopes. Of much worthy mention is also the work carried out in the context of so called extreme-AO (xAO) systems such as the Gemini Planet Imager (GPI) (Poyneer et al. 2005, 2007) and SPHERE (Spectro-Polarimetric High-contrast Exoplanet REsearch instrument) (Petit et al. 2008b). These systems are designed for imaging of exoplanets. These systems focus on real-time correction of atmospheric influence for high-contrast imaging. xAO systems are typically operating at higher frequencies than traditional AO (from 100 Hz to the 10 KHz range). Different wavefront sensing techniques and improvements in the scope of xAO have been tested, namely the performance of pyramid WFS, and the implementation of faster SH-WFS (Shack-Hartmann WFS) (Gerard et al. 2024). Understanding DM dynamics and their implications has also been an important topic of interest, particularly with regards to the new Extremely Large Telescope (ELT) (Correia et al. 2010).

When it comes to AO in the scope of FSOC, as noted in section 1.1, research has seen a resurgence in the last decades. In 2016, the Institute for Communication and Navigation of the German Aerospace Centre (DLR-KN) achieved a record-breaking 1.72 Tbit/s throughput, later updated to 13.16 Tbit/s in another experiment in 2017 (Poliak et al. 2018). Later in 2019, a study on the results was published, showing significant improvements on fade statistics when using AO versus only tip tilt correction (Calvo et al. 2019). Whilst these results focused on testing AO on a horizontal testbed, bidirectional satellite links with the Technology Demonstrator Payload-1 (TDP-1) on board the GEO communications satellite AlphaSat (Figure 1.4) using pre-distortion on the uplink have since been successfully carried out (Hristovski et al. 2024a; Prell et al. 2023). The French Aerospace Lab (ONERA) has also been contributing to the field initially with FEEDELIO (Bonnefois et al. 2019) experiment and presently with the optical ground station FEELINGS (Bonnefois et al. 2023). NASA's Jet Propulsion Lab (JPL) has carried out important research on the applications of space-based FSOC starting from deployment of daytime AO (Roberts et al. 2019) and working towards deep-space communications, having recently achieved a control bandwidth of 20 kHz with a DSP board solution for the real-time control (Roberts et al. 2023).

The temporal delay in AO systems generally contributes to a significant portion of the portion of the total error, typically broken down into an "error budget". This temporal loop delay refers to the waiting time between sensing the wavefront and correcting it. Predicting the wavefront has the potential to compensate for this waiting time. In recent years, optimal predictive control techniques have been at the forefront of AO control in astronomy, with reported exciting results. These aim to minimise the temporal error by using

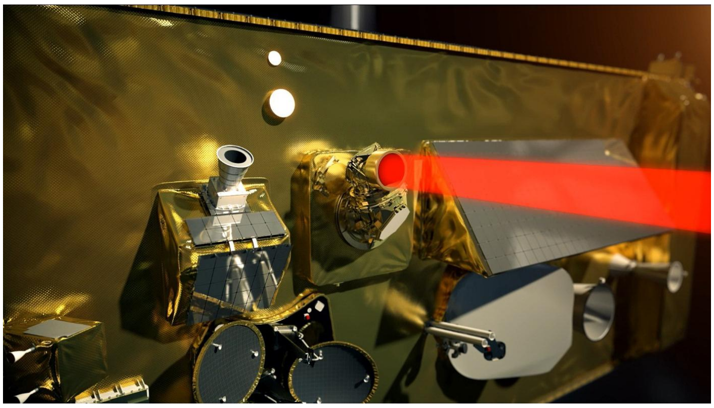

Figure 1.4: The laser communication terminal (LCT) is one of four ESA technology demonstration payloads on Alphasat. It was developed by Tesat-Spacecom GmbH with funding from DLR. (Credit: DLR/ESA.)

prediction methods. Some of the first mentions of optimal correction in the scope of AO reflect on the use of only spatial statistics to compute an optimal solution based on phase estimation (Wallner 1983; Ellerbroek 2002). Early works in optimal control, with use of temporal statistics, make use of a Linear Quadratic Gaussian (LQG) regulator but do not properly account for the way the system should be discretized (Paschall et al. 1993) or rely on a fully decoupled system (Looze et al. 2003). In 2004, an optimal LQG control law for AO and MCAO was proposed, in which a discrete-time approach with both spatial and temporal statistics was used (Roux et al. 2004). A more accurate representation of the sensing in the AO loop and the consequent delays was then proposed in (Kulcsár et al. 2006). This LQG approach led to the first laboratory validation of optimal control (Petit et al. 2008a), as well as the first on-sky testing of an LQG regulator for full AO system in astronomy (Sivo et al. 2014). In present day, significant research efforts have been going onto developing new turbulence models and associated identification strategies (Sinquin et al. 2020; Prengère et al. 2020; Marquis 2023), with the successful first full LQG on sky with a 10m class telescope taking place in April 2024 at GTC (Marquis et al. 2024).

The successful implementations of LQG AO control in the scope of astronomy poses a very important question: could we take inspiration in these findings and adapt them to the conditions experienced in FSOC to overcome turbulence influence and ultimately improve fibre coupling?

1.1.3 Optimal predictive AO control in the context of FSOC

Whilst AO has been shown to enhance FSOC performance by compensating phase distortions, it can also become highly unstable in strong turbulence conditions, and particularly when faced with strong scintillation. It has been found that the increase of scintillation severely degrades AO performance in FSOC, especially when branch points are present in the phase (Fried et al. 1992; Primmerman et al. 1995). This was further supported by Barchers et al, in a study comparing the performance of different wavefront sensors under scintillation (Barchers et al. 2003). These effects have not been studied in the context of predictive AO control, which in the scope of optical communication has the potential to minimise the impact of the temporal loop delay. Such an outcome could significantly improve link budgets, and thus is presently a very active and prolific topic of research. In 2020, a first approach to LQG for satellite tracking was proposed and simulated (Prengère et al. 2020). These results based on a zonal state-space model were very promising achieving 50% Strehl ratio, but the chosen conditions do not account for more damaging consequences of propagation effects such as scintillation on the WFS under the varying link conditions. In 2022, a Zernike basis model was built in a similar way to derive the LQG regulator and tested under similar conditions (Robles et al. 2022).

On-sky experimental data taken under strong turbulence conditions and subsequent studies support that propagation effects can be detrimental to FSOC, especially at low elevations, and the need to account for these effects in simulation was shown to be crucial (Torres et al. 2022). In 2022, Kelemu *et al* reported a simulation study of predictive control under challenging conditions and proposed a priors model that used on-sky wavefront slopes measurements to estimate covariance matrices. The resulting LQG controller was thus synthesized in measurement space and simulated for a horizontal FSOC link with boiling turbulence, achieving a modest 0.96dB improvement with regards to a tuned integrator for frozen-flow dominant turbulence (Kelemu et al. 2022). In 2024, work on a reinforcement learning algorithm was carried out with promising results but ultimately compared to an LQG model that is considered less efficient than reported state-of-the-art alternatives; this work also does not account for scintillation or WFS noise (Dray et al. 2024).

In summary, whilst current state-of-the-art LQG regulators for FSOC-AO control report promising results, these simulations most often dismiss critical propagation effects on wavefront sensing and their consequences. In the case where these effects were considered (Kelemu et al. 2022), their impact was not assessed, and the LQG regulator was designed in the WFS space using noisy measurements, which induces noise propagation. Zonal-based LQG regulators have so far yielded the best results in simulation, likely due to the preservation of spatio-temporal statistics. This is especially true for dominant frozen-flow conditions, such as the ones expected in LEO links, since a zonal representation naturally encodes frozen-flow.

Therefore, in this dissertation it is proposed to build on the work presented in (Prengère et al. 2020) in order to find the answer to the question posed at the end of section 1.1.2: "could we take inspiration in these findings and adapt them to the conditions experienced in FSOC to overcome turbulence influence and ultimately improve fibre coupling?" This is achieved by including propagation effects in simulation and understanding their impact in the unique context of LEO links under strong turbulence conditions. The feasibility of a zonal-based LQG specifically for a LEO link under strong turbulence is then assessed. Improvements to LQG model synthesis are proposed and iterated upon to better adapt the models to their use case. The different configurations are simulated and compared, and emphasis is given to performance under low elevation, strong scintillation conditions.

1.2 Synopsis

The work herein presented focuses on zonal LQG control for FSOC-AO particularly focusing on LEO satellite downlinks under low elevation and strong scintillation conditions.

In chapter 2, the relevant literature is reviewed and the fundamental theoretical principles that support the work of this thesis are summarised. This is achieved by starting with the basics of atmospheric turbulence (section 2.1), and then considering the optical propagation through turbulent air (section 2.2) as well as the degradation of the resulting optical links (section 2.3). These topics come together in the simulation of light propagation through atmospheric turbulence (section 2.4) leading to the wavefront correction with AO (section 2.5). Lastly, the considered performance parameters are summarised (section 2.6).

In chapter 3, the work towards development and integration of predictive control within the existing simulation tool is detailed. A step-by-step approach to the LQG implementation is taken (section 3.1) showing the necessary validations. This development culminated in a modular Python package for the simulation (section 3.2), and some initial simulation results over a horizontal link are presented (section 3.3).

In chapter 4, the basis presented in chapter 2 come together with the tools developed in chapter 3 in order to simulate the zonal LQG control for LEO downlinks. The simulated atmospheric conditions are presented (section 4.1) along with the AO system parameters corresponding the OGS from DLR-KN (section 4.2). The simulated LQG controllers are detailed (section 4.3) and finally the end-to-end simulation conditions and results are consolidated (section 4.4). An initial estimation of the potential improvements that LQG control enables on the communication channel is shown (section 4.5).

In chapter 5, the impact of the inclusion of physical propagation is assessed (section 5.1), complemented with a statistical analysis of simulated LEO downlink data (section 5.2). A strategy to address degraded measurements by replacing them with the prediction is presented (section 5.2.3).

Chapter 6 concludes by summarising all the findings, presenting perspectives and proposing future research directions.

Chapter 2

Adaptive Optics for Free Space Optical Communication

In this chapter, an overview of essential theory and assumptions underlying the work presented herein is provided. Section 2.1 summarises the mechanisms behind turbulence and the statistical tools to characterise it; section 2.2 takes the physical principles from section 2.1 and expands on the effects on light propagating through such turbulence, justifying the importance of the inclusion of diffraction effects in near-field propagation and summarising how to model the distorted phase; section 2.3 aims to present the consequences of the mechanisms exposed in the previous sections in the context of optical links, highlighting scintillation and wavefront error as main adverse effects in FSOC, and summarising conditions expected in different links scenarios; the sections mentioned so far contain information which is essential to understand section 2.4, which provides an overview of the chosen simulation methods including diffraction effects via angular spectrum method; section 2.5 focuses on adaptive optics for wavefront distortion compensation in the context of optical links, highlighting shortcomings of classical AO control and how modern predictive control techniques can mitigate the consequences of the loop delay; and lastly section 2.6 describes parameters that will be used to compare the performance of the different controllers.

2.1 Atmospheric Turbulence

Earth's atmosphere regulates the temperature at its surface by absorbing radiation from the sun. Sunlight propagates through the different atmospheric layers affecting different patches of air unevenly and leading to a stochastic distribution of energy levels. With natural convection promoting the rise of the heated air, eddies form as patches of air move, leading to atmospheric turbulence. The Reynolds number, Re, is a dimensionless quantity from fluid dynamics that aids in characterising whether a flow is laminar or turbulent (White 2003). It was first introduced as a dimensionless analysis method by Reynolds (Reynolds 1883) and later named in honor of his contributions to incompressible flow in fluid dynamics (Reynolds 1895). It is defined as follows:

$$\text{Re} = \frac{V\,L}{\nu} = \frac{\text{Inertial forces}}{\text{Viscous forces}} \tag{2.1}$$

where V is the velocity of the fluid [m/s], L is the characteristic length of the flow [m], and ν is the kinematic viscosity of the considered fluid [m^2/s]. In his experimental observations, Reynolds noted that for Re > 2300 the flow transitioned from laminar to turbulent (Reynolds 1883). The turbulent flow is dominated by inertial forces, exhibiting vortices, eddies and other chaotic flow behaviours. The following table (Table 2.1) was obtained by assuming a patch of turbulent air to be $L = 10$ m and assuming a nominal air kinematic viscosity of $\nu = 1.5 \times 10^{-5}$ (White 2003). It shows that we can consider air as having a fully developed turbulent flow.

The following subsections highlight important theory for turbulence modeling.

Velocity (m/s)	**Reynolds Number**
1	6.67×10^5
5	3.33×10^6
10	6.67×10^6
20	1.33×10^7
50	3.33×10^7

Table 2.1: Summary of calculations of Reynolds number for air at nominal conditions and different velocities. All values calculated exceed the critical Reynolds threshold of 2300, therefore demonstrating that atmospheric air can be considered to be fully developed turbulence.

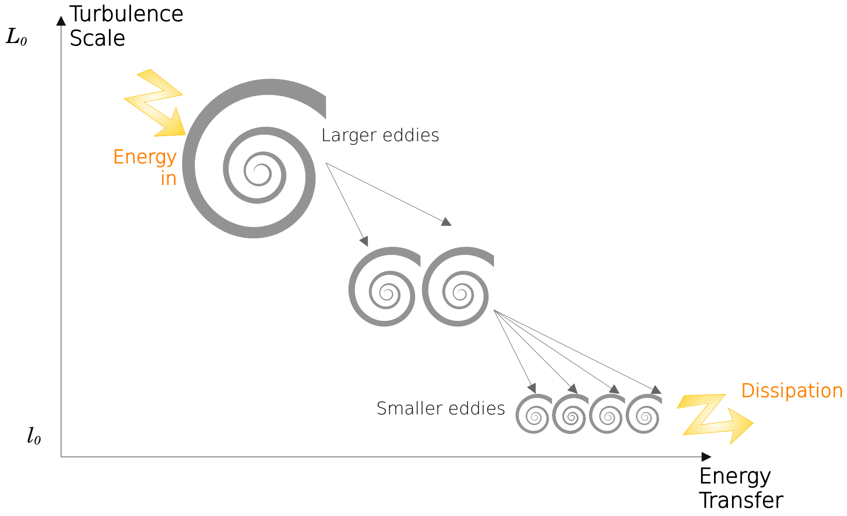

Figure 2.1: Representation of the energy cascade from larger to smaller eddies until viscous dissipation. The larger eddies, that represent the outer scale of turbulence L_0, break down into progressively smaller eddies. This process continues until the eddies are small enough for energy to dissipate as heat as a result of dominant viscous forces.

2.1.1 Kolmogorov and von Kármán theory

2.1.1.1 The concept of energy cascade

In 1922, Lewis Fry Richardson introduced the concept of an energy cascade as a weather forecasting tool (Richardson 1922), a mechanism he described as follows:

> *"Big whirls have little whirls that feed on their velocity,*
> *and little whirls have lesser whirls, and so on to viscosity."*

In 1941, Kolmogorov presented a statistical model for fully-developed turbulence (Kolmogorov 1941) formalising the concept of the energy cascade (Figure 2.1). This theory states that energy is transferred from the larger eddies (L_0, outer scale) into progressively smaller eddies without energy loss, and continues to do so until viscous dissipation occurs at very small scales (l_0, inner scale). This range where the balance between energy input and dissipation is maintained in a steady state is often denoted as the inertial subrange. In simpler terms, the inertial subrange corresponds to the turbulent structures sized between l_0 and L_0. The Kolmogorov concept of energy cascade is an abstraction, based on idealized flows falling under the assumption of infinitely homogeneous (i.e. constant properties at every point in space), isotropic (i.e. constant properties in all directions) and incompressible turbulence, with a constant rate of energy dissipation. These assumptions facilitate statistical analysis and lead to the formalisation of structure functions to describe certain properties of turbulence.

2.1.1.2 Structure function

Atmospheric turbulence is a difficult process to predict given its random nature. However, it can be statistically characterised. Structure functions help quantify statistical properties of fluctuating fields by comparing a chosen property between points in the random field. In 1941, Kolmogorov formalized a velocity structure function to quantify how much a difference between velocity of two points is a function of the distance between them (Kolmogorov 1941). This formalisation relied on three assumptions regarding the fully developed turbulent air: as the velocity of the flow is much lower than that of the speed of sound, air is incompressible; moreover, within the inertial subrange, the turbulence can be considered homogeneous and isotropic (section 2.1.1.1). Under these assumptions, it is possible to describe a structure function for velocity by the ensemble average:

$$D_v(r) = \langle [v(x+r) - v(x)]^2 \rangle \tag{2.2}$$

where r represents the separation of two points in space.

Kolmogorov theorised that the second order velocity structure function depends solely on the separation r and the dissipation rate per unit mass ε, which is the rate at which energy is transferred down along the energy cascade depicted in Figure 2.1. Through dimensional analysis it is then possible to write (Sasiela 2012):

$$\begin{gathered} D_v(r) \propto \varepsilon^a \, r^b \\ \therefore \\ [m^2/s^2] = [m^2/s^3]^a \, [m]^b \end{gathered} \tag{2.3}$$

from which proceeding with the dimensional analysis unit by unit, it is then clear that:

$$D_v(r) \propto \varepsilon^{2/3} r^{2/3} \tag{2.4}$$

the proportionality constant being the velocity structure constant, denoted by C_v^2. The dissipation rate ε is the rate at which kinetic energy converts to heat at small scales. As was mentioned in section 2.1.1.1, within the inertial subrange, the transfer rate across the cascade remains constant and thus no energy is lost to friction. Therefore, the term ε is "absorbed" by the constant and we can simply write (Sasiela 2012):

$$D_v(r) = C_v^2 r^{2/3}, \quad \forall r \in [l_0, L_0] \tag{2.5}$$

which is known as the $2/3$ Kolmogorov power law. This law applies to any passive scalar, i.e., to any quantity that is "transported" by the dynamics in the flow rather than affecting them directly. Since we can consider the refractive index to be a passive scalar, then the same proportionality law can be written (Tatarskij 1961):

$$D_n(r) = C_n^2 r^{2/3}, \quad \forall r \in [l_0, L_0] \tag{2.6}$$

where the constant is instead called refractive index structure constant and is denoted by C_n^2. This parameter is often used in atmospheric profiling, as it depicts a relative strength of the atmosphere as a consequence of refractive index fluctuations. Through dimension analysis it was also demonstrated that refractive index fluctuations happen solely due to temperature changes. These fluctuations in refractive index cause the disturbance in optical propagation. These effects and their consequences on the light that propagates through the atmosphere are explored more in depth in section 2.2.

2.1.1.3 Spatial power spectra

Section 2.1.1.2 introduced the concept of structure functions for statistical analysis for fluctuating fields by quantifying variations in passive scalars. To further understanding on this matter and view how energy is distributed across different spatial frequencies in the flow, it is interesting to look at the power spectra. The spatial power spectrum describes how the intensity or pattern of the turbulent flow is distributed across different wavenumbers. The wavenumber k can be defined as the spatial frequency of a disturbance, as it represents the number of cycles per unit distance. It is mathematically defined by:

$$k = \frac{2\pi}{l} \tag{2.7}$$

where l represents a distance between inner and outer scale, i.e. $l_0 < l < L_0$. The lower the wavenumber, the larger the scale of features which are being considered. By opposition, the higher the wavenumber the finer the features. Following a similar analysis as described in equation (2.3), it is possible to represent the energy of the fluctuating refractive index as a function of k:

$$E(k) \propto \varepsilon^{2/3} k^{-5/3} \tag{2.8}$$

where $E(k)$ represents the energy contained in each spatial frequency. This decaying $5/3$ power law indicates that within the inertial subrange, energy decreases with increasing wavenumber, and by contrast smaller scales contain less energy. In section 2.1.1.1, it was stated that energy moves from larger to smaller scales. The decaying Kolmogorov $5/3$ power law quantifies this same energy cascade in the spatial frequency domain. Similarly to what was described in section 2.1.1.2, equation (2.6) it is also possible to represent fluctuations of refractive index as a function of spatial frequencies (Tatarskij 1961). This is commonly referred to as Kolmogorov power spectra and described by:

$$\Phi^{\mathsf{K}}(k) = 0.033 C_n^2 k^{-11/3}. \tag{2.9}$$

Whilst widely used, it is important to stress that this description of the power spectra has the caveat of not accounting for the correlation limitations that happens when increasing the separation. In short, it does not account for the decay in the power law at both high and low spatial frequencies, as the turbulent structures have a finite size. The von Kármán model introduced the concept of outer scale L_0, thus addressing lower spatial frequencies. The von Kármán spectra can be represented by:

$$\Phi^{\mathsf{vK}}(k) = 0.033 C_n^2 \left(k^2 + k_0^2\right)^{-11/6} \tag{2.10}$$

where $k_0 = 2\pi/L_0$, thus accounting for the decay at lower spatial frequencies. A similar decay of the power law is also observed at high spatial frequencies, since after reaching the smallest scales the energy is dissipated as friction. Modified von Kármán spectra follows a similar logic to introduce constraints on the inner scale l_0:

$$\Phi^{\mathsf{mvK}}(k) = 0.033 C_n^2 \frac{\exp\left(-k^2/k_m^2\right)}{\left(k^2 + k_0^2\right)^{11/6}} \tag{2.11}$$

where $k_m = 5.92/l_0$, thus accounting for the influence of the inner scale. The introduction of these constraints helps more accurately characterizing problems that happen within a tighter range of scales. The wider the range between l_0 and L_0, the closer the modified von Kármán and von Kármán theory resemble Kolmogorov decay line. In Figure 2.2, we observe the different scaling behaviors of the Kolmogorov spectrum, the von Kármán spectrum, and the Modified von Kármán spectrum.

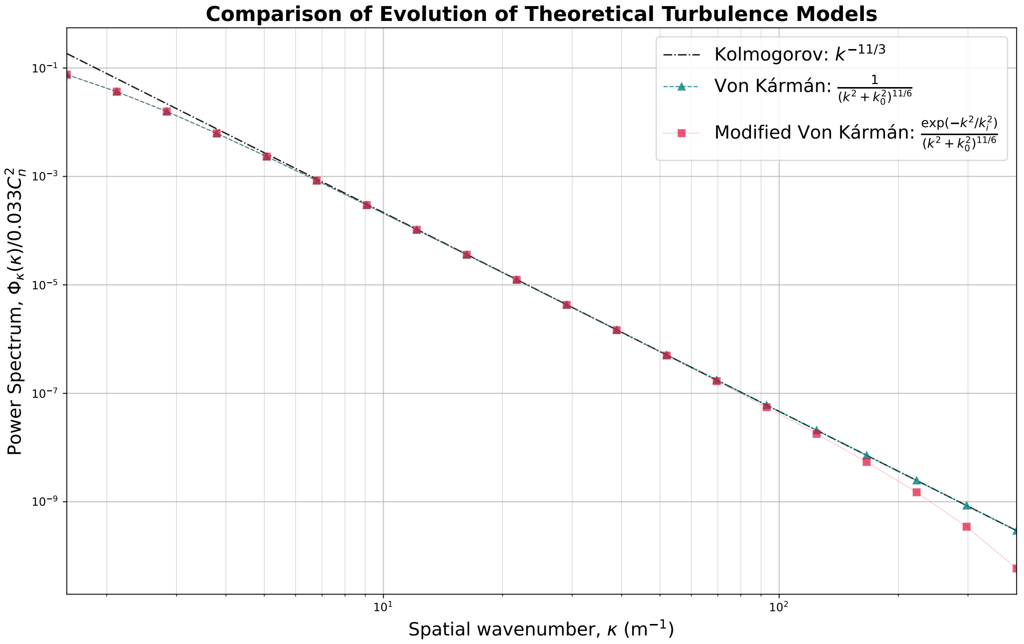

Figure 2.2: Summary comparison of the different aforementioned models for turbulence power spectra. The Kolmogorov spectrum follows a $k^{-11/3}$ law, while the Von Kármán accounts for the outer scale. It also shows the modified von Kármán, which came about from adding inner scale breakdown into von Kármán Theory (Tatarskii 1971). It is of note that for the limit case of $l_0 = 0$ and $L_0 = \infty$, von Kármán and modified Von Kármán converge to the Kolmogorov theory.

2.1.2 Turbulence profiling

The atmosphere can be modeled as a set of discrete layers moving independently (as detailed in section 2.1.3). This is illustrated in Figure 2.3.

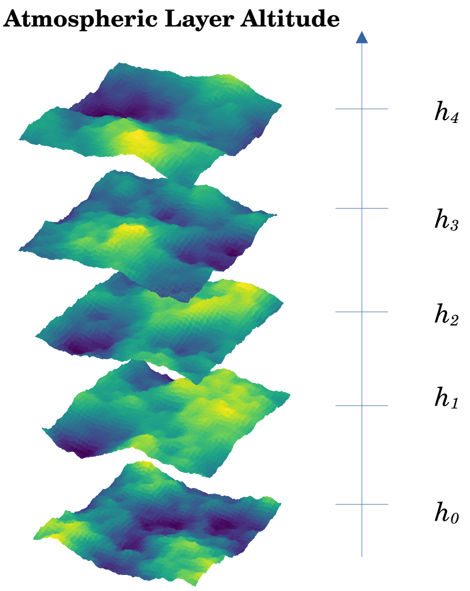

Figure 2.3: Depiction of the atmosphere model as a set of discrete layers that are independently modeled at chosen heights.

Fluctuations in the refractive index have been identified as the mechanism behind atmospheric or optical turbulence. In section 2.1.1.2, the refractive index structure constant C_n^2 was introduced. The C_n^2 constant provides information on the strength of atmospheric turbulence. It is of note that this index is not constant in either time or space throughout the atmosphere. In fact, several models have been established to describe the variations of C_n^2 with altitude. In this work, the considered reference is the Hufnagel-Valley (HV) profile, given the flexibility to calculate for different conditions. The HV profile was created based on experimental data and can be obtained as:

$$C_n^2(h) = 0.00594 \left(\frac{w}{27}\right)^2 (10^{-5}h)^{10} e^{-h/1000} + 2.7 \times 10^{-16} e^{-h/1500} + T\, e^{-h/100}, \tag{2.12}$$

where h [m] is the altitude , w [m/s] represents the high-altitude rms windspeed, and $T = C_n(h_0)^2$ [m] is the turbulence strength at ground level. Turbulence profiling is useful in simulation and further detailed in section 2.4. The rms windspeed w is defined with regards to a wind velocity profile with:

$$w = \left[\frac{1}{15 \times 10^3} \int_{5\times10^3}^{20\times10^3} V^2(h)\, dh\right]^{1/2} \tag{2.13}$$

where $V(h)$ represents the wind velocity profile. This can be calculated with the model often attributed to Bufton which was defined by Greenwood (Greenwood 1977)

$$V(h) = w_s \cdot h + V_g + V_T \exp\left[-\left(\frac{h\cos(\zeta) - H_T}{L_T}\right)^2\right] \times \left[\sin^2\varphi + \cos^2\varphi\cos^2\zeta\right]^{1/2} \quad , \tag{2.14}$$

where w_s is the slew rate of the satellite, V_g and V_T are respectively the ground and tropopause wind speeds; V_g is the ground wind speed; ζ is the zenith angle; H_T and L_T are height and thickness of the tropopause layer, and φ is the wind direction relative to the telescope azimuth. The slew rate w_s term incorporates the apparent wind resulting from tracking the target into an otherwise natural wind profile. The apparent wind effect is further explain in section 2.3.

2.1.3 Taylor's frozen flow hypothesis

The previous sections focused on spatial statistics solely. When it comes to temporal effects, some assumptions are needed in order to derive temporal statistics. In 1938, G. I. Taylor proposed the frozen flow hypothesis otherwise known as the Taylor Hypothesis (Taylor 1938). This theory states that although the turbulence is characterized by the presence of chaotic structures like vortexes and eddies, these can be seen as moving with the mean of the flow. In simpler terms, when considering a turbulent flow with high mean velocity, the turbulent structures move past a fixed observer without significant shape or structural changes. This assumption allows the flow to be considered as drifting through in a frozen state, as is depicted in Figure 2.4.

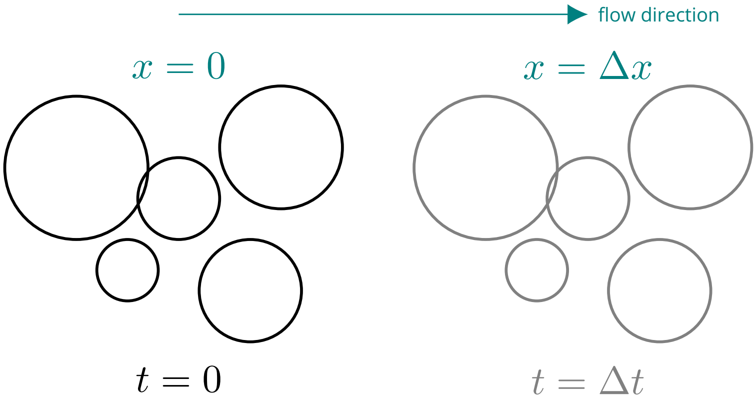

Figure 2.4: Visual representation of the frozen flow hypothesis. Turbulence eddies (represented by circles) move with the mean of the flow in a frozen manner, thus maintaining spatial distribution as they travel with the flow from x to Δx.

The frozen-flow assumption implies that what is measured at a point in time can give spatial information. It is therefore possible to relate temporal and spatial spectra with:

$$f = kU \tag{2.15}$$

meaning that frequency f of a turbulent structure passing through a fixed point is related to its wavenumber through the flow mean velocity U. As this assumption allows temporal variations to be interpreted as spatial structures, turbulence can also be described using spatial basis functions such as the Zernike polynomials. Zernike modes are an orthogonal basis for representing spatial variations, particularly useful in circular apertures. The power spectrum of the turbulence field can thus be expanded in terms series of Zernike modes.

2.1.4 Optical turbulence parameters

Along with the turbulence profile (section 2.1.2), different turbulence parameters provide information about atmospheric turbulence at a specific cite, and its consequences on the wavefront distortions. The following sections detail the turbulence parameters that were essential in the context of this thesis manuscript.

2.1.4.1 Fried parameter

The Fried parameter r_0 describes the spatial coherence length of a wavefront passing through optical turbulence. It is defined as the distance over which the root-mean-square (RMS) phase distortion caused by turbulence is approximately 1 radian. It is described by:

$$r_0 = \left[0.423\, k^2 \sec(\zeta) \int_0^\infty C_n^2(h)\, dh \right]^{-3/5} \tag{2.16}$$

where k is the wavenumber, ζ is the zenith angle, and $C_n^2(h)$ represents the turbulence strength integrated by altitude range. Physically, it represents the largest aperture which can support diffraction limited optical performance without wavefront correction. The stronger the turbulence, the lower the r_0 value.

2.1.4.2 Coherence time

The coherence time τ_0 quantifies the temporal evolution of an optical wavefront as it travels through turbulent media. It is therefore measured in units of time and represents a characteristic time interval over which the phase distortions induced by the turbulence in the atmosphere are still correlated. It is defined by the time during which the mean square error of the phase changes by 1 radian. It can be written in proportion to C_n^2 or r_0 by

$$\tau_0 = 0.057\,\lambda^{6/5}\left[\int_0^\infty C_n^2(h)\,V^{5/3}(h)\,\mathrm{d}h\right]^{-3/5} = 0.314\,\frac{r_0}{V_{\text{eff}}} \tag{2.17}$$

where r_0 is the coherence length or Fried parameter (section 2.1.4.1), λ is the seeing wavelength, C_n^2 is the refractive index structure constant from which the turbulence profile can be obtained (section 2.1.2), $V(h)$ is the wind speed as a function of altitude h, and finally the V_{eff} is the effective wind speed which is given by

$$V_{\text{eff}} = \left[\frac{\displaystyle\int_0^\infty C_n^2(h)\,V^{5/3}(h)\,\mathrm{d}h}{\displaystyle\int_0^\infty C_n^2(h)\,\mathrm{d}h}\right]^{3/5}. \tag{2.18}$$

2.1.4.3 Rytov variance

The Rytov Variance σ_R^2 quantifies the strength of optical wave intensity fluctuations caused by atmospheric turbulence. It is closely related to scintillation, and can be described by:

$$\sigma_R^2 = 2.25k^{7/6}\sec^{11/6}(\zeta)\int_{h_0}^{H} C_n^2(h)(h-h_0)^{5/6}dh \tag{2.19}$$

where L is the length of the propagation path. The Rytov variance provides a classification between weak ($\sigma_R^2 < 1$) and strong ($\sigma_R^2 > 1$) turbulence regimes. It provides a way to quantify intensity fluctuations as light propagates through a turbulent medium. The higher the Rytov variance, the stronger the scintillation. Whilst it is related with r_0 it is distinct from it. Two distinct turbulence conditions can have the same r_0 and very different σ_R^2 due to the position of the turbulence with respect to a receiver.

2.2 Optical propagation through turbulent air

The previous sections (2.1) highlighted important spatial and temporal statistical models for the atmosphere. Concepts such as spatial power spectra (section 2.1.1.3) and structure functions (section 2.1.1.2) were introduced. In this section, these topics are expanded upon within the particular context of light propagation through turbulent air, and the consequences for an FSOC link. The refractive index fluctuations are highlighted as the main mechanism of optical turbulence, and the consequences and resulting beam degradation are explored.

2.2.1 Light propagation

There are two approaches to a scientific description of light. Classical electrodynamics is used to describe light as an interaction between electromagnetic fields continuous in both space and time. It is generally useful when dealing with macroscopic properties. Quantum electrodynamics deals with light particles or photons, which are devoid of mass and charge, and is used mostly for submicroscopic properties. Both are fundamental theories to the scientific understanding of light, with supporting experimental evidence, leading to what is often referred to as wave particle duality. In the scope of this manuscript, macroscopic properties are in focus and thus the suitable description is classical electrodynamics. In 1865, James Clerk Maxwell successfully demonstrated that electromagnetic fields travel as waves at the speed of light. The Maxwell equations are a set of equations based on experimental laws of electricity and magnetism that were unified into a single theoretical framework for electric and magnetic fields (Maxwell 1865). These have come to be the mathematical basis in wave propagation theory, and the subsequent sections can all be demonstrated to be derived from or related to the Maxwell equations (Born et al. 2019; Hecht 2017). For the scope of this work, an electromagnetic field $E(\mathbf{r})$ can be simply described by the equation:

$$E(\mathbf{r}) = A(\mathbf{r})e^{i\Phi(\mathbf{r})} \tag{2.20}$$

with $\mathbf{r}$ representing a position in space, $A(\mathbf{r})$ the amplitude of the field and $\Phi(\mathbf{r})$ its phase. The exponential term $e^{i\Phi(\mathbf{r})}$ encodes the phase variation of the field as a function of position.

Paraxial approximation

The description of propagation of monochromatic electromagnetic waves in a medium is given by the Helmholtz equation, which is in turn derived from the Maxwell equations (Hecht 2017). However, solutions to this are complex to obtain due to the spatial variation in both amplitude and phase of the electromagnetic field. Different assumptions can be made in order so simplify the modeling of specific cases. In the realm of optics, the region of interest is most often the space very close to the optical axis and therefore the paraxial approximation adequately describes the conditions. This approximation is valid when considering small angles from the optical axis (Schmidt 2010). It can be obtained by assuming that wave propagation happens along the optical axis and that transverse variations in amplitude are significantly weaker when compared to variations along the propagation direction. This regime is often denoted as Gaussian optics. With the resulting simplifications, it is possible to rewrite the electric field in equation (2.20) as (Saleh et al. 2019):

$$E(\mathbf{r}) = A(\mathbf{r})e^{ikz} \tag{2.21}$$

where $k = \frac{2\pi}{\lambda}$ is the wavenumber and e^{ikz} represents the fast oscillations along the z-axis. This can also be referred to as a paraxial wave traveling along the z direction and modulated by the complex amplitude A.

2.2.2 Diffraction

Diffraction is an optical phenomena that results in spreading of light when its wavefront is disturbed by an obstacle, aperture, or in-homogeneous medium. As the wavefront travels through apertures, the light is constrained. This causes the light to bend and/or spread, leading to beam divergence. These effects compound with propagation distance, as the shape of the wavefront and energy distribution evolve. Diffraction is therefore modeled differently according to propagation distance. Far-field propagation assumes a long enough propagation distance that the divergence of the wave is the dominant effect and the wavefront expands far enough that its curvature can be assumed to be infinite and therefore a plane wavefront is assumed. Modeling light propagation in the far-field is mathematically represented by a simple Fourier Transform (FT) of the aperture function. This is known as the Fraunhofer diffraction model, and is detailed in Fourier Optics books (Goodman 2005). Because the propagation distance far exceeds the aperture size, the transmitted field can be treated as a plane wave arriving at the top of the atmosphere. Therefore in this work, a plane wave scenario is considered.

Fresnel approximation for scintillation

The use of the Fresnel approximation is necessary to characterize intensity fluctuations (scintillation) caused by atmospheric turbulence. Scintillation is a result of local interference between wavelets scattered by atmospheric eddies. According to the Hyugens-Fresnel principle, it is assumed that each single point in a wavefront is itself propagated as a spherical wavelet. These waves interfere constructive and destructively to produce the resulting diffraction pattern in the observation plane. In the near-field, it is therefore relevant to consider interference and its cumulative effects in the electric field pattern.

The scalar Fresnel diffraction integral defines the electric field E at a given point in space $P = (x, y)$ as:

$$E(P) = \frac{e^{ikr}}{i\lambda r} \int_{-\infty}^{\infty} \int_{-\infty}^{\infty} E(x', y') e^{i\frac{k}{2r}\left[(x-x')^2+(y-y')^2\right]} dx'dy' \tag{2.22}$$

where r represents the distance between the observation P and the source with coordinates (x', y') and $E(x', y')$ represents the e-field at the source. The scaling factor $\frac{e^{ikr}}{i\lambda r}$ accounts for phase shifts along a propagation distance r (see section 2.2.1, equation (2.21)), while the quadratic integrated exponential $e^{i\frac{k}{2r}\left[(x-x')^2+(y-y')^2\right]}$ accounts for phase variation across each observation plane by considering the curvature of spherical wavefronts and therefore including diffraction effects. Numerical evaluations for the Fresnel diffraction integral can be obtained by either expanding the exponentials terms and considering a single FT to represent a translation between two spherical waves, or by rewriting the double integral as a convolution and therefore computing it as two FTs (Schmidt 2010). In the scope of this thesis, the convolution form is used in a method designated as angular spectrum propagation; this is shown in section 2.4.

2.2.3 Wavefront and phase

As a light propagates through vacuum, photons travel at the same speed. Thus, all photons composing an incoming wavefront entering the atmosphere will be at the same phase of the wave cycle. However, when a beam propagates through turbulent air, the speed of each photon is affected by the local refractive index, and is subject to fast variations. The varying speeds at which photons travel will distort the incoming wavefront, as these particles will now be in a different phases of their wave cycle. Whilst the turbulence causing this behaviour is a stochastic process, structure functions can be used to describe property variations across two points in space, as was introduced in section 2.1.1.2.

2.2.3.1 Phase structure function and variance

A phase structure function characterizes the spatial correlation of turbulence induced phase distortions. Following a similar logic as the structure functions mentioned in section 2.1.1.2, the mean phase difference can be defined by:

$$D_\phi(\rho) = \langle [\phi(\mathbf{r} + \rho) - \phi(\mathbf{r})]^2 \rangle \tag{2.23}$$

where $\phi(\rho)$ represents the phase at position $\mathbf{r}$; ρ is the separation between two points; and $\langle . \rangle$ represents the ensemble average over turbulence realizations. If the turbulence is assumed to follow Kolmogorov spectrum (section 2.1.1), the phase structure function can be simplified to (Tatarskij 1961):

$$D_\phi(\rho) = 6.88 \left(\frac{\rho}{r_0} \right)^{5/3} \tag{2.24}$$

where r_0 is the Fried parameter defined in section 2.1.4.1. The phase variance accumulated over a given propagation path L in a homogeneous medium is given by:

$$\sigma_\phi^2 = k^2 \, L \int_0^\infty \Phi_n(\kappa) \, 2\pi\kappa \, d\kappa \tag{2.25}$$

where $k = 2\pi/\lambda$ is the optical wavenumber, and $\Phi_n(\kappa)$ is the von Kármán spectrum (equation (2.10)). The phase variance σ_ϕ^2 can be related back to the structure function through the Fourier transform; by doing so and including equation (2.10) for the von Kármán spectrum, it is possible to obtain the von Kármán phase structure function:

$$C_\phi(\rho) = \left(\frac{L_0}{r_0} \right)^{5/3} \left[\left(\frac{24}{5} \right) \Gamma(6/5) \right]^{5/6} \frac{\Gamma(11/6)}{2^{5/6}\pi^{8/3}} \left(\frac{2\pi\rho}{L_0} \right)^{5/6} K_{5/6} \left(\frac{2\pi\rho}{L_0} \right) \tag{2.26}$$

where L_0 is the outer scale, r_0 is the Fried parameter, Γ is Euler's Gamma function, and $K_{5/6}$ is a modified Bessel function of the second kind with order $5/6$. Equation (2.26) is a key building block when it comes to stochastic turbulence models for AO predictive control. This exact formulation was derived by (Assémat et al. 2006), which references the work of Tokovinin (Tokovinin 2002) based on the works of (Consortini et al. 1972) and (Conan et al. 2000). More extensive demonstrations and studies can be found in the works of Tatarskij (Tatarskij 1961), Strohbehn (Strohbehn 2005) as well as Andrews & Phillips (Andrews et al. 2005).

2.2.3.2 Representation of the turbulent phase

Accurate representation of the turbulent phase is essential when it comes to achieving effective wavefront correction (section 2.5). Two general approaches can be taken: to represent the phase on a zonal or modal basis. Modal representations express wavefronts as a linear combination of functions described on an orthogonal basis set. Examples of popular modal basis are the Zernike modes (Noll 1976) or the Karhunen–Loève modes (Berkooz et al. 1993). While modal approaches offer a compact representation with possibly reduced computational complexity, a zonal basis allows for a representation of the phase native to the manner it is sensed and compensated (for actuators and measurements on a square grid). Furthermore, the Zernike basis is inaccurate for annular apertures, as it is no longer orthogonal over a pupil with central obscuration, resulting in aliasing between modes (Mahajan 1981). A zonal basis offers a convenient description when it comes to FSOC conditions, especially when considering dominant high apparent wind speeds present with LEO satellites (see section 2.3) and the receiving small apertures. This was evidenced in (Prengère et al. 2020). Strong winds are responsible for creating turbulent structures that are mainly shifted, hence easily represented on a zonal basis even on small spatial scales. Their prediction is therefore also easier (corresponding to a shift for most of the points, so a very localized operation at small scale). With a modal basis, this frozen flow behaviour at small scales is more complex to represent and thus less convenient (with in addition the edge effects mentioned above for the Zernike basis). As smaller apertures are more impacted by small-scale features, this requires an accurate representation of such turbulent structures. For all these reasons, this manuscript focuses on a zonal representation of the phase (see section 2.5.2).

2.3 Degradation of optical links

2.3.1 Intensity fluctuations and wavefront aberrations

Optical turbulence is a consequence of fast refractive index fluctuations, causing phase distortions in the wavefront. These wavefront distortions cause issues focusing the beam in a telescope, an effect which is worse for a larger aperture. In the far field, these wavefront distortions evolve and stabilise into amplitude variations causing intensity fluctuations which are often referred to as scintillation. Scintillation can be partly mitigated by increasing the aperture size (Figure 2.5). In the context of optical communications, telescopes diameters are are typically between 40cm-1m depending on the requirements of the link, resulting in diameters that are 8 to 50 times the r_0 scale ($8 < D/r_0 < 50$), assuming r0 is in the range of (2-5cm).

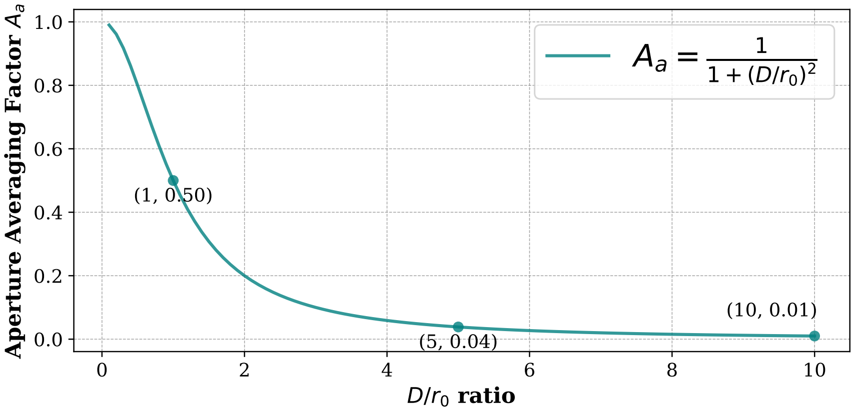

Figure 2.5: Aperture averaging factor (A_a) as a function of D/r_0. Larger apertures reduce scintillation by spatially averaging intensity fluctuations (Andrews et al. 2005).

Scintillation has been identified as a cause for loss of performance in optical links (Barchers et al. 2003). This loss of performance can be quantified as PSI or power scintillation index (see section 2.6.1). This is partly addressed with high D/r_0 ratios facilitating aperture averaging. In optical links wavefront aberrations are dominant leading to high wavefront error as the light is focused and coupled onto a single-mode fibre. Wavefront error refers to spatial phase distortions induced by the varying refraction index across the propagation path. These distortions degrade coherence, reduce the Strehl ratio and thus lower the coupling efficiency. In order to mitigate these effects and improve coupling efficiency, FSOC systems include adaptive optics system in the ground segment. However, when it comes to deploying predictive controllers, it is important to consider that different link scenarios will require different models computed from appropriate methods. The following sections highlight the different conditions experienced in FSOC satellite links.

2.3.2 Differences between up- and downlink

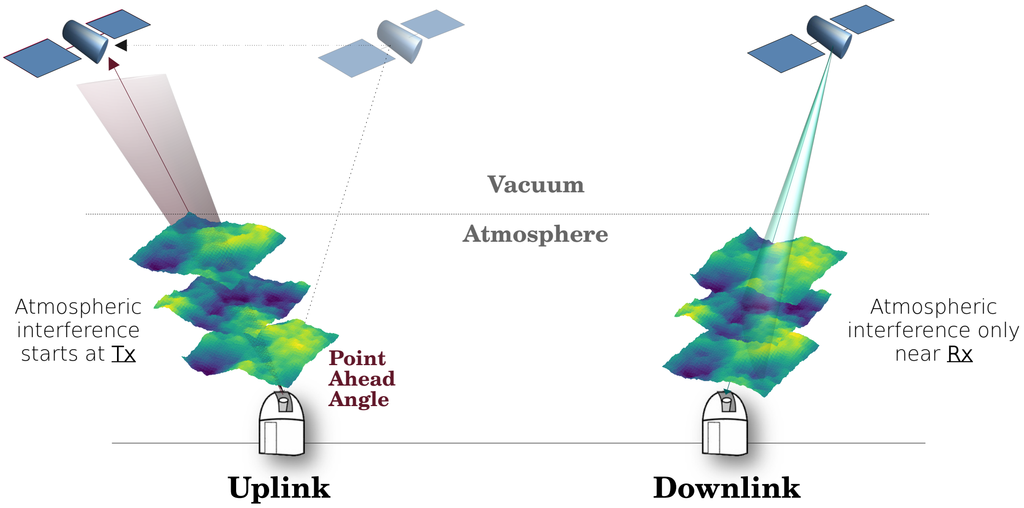

Figure 2.6: Differences between uplink and downlink. Uplink: beam is affected near transmitter (Tx), impacting displacement right at source. Angular displacement from Tx will have a massive impact on receiver (Rx), resulting in stronger beam wander, beam spread, and fast varying intensity pattern. Downlink: displacement near Rx, effects not as damaging.

As light travels through the atmosphere, it experiences turbulence (section 2.1) and diffraction (section 2.2.2). The atmospheric interference leads to several beam degradation phenomena. The impact of these effects is different in uplink and downlink as they experience turbulence at different stages of the beam propagation. This is depicted in Figure 2.6. Uplink is dominated by beam wander and beam spread due to turbulence being the strongest at Tx (transmitter), such that even a small angular displacement at the source will have a massive impact on Rx (receiver). Beam wander can be interpreted as a strong angular displacement of the wavefront in two perpendicular directions (i.e. tip/tilt displacement). Beam spread causes an increase in the overall beam diameter due to small-scale refractive index fluctuations resulting in higher beam divergence, leading to a long term increase of the footprint of the intensity distribution (Figure 2.7). On the other hand, downlink beams mostly propagate through vacuum and are affected by atmosphere near Rx. As a result the physical manifestation of turbulence differs between uplink and downlink.

2.3.3 Satellite orbit impact on optical links

Different link scenarios experience different levels of turbulence according to the respective satellite orbit. Geostationary orbits (GEO) satellites are at approximately 35 800 km and are easier to track. Turbulence is often persistent but with lower intensity at fixed elevation angles. GEO links have a considerably higher latency when compared to LEO links; they are, however, vital in maintaining efficient data networks, as they are often used as data relay. One such example is the EDRS, or European Data Relay System, which uses GEO satellites as nodes in intersatellite communications for efficiency.

Low-Earth Orbit (LEO) satellites are closer to Earth (500-2000km). This leads to fast angular motion, leading to very short passes of links with one particular OGS. The fast angular motion results in a so-called apparent wind effect (see Figure 2.10). A significant portion of a LEO optical link occurs at very low elevations, resulting in the beam traversing through strong apparent winds, resulting in strongly aberrated

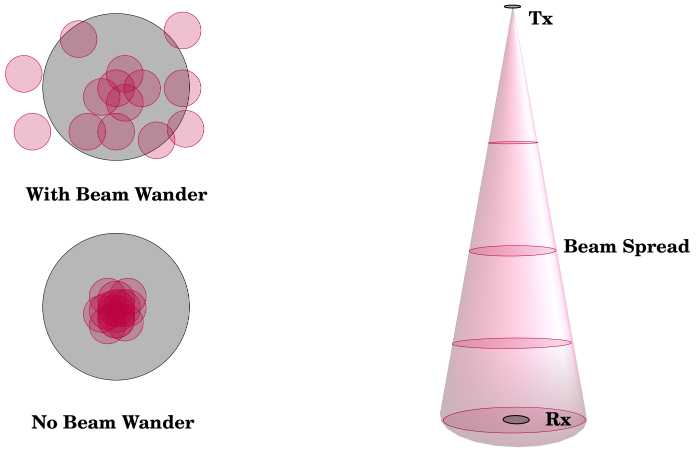

Figure 2.7: Left: Depiction of long exposure PSF at the receiver with and without beam wander; Right: Depiction of beam spread with propagation distance.

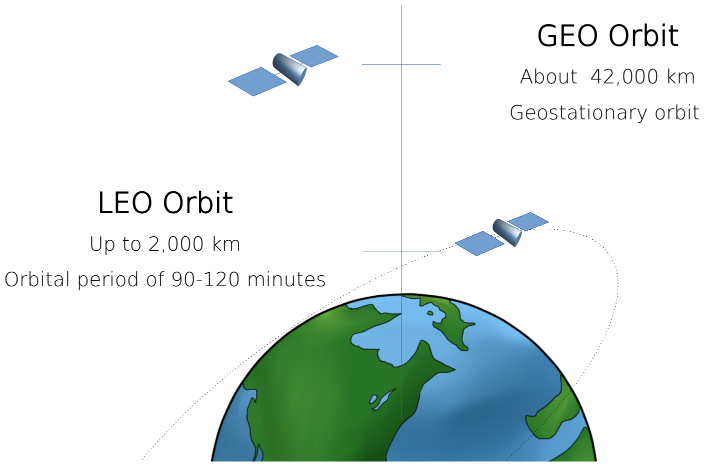

Figure 2.8: Depiction with scale of Low-Earth Orbit (LEO) satellites when compared to Geostationary orbits (GEO).

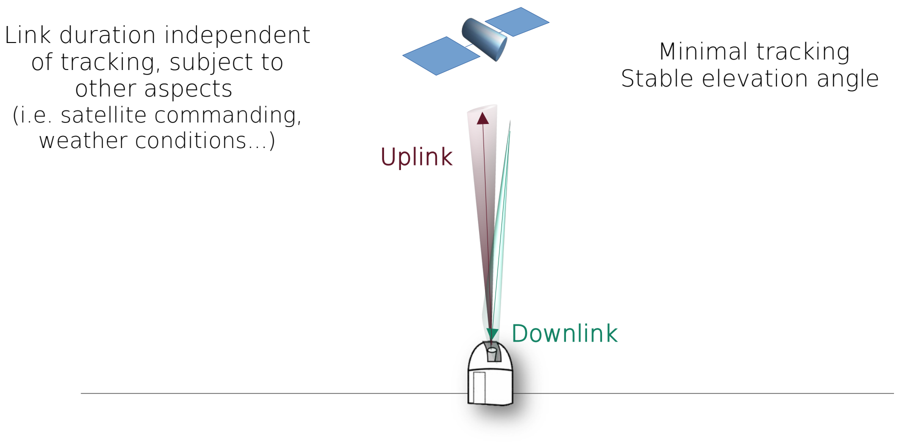

Figure 2.9: Example of GEO satellite bidirectional link with an OGS.

wavefronts of difficult correction, ultimately leading to lots of fades and scintillation. Lower elevations lead to lower $r0$ along to line-of-sight, due to the dependence on the Zenith angle ζ (see section 2.1.4.1).

In the scope of this thesis, LEO links will be in focus due to their challenging nature and relevancy for

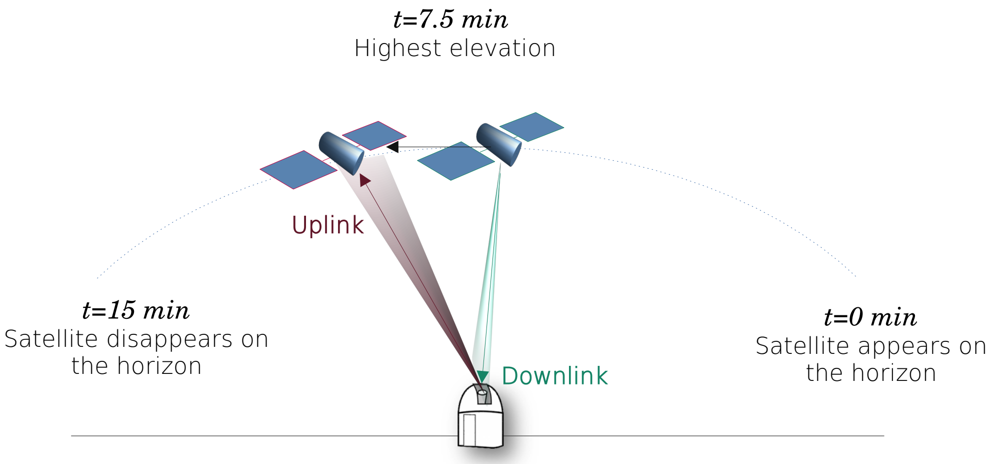

Figure 2.10: Example of LEO satellite pass over an OGS with bidirectional link. LEO passes are very short in time (approximately 10 to 20 minutes) and typically low elevation, starting as low as 15°.

global connectivity applications. In addition to the different orbits, turbulence scenarios will vary according to location and time of day, as well as local atmospheric conditions. FSOC systems are expected to operate also during daylight, under strong turbulence conditions. This is due to the need for a global connectivity network operating 24/7, as well as placing the optical ground stations closer to fibre infrastructure for ease of ground distribution, often leading to suboptimal locations in terms of turbulence.

2.4 Simulating light propagation through atmospheric turbulence

As seen previously in section 2.2, atmospheric turbulence can be represented as a series of discrete layers moving independently. Each discrete layer can be represented by a phase screen, which can be generated according to von Kármán statistics (section 2.1). Simulation tools developed for Astronomy often dismiss Fresnel propagation and assume so-called geometric propagation. Whilst appropriate within the scope of astronomy due to the favourable observation conditions, such assumption dismiss scintillation and fades, which are detrimental phenomena observed in FSOC link data as has been shown in section 2.3. The following section explains the different propagation methods considered.

2.4.1 Light propagation methods

A simplified method for simulating light propagation through atmospheric turbulence is geometric propagation (Fried 1982) where light is modeled as rays traveling along straight paths. These paths are only modified by phase distortions introduced by turbulence layers. Mathematically, this method can be summarised by simply taking the resulting turbulence to be the sum of all individually generated phase screens. This approach is computationally efficient and represents an effective method to simulate large-scale turbulence effects. However, this method dismisses propagation-driven wavefront degradation, neglecting effects such as diffraction and interference. These are critical factors to consider to accurately model beam propagation through small-scale turbulence structures (see Figure 2.11).

FSOC systems are designed to operate in daylight at strong turbulence locations, and require optimal single mode fibre coupling to stay within link budgets. Therefore, these shortcomings can lead to performance degradation due to beam distortion, scintillation, and bandwidth intensity fluctuations; conversely this can lead to optimistic fibre coupling efficiency in simulation results. In order to address these limitations and include diffraction, the angular spectrum method was included in the simulator. Angular spectrum

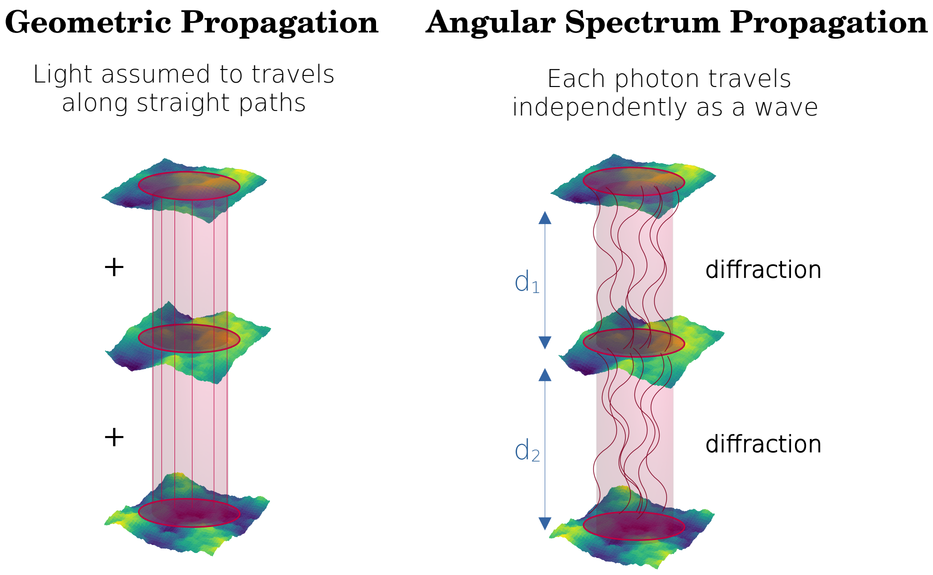

Figure 2.11: Comparison between geometric and angular spectrum light propagation methods.

propagation offers a wave-focused alternative by including the detailed evolution of both phase and amplitude while accounting for diffraction and interference effects, making it a more reliable tool for FSOC simulations and leading to more realistic, less optimistic results. The method is based on representing the optical field as a superposition of plane waves using the angular spectrum of the field. It includes diffraction, and has been shown to be an accurate representation of near-field propagation (Goodman 2005). It leverages Fourier optics to describe the evolution of spatial frequencies, whilst explicitly computing the phase shifts. In simulation, the resulting electric field can be computed with:

$$U_{\text{out}}(x_{\text{out}}, y_{\text{out}}) = Q_3 \cdot \mathcal{F}^{-1}\left\{\mathcal{F}\left[\frac{Q_1 \cdot U_{\text{in}}}{m}\right] \cdot Q_2\right\} \tag{2.27}$$

where $\mathcal{F}$ denotes a two-dimensional Fourier Transform, U_{in} is the input wavefield, m represents a scaling factor relating the sampling at the observation with the source plane, and Q_1, Q_2, Q_3 are the quadratic phase factors accounting for the phase changes taking place when propagating (Schmidt 2010). Each of these factors adds complexity at the source, during propagation and the observation plane, respectively. These facilitate the inclusion of diffraction and can be given by:

$$\begin{aligned} Q_1 &= e^{i\frac{k}{2}\frac{(1-m)}{Dz}(x_{\text{in}}^2+y_{\text{in}}^2)}, \\ Q_2 &= e^{-i\frac{2\pi^2 Dz}{mk}(f_x^2+f_y^2)}, \\ Q_3 &= e^{i\frac{k}{2}\frac{(m-1)}{mDz}(x_{\text{out}}^2+y_{\text{out}}^2)}. \end{aligned} \tag{2.28}$$

The quadratic factor Q_1 is a source plane correction aiming to adjust the phase by applying an initial curvature to the wavefront. Q_2 corresponds to the free-space propagation effects and modifies spatial frequencies according to how much each component propagates over the distance Dz. Finally the quadratic factor Q_3 adjusts the phase at the observation plane to ensure proper wavefront mapping. The inclusion of these quadratic factors is essential for accurate representation of the spatial frequency variations and resulting phase shifts and distortions (Schmidt 2010).

2.4.2 ELSiE - Extended Light Simulation Engine

ELSiE is an end-to-end Monte Carlo simulation tool developed at DLR with the aim of including Fresnel propagation and therefore achieving more realistic results for link budget calculations (Hristovski et al. 2024b). This light propagation simulator is a modular and therefore flexible tool, with a streamlined workflow as depicted in Figure 2.12. The main motivation behind the chosen tool is twofold: the angular spectrum

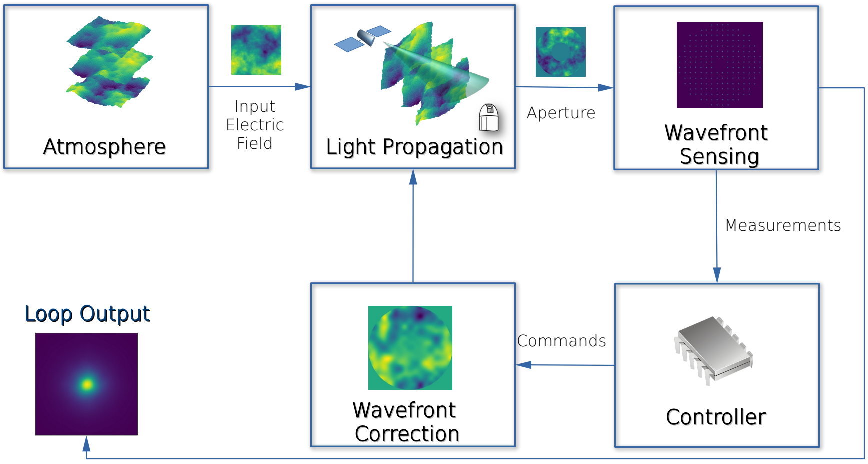

Figure 2.12: Workflow of modular light propagation simulation tool ELSiE.

propagation and the ease of integration of new control algorithms.

Light is assumed to enter the atmosphere as a plane wave, as the satellite is far from the top of the atmosphere relative to the beam size. It is propagated between atmospheric layers using either a geometric or physical propagation algorithm (e.g., angular spectrum). An aperture function is applied to the electric field distribution at the ground, and the result corrected by a simulated DM. The residual electric field is observed by a simulated Shack-Hartmann WFS (SH-WFS), using a full diffractive model and therefore including scintillation effects on sub-apertures. DM commands are computed from WFS using various prototype AO controllers. A delay of 2 frames is assumed between wavefront sensing and DM settling into commanded shape. The residual electric field is also simulated to be coupled into a single mode fibre (SMF) by performing an overlap integral with the SMF mode.

This simulator with ASP has been used to simulate finely uplink pre-distortion with ALPHASAT's TDP-1 (Hristovski et al. 2024b). The corresponding simulations results for received power at the satellite including scintillation were key towards the on-sky validation of the AO pre-distortion, in which performance was proven to be in the expected ballpark as is reported in (Hristovski 2025).

2.4.2.1 Diffractive WFS response

In simulation, there are two ways to represent a WFS and its response. The geometric WFS model treats each measurement as a linear mapping from phase to slopes. It uses a static matrix D to perpetuate the linear mapping. Whilst generally fast, it can miss effects from sampling and non-linearities. Moreover, it does not account for diffraction physics. And it therefore under represents scintillation. Instead, a diffractive model propagates the wavefront through the lenslet array and into the detector plane. Then, a centroiding algorithm reconstructs the measurements. These effects are modeled by dividing the complex field into the corresponding subapertures and computing a fast-Fourier-transform (FFT) per each pair, thus maintaining diffraction and scintillation effects.

The response of the diffractive WFS to a multi-layer example turbulent phase is show in Figure 2.13.

2.4.2.2 Zonal DM behaviour

The AO systems implemented at DLR use continuous DMs. These are characterized by a continuous mirror surface which is deformed by moving a discrete grid of actuators. The surface is thus mechanically coupled to the actuators in such a way that the movement of one actuator will affect the movement of neighboring actuators as well. The DM behaviour is therefore characterized by this inter-actuator coupling, and its response can be mapped into so-called DM influence functions. The zonal DM module in ELSiE was developed into the simulator in order to adequately emulate such hardware. In simulation, influence

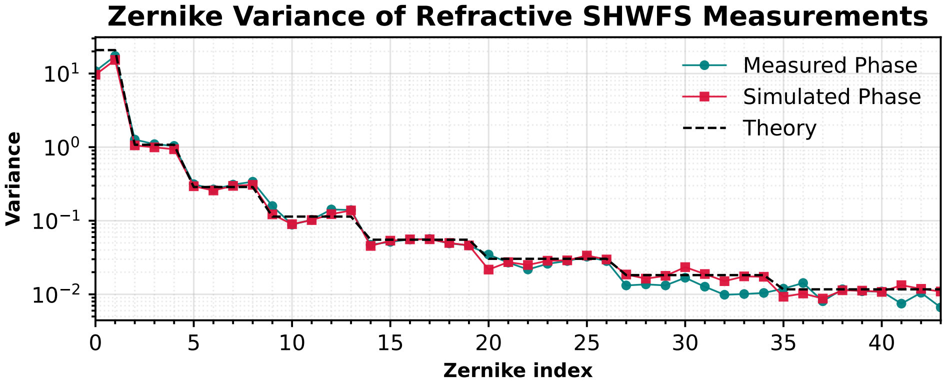

Figure 2.13: Zernike variance comparison between simulated phase, measured phase and theoretical expectation.

functions are often approximated by curves such as Gaussians or splines (Schmerbauch et al. 2020). A zonal representation with cubic splines was taken (Hristovski 2025).

In order to observe the effects of the spline influence functions on the DM, a waffle pattern was used as actuator commands onto the DM, and is shown here in Figure 2.14.

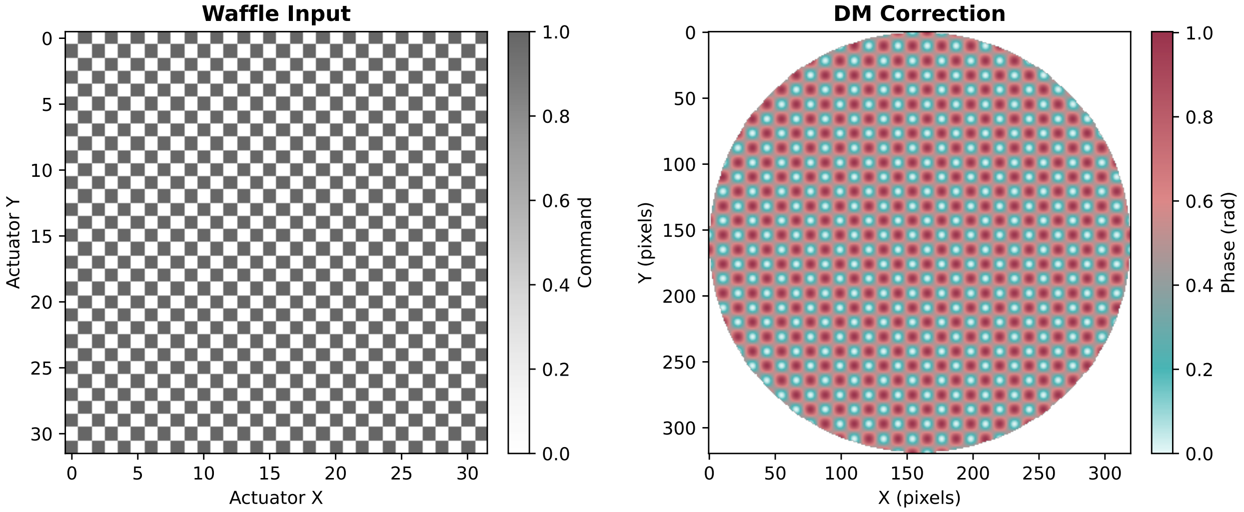

Figure 2.14: Plot of the DM response to a waffle input pattern.

In order to assess the effect of the correction, a phase screen with von Kármán statistics was generated and seen by the WFS. The corresponding measurements were then passed through the control matrix in order to project the correction commands onto the DM. This is shown in Figure 2.15.

2.5 Wavefront correction with Adaptive Optics (AO)

Light propagating through the atmosphere is subject to turbulence, leading to wavefront distortion. The resulting disturbance is wavelength independent. It is therefore possible to deploy AO systems to compensate for these distortions.

In the diagram of Figure 2.16, three optical paths can be distinguished. On the downlink path, light is directed from the deformable mirror into the wavefront sensor/ AO control path; a beamsplitter facilitates the coupling of light into a single-mode fibre. On the uplink path, the Tx laser is reflected from a fast steering mirror optimised for point-ahead angle, passing through the deformable mirror and therefore being launched with pre-distortion. In addition to the optical paths, the digital path for the AO control loop is highlighted. AO systems rely on digital sensors and controllers that sample the incoming wavefront at specific time intervals and issue actuator commands on a zero-order hold basis. Thus a discrete time approach is most adequate to reflect the discrete nature of signals within these systems (Kulcsár et al. 2006). Furthermore, an inherent characteristic of AO systems is the operational delay that happens between the WFS sensing and the DM correction. This delay is further evidenced in Figure 2.18.

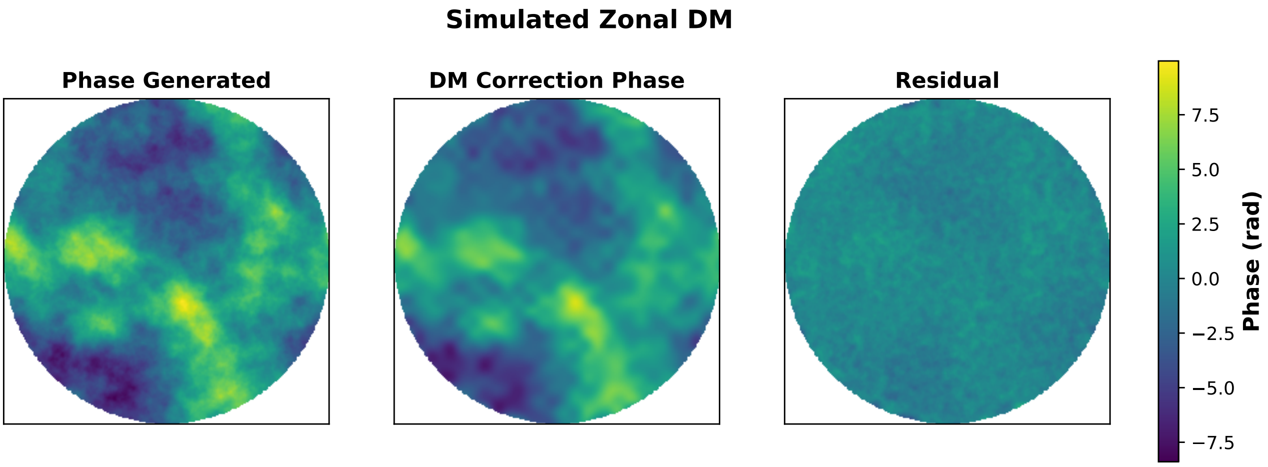

Figure 2.15: Plot to illustrate correction with the simulated zonal DM, showing the generated phase, the corresponding correction phase issued by the DM, and the resulting residuals.

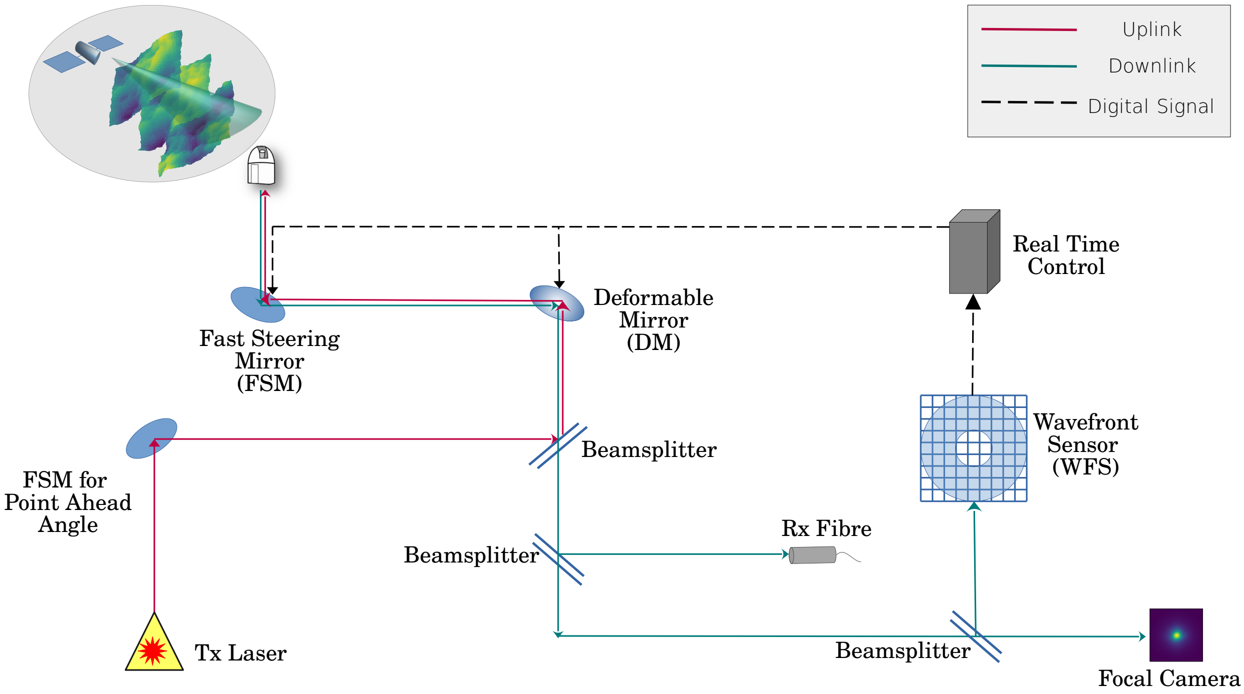

Figure 2.16: Diagram of an FSOC AO system showing uplink, downlink path and AO control.

2.5.1 Integral action control

The most widely used regulator in AO is the integral action controller, or integrator. It is reliant upon a calibrated matrix M_{int} called interaction matrix. This matrix is usually obtained by sequentially poking DM actuators and recording the corresponding measurements. It includes common-path aberrations and can therefore be defined as $M_{int} = DN$. This matrix is used to obtain the command matrix M_{com}:

$$M_{com} \triangleq M_{int}^{\dagger} = \left(M_{int}^{\mathrm{T}} M_{int}\right)^{-1} M_{int}^{\mathrm{T}} \tag{2.29}$$

where $\dagger$ represents the pseudo-inverse operation. With this, it is possible to define the AO integrator by:

$$u_k = u_{k-1} + g M_{com} y_k \tag{2.30}$$

where u is the command vector, g the integrator gain and y is the measurement vector. The integrator is simple to understand and easy to implement and has been extensively used in both astronomical and FSOC systems.

However, its performance is fundamentally limited. The unavoidable two-frame loop delay between WFS integration, data transfer, and DM settling introduces significant temporal error that remains unaddressed when deploying an integrator. When it comes to daylight operation under strong turbulence in conditions

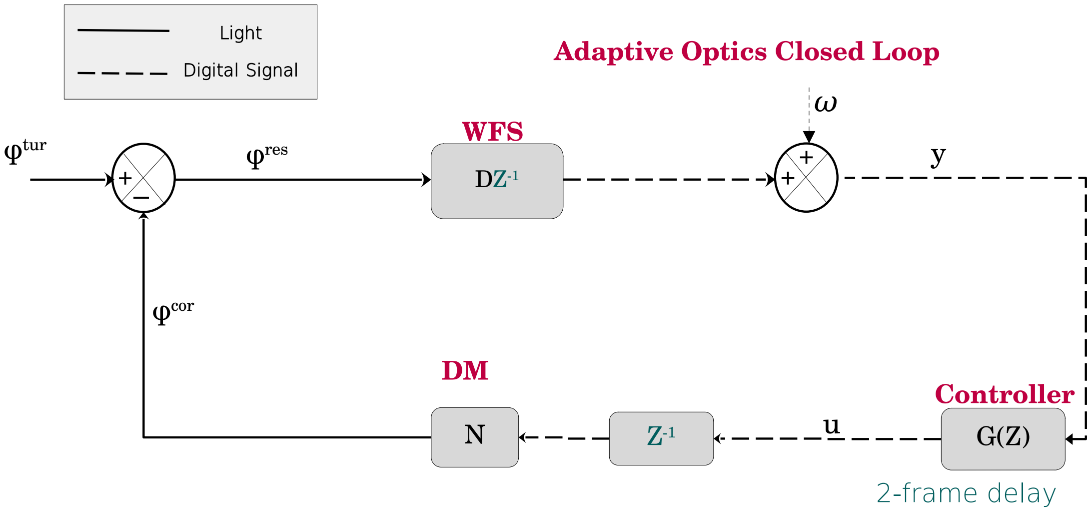

Figure 2.17: Block diagram of a closed loop AO system, with the discrete-time transfer function of the WFS and DM, including the 2-frame delay. D is the measurement matrix and N the DM influence functions matrix.

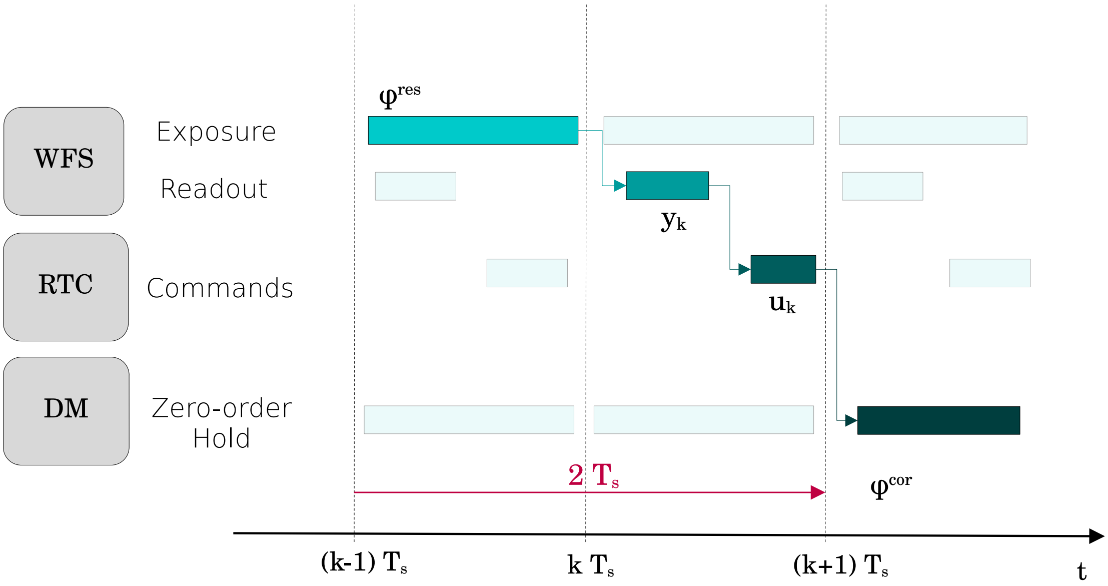

Figure 2.18: AO chronogram evidencing the 2-frame loop delay.

as described in section 2.3, scintillation causes missing or corrupted WFS measurements rendering the controller unstable and thus failing to maintain acceptable coupling efficiency into a single-mode fibre. Whilst in section 2.3 scintillation was said to be addressed by aperture averaging, its effects are nonetheless present in the WFS. The drops in intensity in the subapertures lead to degraded or missing measurements. These cause the integrator to get destabilized, interrupting operation and therefore effectively negating the communication link. Whilst lowering the integrator gain can increase the stability margin, this is achieved at the expense of reactivity and performance. Also to consider is the fact that the integrator incrementally reacts according to the measurement error gradient, which is inherently affected by the loop delay.

2.5.2 Linear Quadratic Gaussian (LQG) regulator

Predictive optimal controllers offer an attractive solution to minimising the effects of the operational delay for FSOC AO under straining conditions. Linear Quadratic Gaussian (LQG) regulators are controllers designed by minimizing a quadratic cost function. For AO systems which are accurately represented by a linear state model driven by Gaussian white noises, LQG control has been shown to minimize the variance of the residual phase ϕ^{res} (Roux et al. 2004; Kulcsár et al. 2006; Looze 2009; Kulcsár et al. 2012). This residual phase is the difference between the incoming phase ϕ and the correction phase ϕ^{cor} generated by the DM, that is, $\phi^{\text{res}} = \phi - \phi^{\text{cor}}$. When ϕ is a stationary, ergodic (i.e. time average converges towards an ensemble average), zero-mean stochastic process, the optimal control u_k minimizes the performance criterion

$$J_k^{\text{d}}\left(u_k\right) \triangleq \mathrm{E}\left(||\phi_k^{\text{res}}\,||^2 \mid \mathfrak{J}_k\right) \triangleq \operatorname{trace}\left(\operatorname{Var}\left(\phi_k^{\text{res}} \mid \mathfrak{J}_k\right)\right) \tag{2.31}$$

where $\mathfrak{J}_k$ is all the information available at time index k. It has been demonstrated that when a linear stochastic model is used for the disturbance, the optimal AO control problem is equivalently solved in discrete-time (Kulcsár et al. 2006, 2012). Here and throughout the course of this manuscript, x_k will denote the average of the continuous-time variable $x(t)$ over the sampling interval $(k-1)T_s \leq t < kT_s$. Considering the standard case of a 2-frame-delay (see Figure 2.17), and that the DM response is fast enough with respect to T_s, so that the correction phase can be written from the DM influence functions matrix N as $\phi_k^{\text{cor}} = N u_{k-1}$, the optimal control is given by

$$u_k \triangleq \arg\min_{u_k} \left(J_k^{\text{d}}\left(u_k\right)\right) = P_u \widehat{\phi}_{k+1|k} \tag{2.32}$$

where $P_u \triangleq N^{\dagger}$ represents the phase-to-commands projector, and the conditional expectation $\widehat{\phi}_{k+1|k} = \mathrm{E}(\phi_{k+1} \mid \mathfrak{J}_k)$ is the minimum-variance one-step-ahead prediction of ϕ_k knowing all past information up to time k. The optimal prediction problem is shown to be solved constructively using a Kalman filter based on a linear stochastic state-space model of the incoming disturbance and WFS measurement. For the AO case with the aforementioned assumptions the state-space model can be summarized by

$$\begin{aligned} X_{k+1} &= AX_k + \Gamma v_k \\ \phi_k &= C_1 X_k \\ y_k &= CX_k + w_k - M_{int} u_{k-2} \end{aligned} \tag{2.33}$$

where A, Γ and C_1 define a chosen disturbance model based on priors and C the WFS measurement model, while v and w are mutually independent zero-mean vector-valued Gaussian white noises, with covariance matrices Σ_v and Σ_w respectively. The interaction matrix M_{int} can be expressed as a function of the WFS matrix D and the influence functions matrix N as $M_{int} = DN$. The optimal disturbance prediction is then obtained as $\widehat{\phi}_{k+1|k} = C_1 \widehat{X}_{k+1|k}$, where $\widehat{X}_{k+1|k}$ is computed in real time as:

$$\widehat{X}_{k+1|k} = \left(A - L_\infty C\right) \widehat{X}_{k|k-1} + L_\infty \left(y_k + M_{int} u_{k-2}\right) \tag{2.34}$$

In this recursive equation, L_∞ is the asymptotic Kalman gain, which is given by:

$$L_\infty = A \Sigma_\infty C^{\mathrm{T}} (C \Sigma_\infty C^{\mathrm{T}} + \gamma \Sigma_w)^{-1} \tag{2.35}$$

where Σ_∞ is the asymptotic prediction error covariance matrix and γ is the so-called fudge factor allowing for filter tuning. Modifying the measurement noise variance in the Kalman filter is commonly used to absorb model discrepancies, see, e.g. (Petit et al. 2009; Sivo et al. 2014; Sinquin et al. 2020) for its use in AO. The matrix Σ_∞ is computed as the unique solution of the Discrete Algebraic Riccati Equation that writes

$$\Sigma_\infty = A \Sigma_\infty A^{\mathrm{T}} + \Gamma \Sigma_v \Gamma^{\mathrm{T}} - A \Sigma_\infty C^{\mathrm{T}} (C \Sigma_\infty C^{\mathrm{T}} + \gamma \Sigma_w)^{-1} C \Sigma_\infty A^{\mathrm{T}}. \tag{2.36}$$

In practice, the implementation of the regulator boils down to the Kalman filter (Equation (2.34)) and a static command matrix multiplication to recover the predicted phase from the state prediction $\widehat{X}_{k+1|k}$. Concerns about real-time computational burden when compared to the integrator are common. Its has however been demonstrated that the critical real-time path from measurements to applied commands is of the same complexity as the integrator (Marquis 2023). Any additional calculations can be precomputed or parallelized outside the critical loop. As an example, a fully decoupled LQG regulator has already been demonstrated at rates as high as 8 kHz, showing that predictive control can be used at very high rates on a large system (Poyneer et al. 2023).

2.6 Performance Parameters

2.6.1 Power Scintillation Index, PSI

The *power scintillation index* quantifies the normalized variance of power fluctuations received over a finite aperture in the presence of atmospheric turbulence. It is defined as:

$$\sigma^2_{I,\text{ap}} = \frac{\langle P^2 \rangle - \langle P \rangle^2}{\langle P \rangle^2} \tag{2.37}$$

where P is the total optical power collected by the aperture, $\langle P \rangle$ is the mean power, and $\langle P^2 \rangle$ is the mean squared power. PSI reflects the impact of spatial averaging due to the aperture size, which mitigates turbulence-induced intensity fluctuations. Larger apertures reduce the scintillation effect by averaging over multiple spatially uncorrelated turbulence cells, leading to a lower power scintillation index. Unlike the scintillation index, which is theoretical and assumes an infinitesimally small aperture, the power scintillation index directly accounts for practical aperture-dependent effects in FSOC systems (Andrews et al. 2005).

It is important not to conflate the PSI with the physical phenomena of scintillation, which refers to the temporal and spatial fluctuations of optical intensity caused by refractive-index variations.

2.6.2 Coupling efficiency and coupling loss

Coupling efficiency η is the fraction of collected optical power coupled into the single-mode fiber. It is expressed in linear units (0–1) or percent (0–100%).

$$\eta = \frac{P_{\text{coupled}}}{P_{\text{incident}}} = \frac{\left\langle \left| \int_A U_i(\mathbf{r})\, U_m^*(\mathbf{r})\, d\mathbf{r} \right|^2 \right\rangle}{\left\langle \int_A |U_i(\mathbf{r})|^2 \, d\mathbf{r} \right\rangle} \tag{2.38}$$

where $U_i(\mathbf{r})$ represents the incident optical field in the receiver plane, and $U_m^*(\mathbf{r})$ represents the normalized fibre mode profile. Therefore the efficiency is measured by an overlap integral over the aperture: the better the match between the incoming field and the fiber mode, the higher the coupled power.

Coupling loss L is the same quantity expressed in dB. This is the most standard performance parameter used when reporting results in the context of FSOC AO and channel modeling. It can be calculated from the efficiency with:

$$L = 10 \log_{10}(\eta) \tag{2.39}$$

L is always negative as it represents the loss relative to incident power.

2.7 Summary

In this chapter, the fundamental theoretical framework which serves as the basis for the remainder of the thesis is presented, and thus serves a way to contextualise the development (chapter 3) and novel results chapters (4 and 5).

An overview on optical propagation through atmospheric turbulence highlighted the need to consider diffraction in near-field propagation. The resulting degradation of optical links and the particularities of up and downlink with satellites native to different orbits is considered, establishing the need for the use of an adequate simulation environment that accounts for scintillation. The simulator is detailed, together with the implementation of physical propagation via angular spectrum method. Wavefront correction with AO is addressed, and the theory behind the proposed predicted controller is summarized. Lastly, the parameters which are used in this thesis as performance metrics are shown.

Chapter 3

Development and integration of predictive control within end-to-end simulation

3.1 Initial LQG implementation

Throughout the course of this thesis, the simulator ELSiE developed in-house at DLR was used. This simulator was developed solely with integral action control in mind. Therefore, it was necessary to develop predictive control tools compatible with the existing simulation software. Whilst the simulator had a complete end-to-end modular approach, with a validated integrator and AO loop, it was necessary to develop the loop code further in order to assure compatibility with predictive control. Therefore, a step-by-step approach towards developing and validating a predictive control software tool was taken. Initially, a cross-validation with integrator was made. This validation ensured both the architecture of the LQG controller and its compatibility inside the AO loop. It was then possible to proceed with methods to generate the theoretical priors model as well as ensure accurate zonal phase reconstruction, implement Kalman gain calculation algorithms and finally develop a projection method to extract the phase prediction from the state vector and project it onto the DM. Whilst each new development was tested and validated independently, a final cross-validation was performed. For this, the performance of published simulated work with the OOMAO simulator (Conan et al. 2014) was matched (Prengère et al. 2020). This provided a strong foundation with which to build a control module fully compatible with ELSiE, which was validated at each incremental step. Following the validation, these tools were initially used to simulate an horizontal link. This simulation environment provided a performance comparison between geometric and angular spectrum propagation to assess the influence of scintillation. The next sections summarise this process.

3.1.1 State-space control validation with integrator

In order to validate the implementation of the LQG and its correct interaction with the simulation tools, its performance was cross-validated with that of the ELSiE integrator. The integral action control included in the simulator has been shown to match theoretical expectations (Hristovski et al. 2024b). Therefore, the LQG implementation can be validated by simply taking the Kalman Filter shown in equation (2.34) and rewriting it in state-space form as

$$\begin{aligned} X_{R,k+1} &= \mathrm{M}_1 X_{R,k} + \mathrm{M}_2 y_k + \mathrm{M}_3 u_{k-2} \\ u_k &= \mathrm{M}_4 X_{R,k+2} \end{aligned} \tag{3.1}$$

where $\mathrm{M}_1 = (\mathrm{A} - L_\infty C)$, $\mathrm{M}_2 = L_\infty$, and $\mathrm{M}_3 = L_\infty M_{int}$. Using this notation, it is possible to reproduce exactly an integrator (see equation (2.30)) by simply replacing $\mathrm{M}_1 = [I]$, where I is an identity matrix of appropriate dimensions, $\mathrm{M}_2 = gM_{com}$, where g is the integrator gain and M_{com} the control matrix, $\mathrm{M}_3 = [0]$ and finally $\mathrm{M}_4 = [I]$, so that $X_{R,k} = u_k$. Running both integral controller architectures on the same phase screens and without WFS noise should result in the exact same closed-loop time series. These results are shown here in Figure 3.1. This cross-validation provided confirmation that the newly developed

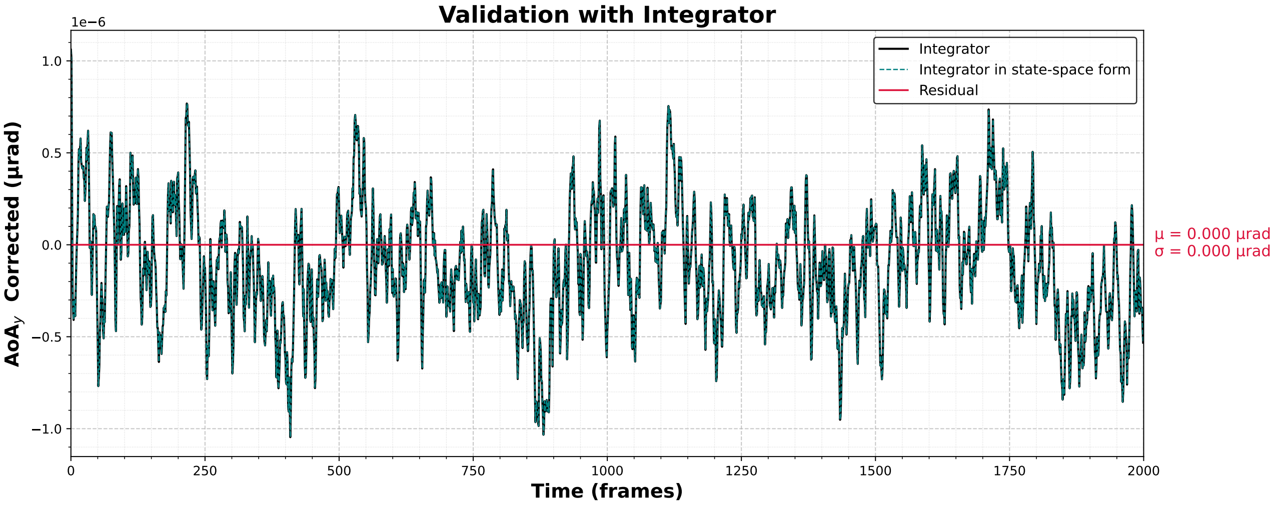

Figure 3.1: Time series of the angle of arrival for the standard integrator and an integrator in state-space form, under the same conditions. Both time series perfectly overlap, leading no residuals between the two. This is shown with the residual line, with highlighted mean and standard deviation of pure zero.

Kalman filter implementation was correct. Furthermore, it also provided AO loop validation, the algorithm of which had to be adapted in order to generate and access internal variables required for LQG control.

3.1.2 LQG synthesis

With the validation of the loop and general integration of the Kalman filter equation into the simulation, it was now possible to move forward with the different building blocks needed in order to generate the priors models, calculate the Kalman gain, and ultimately implement a full LQG. The following subsections introduce the methodology that was followed towards LQG synthesis.

3.1.2.1 Disturbance modeling and priors

The Kalman filter requires a priors model in order to output a state prediction. Several methods can be chosen to obtain an adequate model of the incoming wavefront, ranging from purely theoretical (Roux et al. 2004) to entirely data-driven and data-based (Sinquin et al. 2020). It is also possible to have the wavefront ϕ represented via an orthogonal basis of optical modes (usually Zernike of Karhunen-Loève modes) or on a zonal basis. However, due to the constraint that all modes are normalized on a finite circular aperture, higher-order Zernike modes concentrate more of their spatial variation and therefore larger amplitudes at the edge of the pupil (Mahajan 1994). A zonal basis representation samples the phase over a regular grid of phase points taken over the telescope pupil. Whilst orthogonal basis can lead to leaner calculations, a zonal basis naturally encodes frozen flow as wind translation directly corresponds to a spatial phase shift. Moreover, it can also accurately represent high spatial frequencies according to the chosen spatial sampling period. With this in mind, a zonal representation following (Correia et al. 2015; Prengère et al. 2020) was used.

The incoming wavefront model was derived from the standard von Kármán statistics (see section 2.2.3.1) and the frozen-flow Taylor hypothesis (see section 2.1.3). According to the frozen flow assumption, atmospheric turbulence is spatially discretized as a finite number of thin layers, each of which exhibits von Kármán spatial statistics and is moving with constant speed and direction (Roddier 1999).

In order to represent the phase in a zonal basis with theoretically derived priors, the covariance matrices were used. The covariance matrices are filled with values from the von Kármán phase structure function (see Equation (2.26)). Piston mode is removed from the covariance calculations. This is done with the SH-WFS in mind which by nature cannot detect piston changes. If piston mode is not removed, the LQG regulator results would not change provided the fudge factor γ is tuned, as the signal-to-noise ratio of the LQG regulator drives the filter behaviour. Therefore, the variance-covariance matrix $\Sigma_\phi = \mathrm{Var}(\phi_k)$ of the

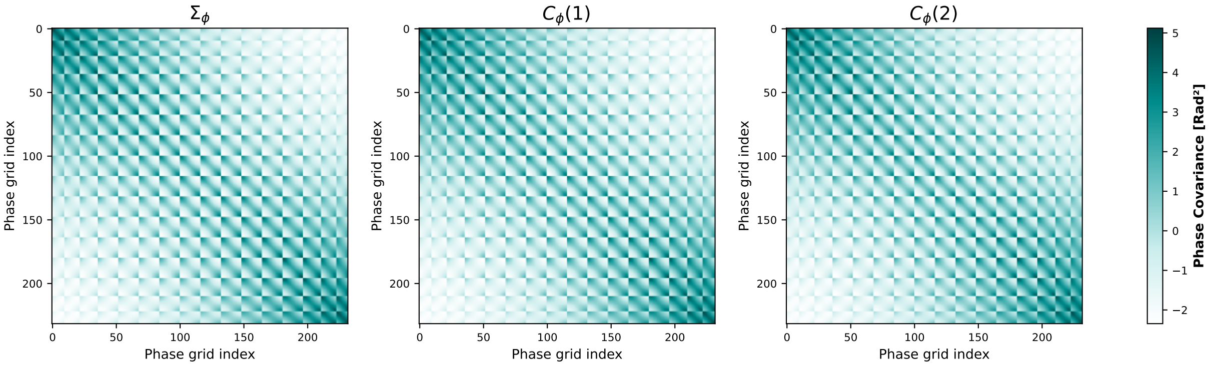

Figure 3.2: Variance-covariance matrix Σ_ϕ, and the cross-covariance matrices $C_\phi(1)$ and $C_\phi(2)$ generated from von Kármán structure function. Within these matrices a repeated rectangular pattern is visible, which is a product of generating the covariance matrices over a discrete grid of points. Their structure is visibly diagonal, which is expected of stronger turbulence scenarios as the spatial decorrelation is more accentuated. Furthermore, these matrices were generated on a circular grid leading to differences in size of the observed rectangular structures which are smaller around the edge of the matrices.

phase points in the telescope's pupil is computed from the phase structure function. Combining the von Kármán phase structure function and the frozen-flow assumption also enables the computation of the temporal cross-covariance matrices $C_\phi(1) = \mathrm{Cov}(\phi_{k+1}, \phi_k)$ and $C_\phi(2) = \mathrm{Cov}(\phi_{k+2}, \phi_k)$. This is possible because the Von Kármán model provides spatial correlations while the frozen-flow assumption converts time steps into equivalent spatial shifts. The resulting matrices are shown in Figure 3.2. Their structure speaks to the spatio-temporal correlations, as the further apart in time the phase shift, the faster the decorrelation. Hence, the diagonal components are stronger on the autocovariance matrix then the temporal cross-covariance matrices.

The next step is to match these spatio-temporal statistics to a vector-valued auto-regressive stochastic model of order 2 in the form:

$$\phi_{k+1} = A_1\phi_k + A_2\phi_{k-1} + v_k. \tag{3.2}$$

The parameters of this model are the matrices A_1, A_2 and the disturbance noise covariance matrix Σ_v. Matching the values of $C_\phi(1)$, $C_\phi(2)$ computed from this AR(2) model with the values given by the frozen-flow model amounts to solving the so-called Yule-Walker equations for the unknowns A_1, A_2 (depicted in Figure 3.3) and Σ_v (depicted in Figure 3.4). To achieve this, the AR(2) model is put in the standard state-space form:

$$\begin{aligned} X_{k+1} &= AX_k + \Gamma v_k = \begin{pmatrix} A_1 & A_2 \\ I & 0 \end{pmatrix} X_k + \begin{pmatrix} I \\ 0 \end{pmatrix} v_k, \; X_k = \begin{pmatrix} \phi_k \\ \phi_{k-1} \end{pmatrix} \\ \phi_k &= C_1 X_k = \begin{pmatrix} I & 0 \end{pmatrix} X_k. \end{aligned} \tag{3.3}$$

In the steady-state regime, the covariance matrix of X_k is equal to

$$\Sigma_X = \begin{pmatrix} \Sigma_\phi & C_\phi(1)^{\mathrm{T}} \\ C_\phi(1) & \Sigma_\phi \end{pmatrix}. \tag{3.4}$$

The values of A_1, A_2 are then given by

$$\begin{pmatrix} A_1 & A_2 \end{pmatrix} = \begin{pmatrix} C_\phi(1) & C_\phi(2) \end{pmatrix} \Sigma_X^{-1} \tag{3.5}$$

Finally, the value of the noise covariance Σ_v is deduced from the identity $\Gamma\Sigma_v\Gamma^{\mathrm{T}} = \Sigma_X - A\Sigma_X A^{\mathrm{T}}$. The final structure is shown here in Figure 3.4. The stability of the discrete-time system is assured when all eigenvalues of A are inside the unit disk on the complex plane. This is normally referred to as Schur stability, and A is said to be Schur stable if and only if all its eigenvalues have modulus strictly less than one (Ogata 1995).

The Yule-Walker equations presented here can be used whatever the chosen phase basis. They have been proposed in classical AO for satellite applications in (Prengère et al. 2020) with a zonal basis, have been used for similar applications with a Zernike basis (Robles et al. 2022) and could also be considered with, e.g., a Karhunen Loève basis. In this project, since there is no analytical expression of the phase covariance, variance and covariance matrices will need to be computed numerically from the structure function.

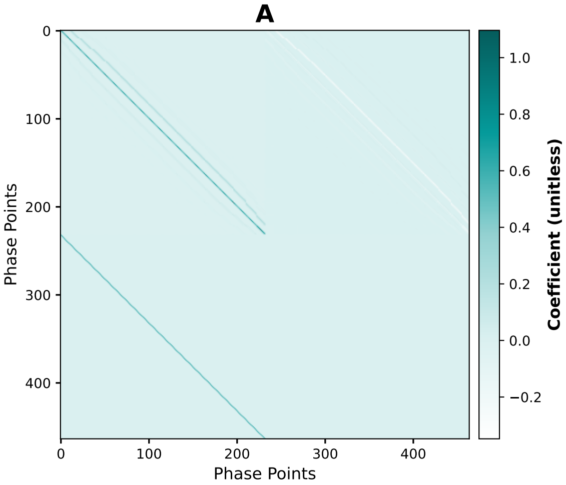

Figure 3.3: Example structure for the final A matrix in an AR2 model. It contains the A_1 and A_2 matrices on the top, and an identity matrix I and a zero matrix on the bottom. The diagonal lines on the A coefficients help carry out the dynamics of the phase, whilst the identity matrix on the bottom ensures phase memory within the state vector.

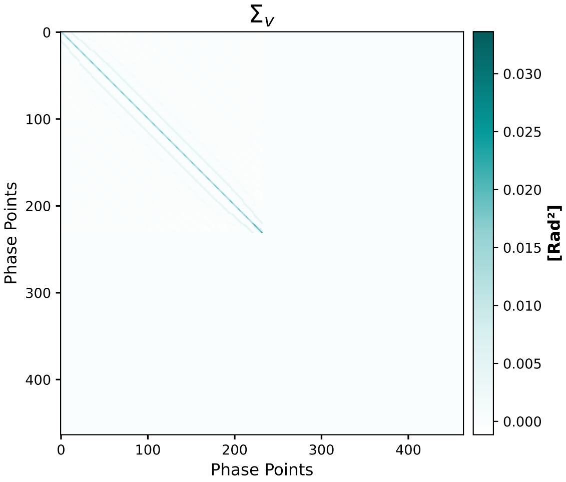

Figure 3.4: Example structure for the noise covariance calculated from the A matrix above.

3.1.2.2 Measurement noise covariance matrix

The calculation of the Kalman gain (Equation (2.35)) requires previous knowledge of the measurement noise covariance matrix Σ_w. This matrix is dependent on the WFS response, and can be challenging to obtain for real AO systems. In order to accurately represent measurement noise covariance in the simulation, a simplified method inspired by to the one described in (Marquis 2023) was taken.

The measurement noise covariance matrix corresponds to the mathematical expectation of $w_k w_k^T$, i.e. $\Sigma_w = \mathbb{E}\left(w_k w_k^T\right)$. Detector noise can be approximated by a Gaussian distribution in high photon flux scenarios. Since w_k is assumed to be spatially uncorrelated and zero-mean, its covariance matrix is diagonal, where the diagonal values are the noise variances corresponding to WFS subapertures measurements

$$\Sigma_w = \operatorname{diag}\left(\hat{\sigma}_{w,1}^2,\ \hat{\sigma}_{w,2}^2,\ \dots,\ \hat{\sigma}_{w,n_y}^2\right), \tag{3.6}$$

with n_y the total number of measurements (two values, x- and y-slope, per subaperture). To obtain empirically these noise variance values, the static flux map corresponding to the illumination footprint was considered, and a flux threshold of 75% was applied to account for the partially illuminated subapertures (lower signal-to-noise ratio) while excluding the invalid ones. The subaperture mask affected by this pupil illumination is shown in Figure 3.5a). This methodology ensured only subapertures generating valid measurements at every frame were considered in the noise estimation, and that the subapertures that are more prone to SNR variations are assigned a higher measurement noise variance. A sequence of simulated open-loop turbulence was then generated and propagated through the SH-WFS. The temporal Fourier transform of each subaperture signal was computed, and the corresponding power spectral density (PSD) was estimated. The noise contribution was isolated by averaging the high-frequency region of the spectrum, as this is where the turbulence power becomes negligible and a plateau appears which is dominated by detector noise. The resulting level was scaled by the number of frames to produce a variance estimate. Finally, the per-subaperture variances were assembled into the diagonal noise covariance matrix, a zoomed-in version of which is shown in Figure 3.5b).

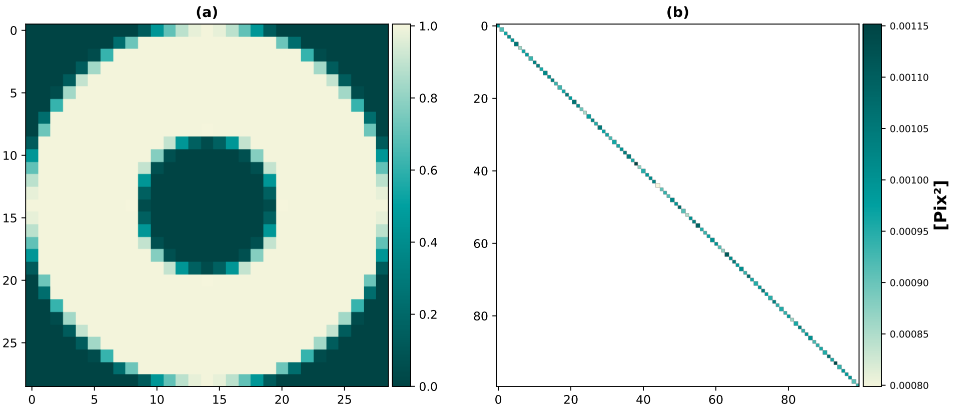

Figure 3.5: (a) Subaperture mask affected by the pupil illumination footprint; and (b) resulting measurement noise covariance matrix for the first 100 measurements.

Two important considerations for this methodology should be noted. First, FSOC-AO systems are by nature very photon rich, especially when compared with photon-starved applications such as astronomical observations. This results in a substantial signal-to-noise ratio that is many orders of magnitude higher than those experienced in traditional astronomical AO systems. Furthermore, the introduction of the fudge factor γ in equation (2.35) relaxes the need for precise amplitude estimation of the noise matrix. In fact, given that γ can scale the overall level while preserving the proportion, only the relative distribution of noise across subapertures matters. Future lab implementations will most certainly require a more refined approach, such as the steps shown in (Marquis 2023) for noise characterisation, especially accounting for potential pupil rotation.

3.1.2.3 Geometric WFS model matrix

In AO systems, the WFS matrix D is the linear operator that is constructed from the geometric model and that relates the slopes measured by the WFS and the phase. The WFS matrix D is dependent on the computational grid chosen to represent the phase. The AO system in consideration follows the so-called

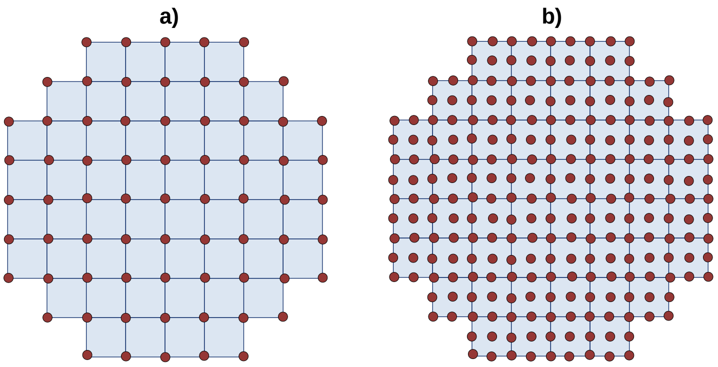

Figure 3.6: (a) Example of a WFS grid overlayed with a simple phase grid in Fried Geometry, where each red dot represents a phase point in a blue subaperture; and (b) Similar overlay but with oversampled phase grid by a factor of 2.

Fried geometry. This refers to the positioning of the DM actuators relative to the SHWFS. In this geometry, actuators are mapped in the pupil to a position corresponding to the edge of the subaperture. This is shown in Figure 3.6a). As the goal is to command the actuators so that the best phase correction is generated, it is logical to position the phase points on a grid corresponding to the actuators location. However this grid can be oversampled, as shown later in section 4.3.1. In order to build the D matrix, it is necessary to follow a weighted average approach along the subaperture edges. This results in a subaperture kernel that can be applied per subaperture. The kernel of the resulting weights for an oversampling factor of 2 corresponding to the one demonstrated in Figure 3.6b) is shown in Figure 3.7.

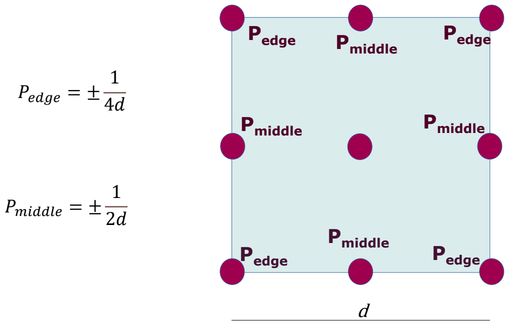

Figure 3.7: Building the subaperture kernel for an oversampling factor of 2.

The code for generating the operator D can be implemented in a such a way that makes it applicable to any desired oversampling factor. Such a generalization consists of a convolution of the kernel of weights with the subaperture grid. The weights can be calculated by generalizing the expressions shown above in Figure 3.7 into the form:

$$\begin{cases} P_{\text{edge}} = \pm\frac{1}{d}\cdot\frac{1}{2(n_{os}+1)} \\ P_{\text{middle}} = \pm\frac{1}{d}\cdot\frac{1}{(n_{os}+1)} \end{cases} \tag{3.7}$$

where d is the subaperture diameter, and n_{os} the oversampling factor. This generalized implementation was developed and implemented in order to future-proof the software and facilitate investigation into oversampling methods as well as quantifying their advantages and computational burden. This matrix generation was cross-checked with the one utilized for the development of the work reported in (Prengère et al. 2020). The final results of this cross-validation are shown in section 3.1.3.

3.1.2.4 Phase projection

In order to complete the LQG controller implementation it is necessary to define the projection matrix that projects the predicted phase onto the actuators space. From section 2.5.2, it was shown that the predicted phase $\widehat{\phi}_{k+1|k}$ can be obtained from the state prediction $\widehat{X}_{k+1|k}$ with C_1. The command vector u_k can thus be obtained from equation (2.32) with

$$u_k = P_u C_1 \widehat{X}_{k+1|k}. \tag{3.8}$$

When access to the DM influence matrix N is available, the projector $P_u = N^{\dagger}$ can be computed. Implementing this projector for a real AO system requires a pseudo-synthetic interaction matrix. This procedure is explained in (Heritier-Salama 2019; Marquis 2023). A simple way to get around computing projector P_u with resorting to a pseudo-synthetic interation matrix is to take advantage of the WFS matrix D (section 3.1.2.3) and the command matrix M_{com} (section 2.5.1) as proposed in (Vidal et al. 2010; Sivo et al. 2014):

$$P_u \triangleq M_{com} D. \tag{3.9}$$

Since M_{com} is the pseudo-inverse of the interaction matrix M_{int}, this projector requires knowledge of M_{int}, which can be calibrated, and is therefore a simpler solution in practice. Although it is a sub-optimal solution when considering the minimisation criterion (equation (2.31)), a projector built directly from M_{int} will intrinsically be robust to system misalignments, whereas obtaining N from a real system would require more complex calibration procedures (Sivo et al. 2014). Furthermore, it has been shown that for the case where where DM and WFS relative positioning respect Fried geometry, both projectors obtain similar performance (Marquis 2023). Therefore, in this thesis the $M_{com}D$ projector was used.

3.1.3 Cross-validation geometric simulation with OOMAO

In order to verify the implementation, a cross-validation with the work published in (Prengère et al. 2020) was performed. In this paper, a simulation of LEO satellite tracking was evaluated with an integrator and several different LQG regulators. The conditions reported in the paper for the LEO satellite simulation were replicated, and two different controllers were simulated, namely an integrator and an LQG controller. The latter relies on a multi-layer zonal-based autoregressive turbulence models as has been explained throughout section 3.1.2. In the work reported in (Prengère et al. 2020), OOMAO was used to simulate the conditions, and the simulations were run in a geometric environment, with a geometric WFS. Whilst with ELSiE it was possible to replicate the geometric propagation, the ELSiE WFS is refractive. The simulations were run for 5 seconds at 2 kHz for each of the regulators, and the time series for the closed-loop Strehl ratio was recorded. The results for an integrator and LQG regulator under matching conditions to those described in the paper are shown in Figure 3.8.

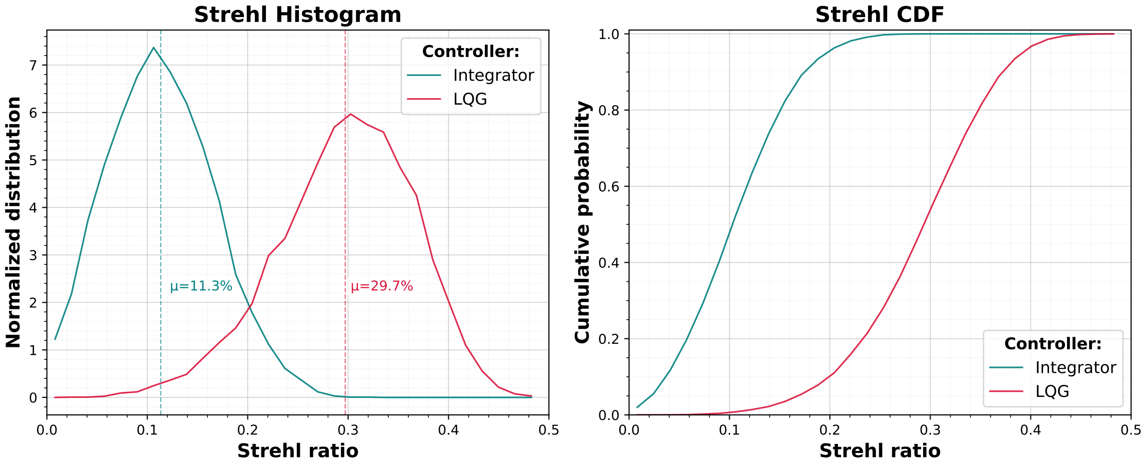

Figure 3.8: Replicated results for integral action control and zonal LQG controller with AR(1).

The histogram from Figure 3.8 reveals two distributions with quite different performance, with the LQG controller outperforming the integrator. This is also apparent on the CDF plot on the right hand side of Figure 3.8. The integrator achieved a mean Strehl ratio of 11.3%, which is very comparable to the 10.4% mean Strehl ratio obtained by (Prengère et al. 2020). The AR(1) LQG regulator here shown is comparable to the SA-LQG (Correia et al. 2015), reported as controller 6 in the published study used for the cross-validation. Here it achieved a mean Strehl ratio of 29.7%, very comparable to mean 28.3% reported in the OOMAO study.

These results accurately replicate the simulation results reported in (Prengère et al. 2020), despite the simulation environment differences. This replication of results confirms the validity of the simulation tools developed for this project. With this validated, it was possible to summarize all the developments here reported into a python library for predictive controllers: CHAOS. The next sections summarize the final architecture, highlight some of the modules and show the final simulation pipeline.

3.2 CHAOS (Control for High-performance Adaptive Optics Systems) summary

In order to simulate an LQG with ELSiE, it was necessary not only to develop the tools specific to the LQG synthesis but also to ensure their efficient use of the simulator itself. The work developed throughout the course of the years was eventually compiled into a single Python library for controller synthesis. As shown in Figure 2.12, the simulator engine ELSiE outputs measurements, which are expected to be processed by a controller in order to produce commands. The following sections detail the library and its intended workflow towards implementing and tuning an LQG controller. (At this time, the tool is not available for public use due to institutional restrictions.)

3.2.1 Simulation wrapper

In order to easily develop and tune the controllers, several ELSiE modules had to be used independently. To facilitate the task, a simulation wrapper was created to configure the required simulator objects via a configuration file. This wrapper includes a simulation configurator that sets up the simulation objects correctly and exposes them to the simulation environment. Figure 3.9 summarizes the configuration.

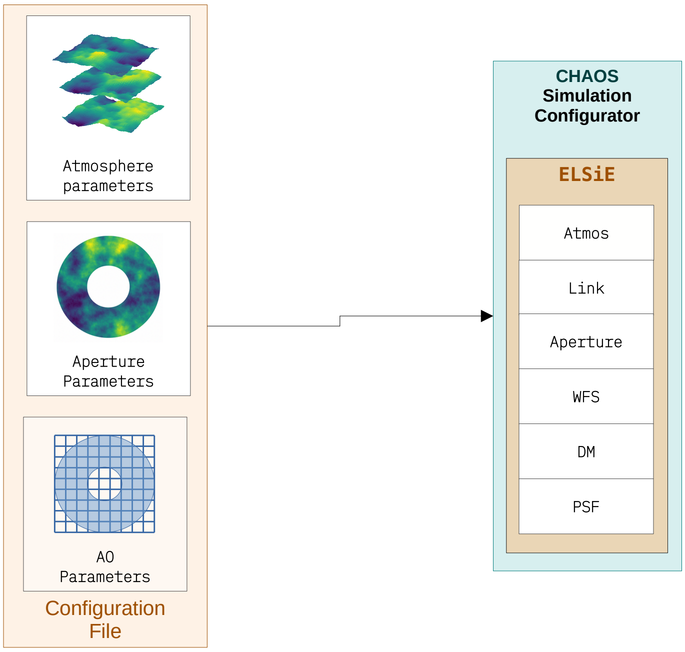

Figure 3.9: Illustration of the simulation configurator class within the simulation wrapper module from CHAOS.

An example of loading the ELSiE simulation using its wrapper for CHAOS is shown in the code block below.

```python
# loading the simulator with the configuration
simulator = simulation_wrapper.SimulationConfigurator(config_file)

# generating the needed objects
atmos = simulator.atmosphere()
aperture = simulator.telescope_aperture()
link = simulator.link_propagator()
wfs = simulator.wavefront_sensor()
dm = simulator.zonal_deformable_mirror()
psf = simulator.point_spread_function()
```

With the objects for simulation now available, it is possible to proceed with synthesizing an LQG regulator, starting with the Kalman filter.

3.2.2 Kalman filter synthesis

Figure 3.10 provides an overview of the workflow from the tool CHAOS towards Kalman filter implementation in order to achieve LQG controller synthesis. The process begins with a configuration file in which the atmosphere parameters are detailed. These parameters serve as inputs towards the module "Disturbance Modeling". This module contains the implementation of the von Kármán phase structure function (Equation (2.26)) with which it is possible to calculate covariance matrices. The covariance matrices can then be used as inputs to the Yule-Walker equations detailed in section 3.1.2.1, leading to a complete autoregressive model. Using this module therefore allows to build a priors model from the atmospheric parameters detailed in the configuration file.

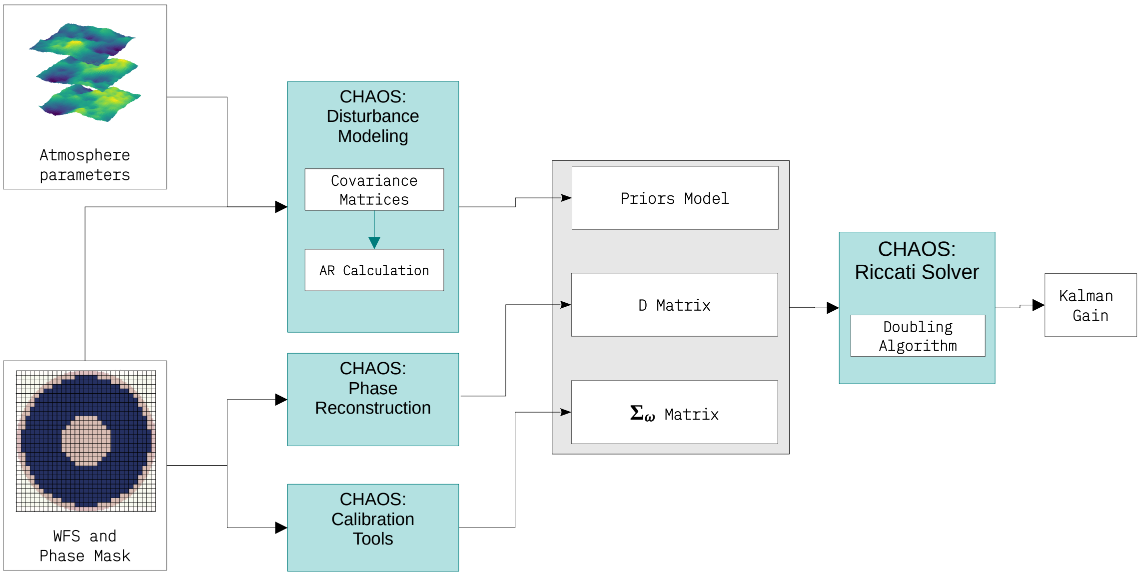

Figure 3.10: Flow chart illustrating the workflow towards Kalman gain calculation using the modules implemented in the library CHAOS.

It is then necessary to complete the measurement model (Equation (2.33)). In order to do so, the WFS matrix is built. This is made possible with the module "Phase Reconstruction" by taking configuration parameters for the WFS and the simulated phase grid. With a class implementing the procedures detailed in section 3.1.2.3, the matrix D can be generated. The calibration tools module implements the necessary steps to obtain the measurement noise covariance matrix (detailed in section 3.1.2.2).

Finally, it is necessary to solve the Riccati equation in order to obtain the Kalman gain. This was done by implementing a doubling algorithm (Lainiotis et al. 1994), which has been shown to be an extremely efficient Riccati solver. With this final output, all the parts necessary towards implementing a Kalman filter are generated.

3.2.3 LQG regulator tuning

Tuning the LQG regulator is primarily done by testing different fudge factor γ values to affect the measurement noise covariance matrix, and recalculating the Kalman gain. As was explained in section 2.5.2, the fudge factor allows also to efficiently compensate for potential model mismatch by adjusting the filter's signal-to-noise ratio. However, the phase-to-commands projector uses the command matrix $M_{com} = M_{int}^{\dagger}$ and thus is also subject to a varying conditioning, which is done by truncating the singular values of the singular value decomposition (SVD) of M_{int}. It is therefore necessary to tune both the fudge factor and the singular values truncation level simultaneously. An illustration of this process is shown in Figure 3.11.

Using the process previously detailed in Figure 3.10, it is possible to obtain the priors for disturbance model (matrices A and Σ_v), the WFS matrix D and the measurement noise covariance matrix Σ_w. The

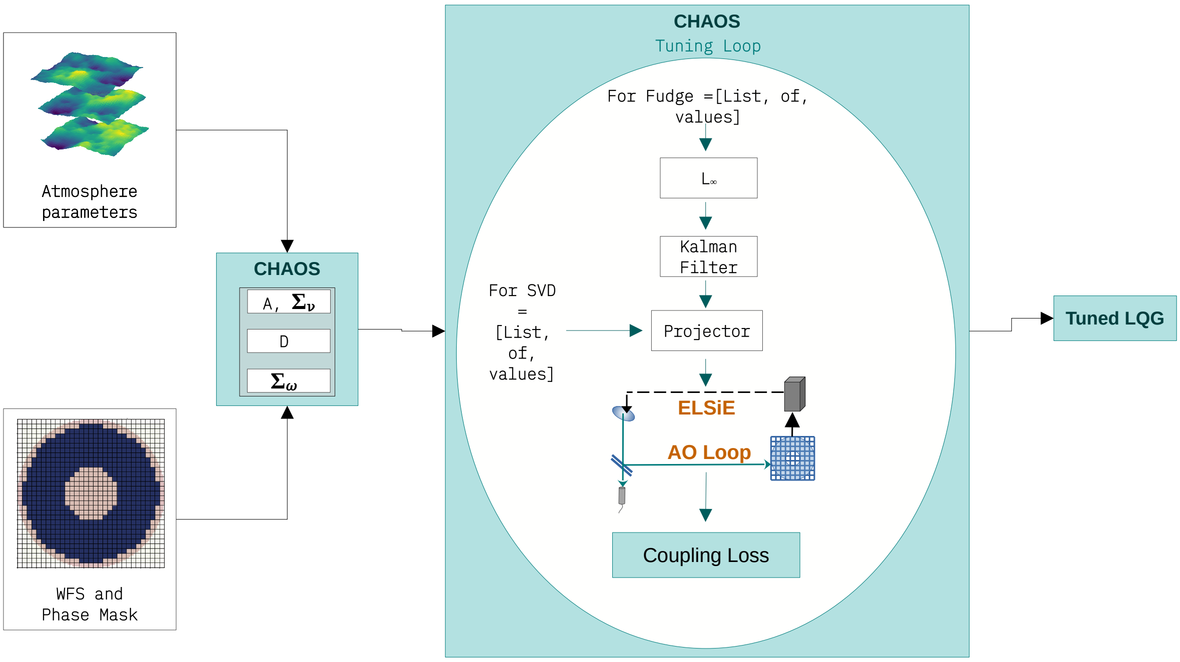

Figure 3.11: Flow chart illustrating the workflow of tuning an LQG controller.

tuning is then done for both the fudge factor and the SVD conditioning value with the rule of maximizing fibre coupling efficiency. The resulting LQG regulator (Kalman filter plus projector) is used as controller in the AO loop and the closed-loop coupling efficiency time series are recorded. The final values for running the full simulations are chosen according to the best mean and median coupling efficiency obtained. In order to make the tuning process as efficient as possible, a simulation configurator was developed to make the simulator objects readily available.

3.2.4 Final simulation pipeline

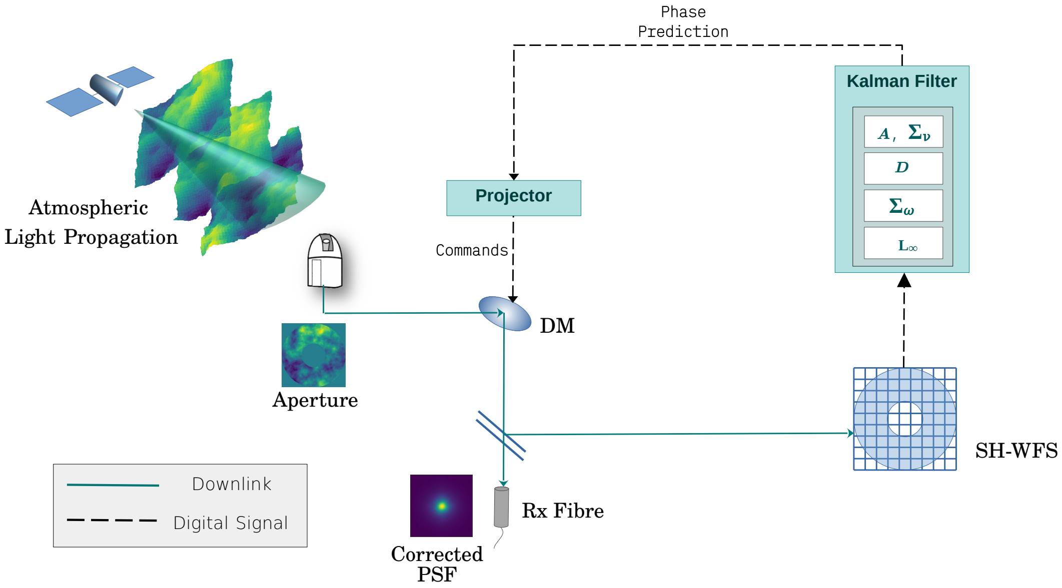

Figure 3.12: Illustration of the AO loop with the final LQG regulator simulation pipeline.

With the tools described in the sections above, it became practical to develop the simulation pipeline which was then used to obtain all the results herein described. This pipeline is illustrated in Figure 3.12. The light is virtually propagated through each atmospheric layer, and the resulting phase at each step masked with the aperture mask. The DM issues the correction phase computed on the previous iteration.

The resulting residual phase is both stored and fed to the WFS. The "Kalman Filter" module issues a state prediction from these measurements, and the phase is extracted and projected onto the DM. The time series is recorded into a csv file for ease of postprocessing.

3.3 Initial simulations: horizontal testbed link

With the goal of progressing towards including diffraction effects, a strong scintillation scenario was simulated. For this, the horizontal testbed link available at DLR was chosen. The horizontal testbed is a 10.5 km link between a valley and a mountain top in the Bavarian Alps with a 2° elevation. The link profile is depicted in Figure 3.13a).

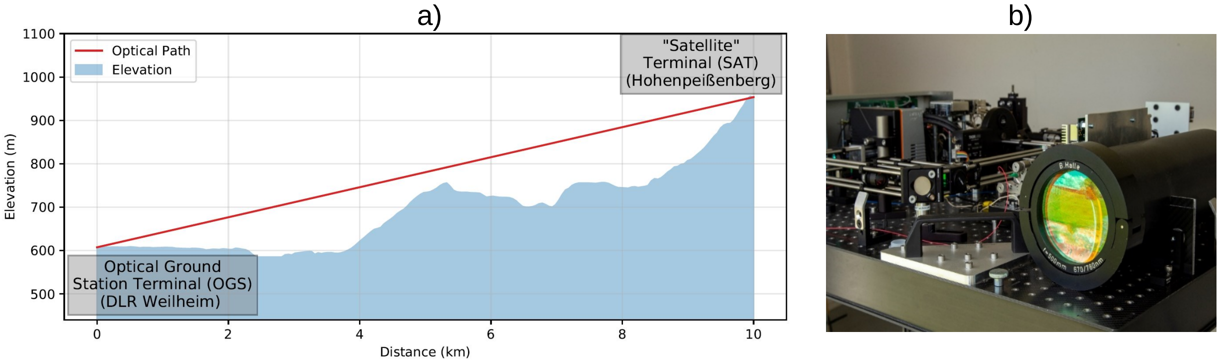

Figure 3.13: a) Elevation profile of the terrain across the 10km link; b) Optical ground station terminal from the testbed link showing the telescope on the optical bench.

This shows how the link is carried out through ground layer turbulence. The OGS is placed on the valley overlooking a mountain where another terminal is positioned, representing the satellite. When the testbed link first came to be, the hypothesis was that the low elevation angle together with the varying elevation profile along the path could create strong boiling turbulence and thus emulate the worst case scintillation present in satellite links. Several successful experiments carried out with the link meant availability of pre-existing on-sky data. Figure 3.14 shows r_0 estimation from fitting covariances to recorded SH-WFS data from a analysis carried out at the beginning of this thesis. On-sky data from the horizontal link provided an initial valuable reference for daytime conditions characterized by strong turbulence and low elevation angles.

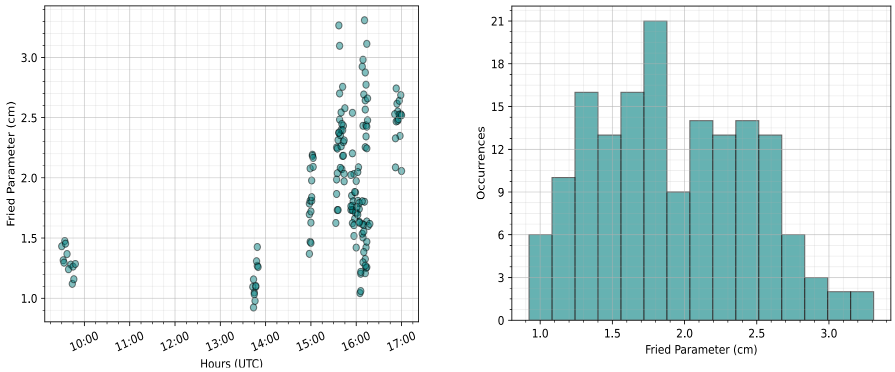

Figure 3.14: Histogram of recorded r_0 measurements (left); plot demonstrating the variation of r_0 with time (right),recorded over the course of different days. The site features relatively strong turbulence, with a mean measured r_0 through the day of $\approx$ 1.9 cm. There is great variation depending on weather conditions, and a trend of stronger turbulence observed in early afternoon (right).

The testbed features an OGS terminal bench with an AO system behind a 10 cm telescope (Figure 3.13b), and an 8 x 8 SH-WFS, producing n_y =104 measurements. The DM has 11 x 11 actuators with

97 active actuators and the system runs at an operating frequency of 2 kHz.The system parameters are summarised in Table 3.1.

Table 3.1: AO system parameters used in the end-to-end simulations. The physical AO system parameters match those of the Optical Ground Station of the THRUST Horizontal testbed link in Weilheim (KN-DLR).

Parameter	Value
Telescope aperture	$0.1\,\mathrm{m}$
DM	11 x 11 grid, 97 actuators
SH-WFS	8 x 8 subaperture grid, $n_y = 104$ total measurements
Rx Wavelength	1550 nm
AO loop rate $F_s = \frac{1}{T_s}$	$2\,\mathrm{kHz}$
Delay	2 frames (1 ms)

A simulation environment for the conditions experienced in the link was developed to test an LQG regulator and an integrator. Given the scintillation experienced, a boiling turbulence model was used, with 4 layers evenly spread out across the 10 km. Each layer was chosen to have a wind speed of 10 m/s, with opposing directions. The atmospheric profile for turbulence was chosen so that all 4 layers have the same relative strength. Based on the real SH-WFS data, some realistic parameters were chosen. As such, integrated r_0 of 2 cm was used, with an outer scale of one meter. This configuration of atmosphere was then used with the two different propagation algorithms: geometric and angular spectrum. The zonal-based LQG regulator with an oversampled (Figure 3.6) AR2 model generated from covariance priors (section 3.1.2.1) was compared against an integrator. The simulation was run for 5 seconds of data with both regulators tuned. The resulting probability density function plots for the coupling efficiency are shown in Figure 3.15, and the mean values for coupling efficiency, Strehl ratio and scintillation index are shown in Table 3.2.

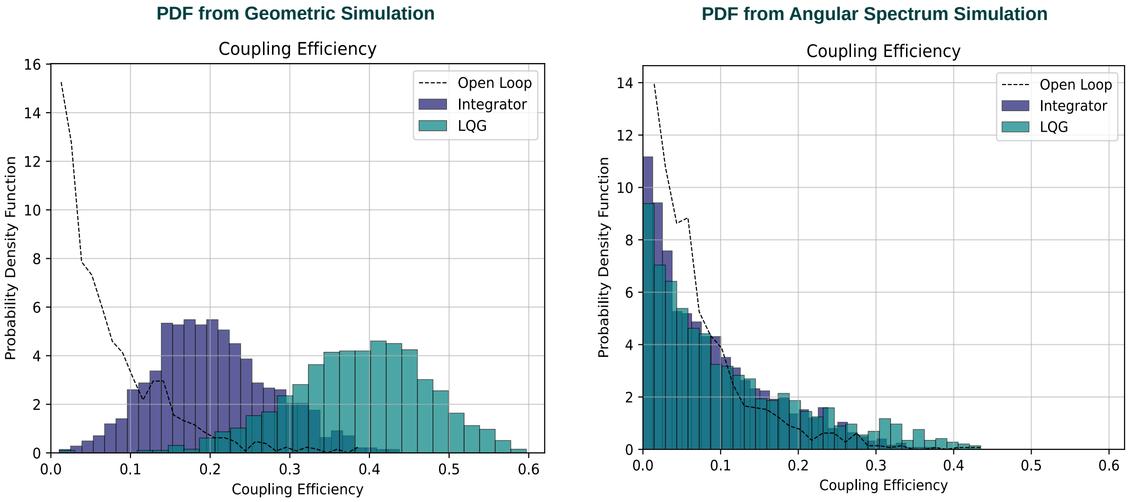

Figure 3.15: Simulation results across the horizontal link: probability density function for the coupling efficiency observed with an AO loop closed with an integrator and an LQG in both geometric (left) and angular spectrum (right) propagation methods.

These results show an overall improvement is obtained by deploying an LQG controller compared to an integrator. However, they also show a very significant difference in performance for the two propagation methods. In geometric propagation there is a significant improvement with LQG over the integrator, and both have been shown to be advantageous with regards to the open loop scenario. However, with the inclusion of diffraction effects into the simulation, the improvement obtained is rather marginal. It is also

Table 3.2: Simulation results across the horizontal link: mean values obtained for different performance parameters with geometric propagation (Geom.) and angular spectrum propagation (ASP).

Horizontal Link	**Coupling Efficiency (%)**		**Strehl Ratio (%)**		**Power Scintillation Index (PSI)**	
	Geom.	ASP	Geom.	ASP	Geom.	ASP
Integrator	20.43	8.90	21.33	8.16	0.13	0.84
LQG22	39.01	11.77	38.29	9.70	0.05	0.75

interesting to note that the Strehl ratio is on par with the coupling efficiency for both simulation scenarios. This effect is expected since the improvement of the image should lead to a better PSF and in turn better coupling of the light into the fibre core.

Table 3.2 shows that the scintillation index increased from 0.13 to 0.84 (integrator), and from 0.05 to 0.75 (LQG) with the inclusion of diffraction effects. Whilst the LQG regulator overperforms the integrator in both scenarios, the performance gap is very wide. Under the same exact conditions, the integrator drops coupling efficiency performance by 56.4% with the inclusion of scintillation, while the LQG controller drops by 69.8%. In the same table, the coupling efficiency improvement observed with the LQG over the integrator drops from 18.6 percentual points to only 2.8. The drop in performance follows the significant increase in scintillation index obtained for the ASP simulation conditions. This is further noted by the resulting long exposure normalized point spread function image and intensity profile for each of the propagation methods shown in Figure 3.16.

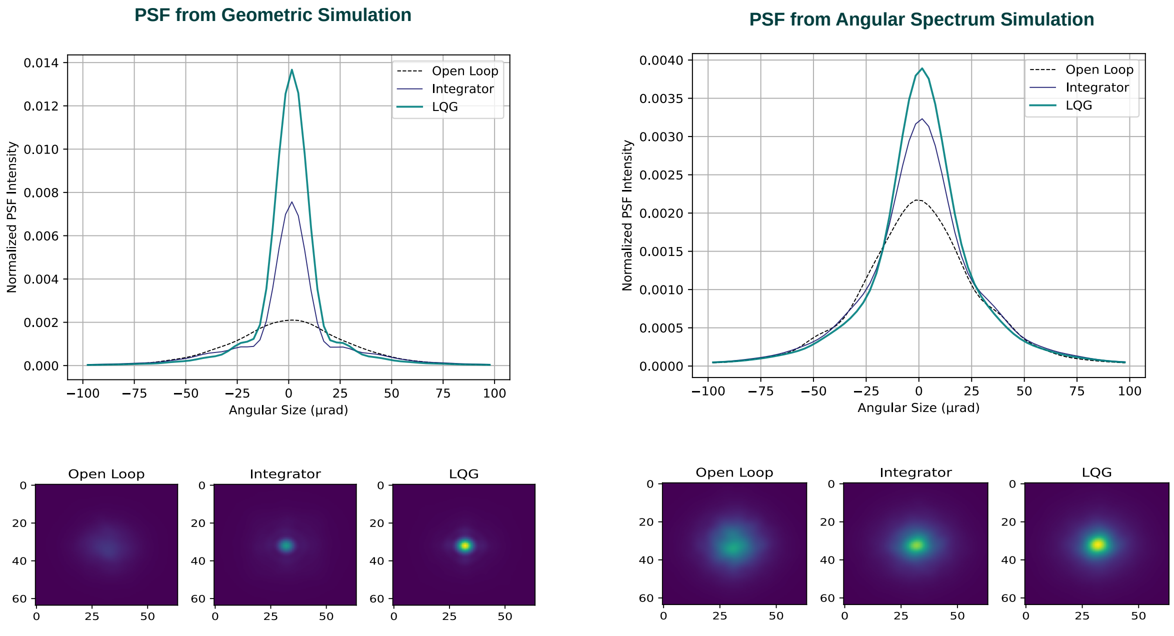

Figure 3.16: Simulation results across the horizontal link: long exposure normalized point spread functions for both controllers in each of the propagation methods.

The PSF intensity profile in the geometric case shows a clear improvement with the deployment of the LQG over the integrator, with the integrator still representing a great improvement over the open loop PSF. The image quality on their long exposure PSFs further supports this with a perfect Airy disk visible with the LQG in the geometric case. When looking at the diffraction-inclusive results however, the performance of both controllers drops significantly and this is visible in both the intensity profiles and the long exposure PSF images. The resulting image with ASP is significantly more blurry, suggesting a lot more lost light that does not end up reaching the fibre core with either of the regulators.

Overall, these results show that for FSOC scenarios where the light is expected to proapagate through strong scintillation, geometric propagation results can lead to overestimation in performance by misrepresenting its consequences on the WFS subapertures. In strong scintillation scenarios such as the one explored here, a simulation methodology that accounts for scintillation, and more particularly its effects on the flux variations on the WFS subapertures is therefore strongly recommended.

The following observations on these results and their conclusions should also be taken into account. First and foremost, the state-space model is not well representing of a boiling turbulence, as opposed to the dominating frozen flow turbulence expected in LEO links due to their rapid movement across the sky. Furthemore, this is done over a horizontal link. It is important to note that these are not necessarily representative of true satellite links. When it comes to optimising for the horizontal scenario, a different turbulence state-space model could be beneficial to the performance of the LQG regulator. For instance, given the availability of data, methods like subspace identification might prove to be more appropriate than the theoretical-based priors deployed here, which are ultimately based on frozen flow assumptions. However, in this thesis the goal is ultimately to optimise for LEO satellite links. Therefore, the horizontal link was left aside to explore LEO links in more depth. These results and optimisation are shown in the next chapter.

3.4 Summary

In this chapter, the methodology towards development and integration of LQG regulators within the existing end-to-end simulation is explained. The step-by-step approach towards LQG control implementation was shown, explaining the building blocks to obtain a full regulator with a Kalman filter. This initial implementation culminated with a cross-validation in which the simulation conditions and results reported in (Prengère et al. 2020) were replicated. With this validation completed, a summary of the software tools developed was shown. The resulting final simulation pipeline and controller tuning were explained. These newly developed tools were then used to simulate the FSOC-AO control with light propagation over a horizontal link. Two different propagation methods were considered in order to compare simulation with and without scintillation and assess its effects on the SH-WFS.

The horizontal link results illustrated that indeed the performance of regulators is much affected by the inclusion of scintillation into the simulation environment. In the case of the horizontal link, the coupling efficiency performance dropped by 56% with the integrator and by 70% with the LQG regulator. Therefore, reliable FSOC performance estimation under strong scintillation calls for simulation environments that include diffraction, as is the case of angular spectrum propagation. The detrimental effect of scintillation is further explored in the following chapters, particularly in Chapter 5.

Chapter 4

Zonal-based LQG regulators for FSOC-AO in downlinks with LEO satellites

The previous chapter detailed the work carried out to integrate and tests tools allowing to implement a variety of LQG controllers in the pre-existing simulation environment present in DLR. The simulation tools were initially used on the horizontal link. In this chapter, these simulation tools are used to assess performance of a zonal-based LQG regulator with theoretical priors in the context of LEO links. Model modifications are also proposed and tested in order to appreciate which modification should be used in this FSOC-AO context with scintillation and stronger turbulence.

4.1 Atmospheric conditions in LEO satellite downlinks

As mentioned previously in section 2.3.3, LEO links are dominated by frozen flow effects due to the apparent wind resulting from the fast motion of the satellite across the sky. The atmospheric profiles used here showcase this effect. These were developed for the project HydRON (High thRoughput Optical Network), an ESA project aiming towards global connectivity supported by optical feederlinks and are described in (Torre et al. 2024). Atmospheric turbulence was modeled using the Hufnagel–Valley 5/7 profile with turbulence strength at altitude h calculated as per Equation (2.12). This approach aims to ensure a realistic estimate of atmospheric dynamics encountered during typical LEO passes at 1000 km altitude. The profile was then discretized according to the equivalent layer method (Fusco et al. 1999) so that the integrated parameters are preserved. A visual representation of this is shown Figure 4.1.

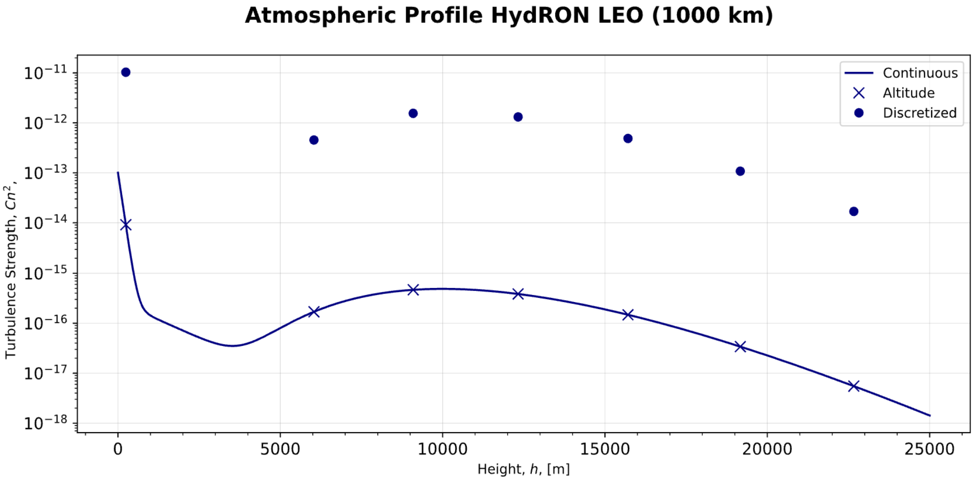
Atmospheric Profile HydRON LEO (1000 km)

Figure 4.1: Resulting turbulence strength profile corresponding to the HydRON LEO case, obtained from using the equivalent layer method (Fusco et al. 1999).

The turbulence profile is presented at zenith. However it is important to note that these profiles are not used directly at zenith. Instead, they are integrated and adjusted to the appropriate elevation angle corresponding to each of the presented SimID cases using the simulation tools. This ensures that the atmospheric effects are accurately represented for the specific slant path of each simulation.

Wind profiles were calculated for three different elevations according to the Greenwood model (Greenwood 1977). In order to do so, the wind ground velocity V_g was chosen to be 5 m/s and the wind tropopause velocity V_t was assumed to be 30 m/s (Torre et al. 2024). The windspeeds were obtained to include both natural and tracking winds. This was achieved by adjusting the calculated wind profiles according to equation (2.14) such that it would match empirical values of RMS wind speed w and ground-level turbulence coefficient T. The empirical values were taken to be $114.8\ \mathrm{m/s}$ and $1 \times 10^{-13}\ \mathrm{m}^{-2/3}$ respectively. These values correspond to the strong turbulence case for LEO satellite links at daytime (Torre et al. 2024). The wind direction relative to the telescope azimuth φ was kept 90° for all layers. A visual representation is shown here in Figure 4.2.

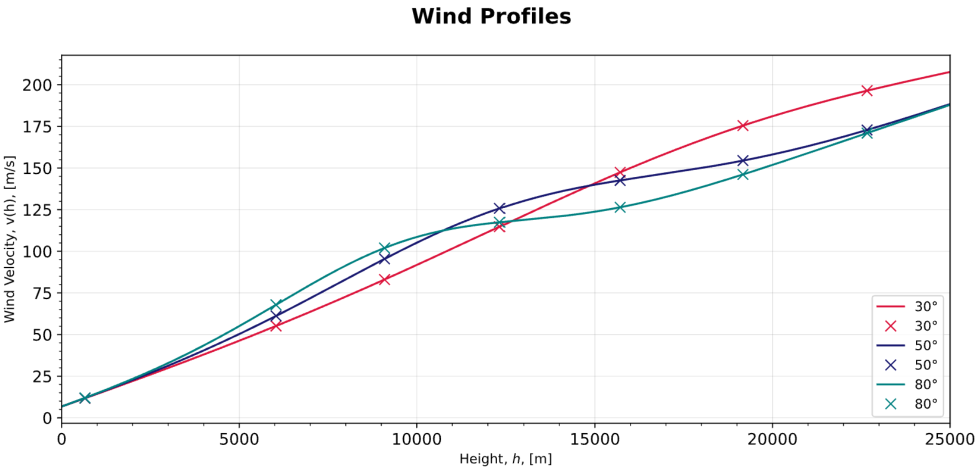

Figure 4.2: Resulting wind profiles corresponding to the HydRON LEO case, including both natural and apparent wind, obtained by adjusting calculations to match empirical values.

The final discretized turbulence profiles for each elevation angle and the corresponding wind speeds considered are summarised in table 4.1.

Table 4.1: Summary of the simulated turbulence conditions by atmospheric layer. The wind profiles consider the apparent wind dependence on satellite elevation to be a dominant effect, and thus all layers are assumed to have the same direction.

Altitude (m)	Cn^2dh **Profile** ($\mathrm{m}^{-1/3}$)	**SimID 80°** (m/s)	**SimID 50°** (m/s)	**SimID 30°** (m/s)
242	1.03×10^{-11}	8.08	8.04	7.99
6036	5.20×10^{-14}	68.0	61.39	55.21
9093	6.96×10^{-14}	100.75	95.18	83.17
12 325	5.67×10^{-14}	117.06	124.93	114.77
15 709	2.10×10^{-14}	126.89	142.32	147.16
19 168	4.63×10^{-15}	146.24	154.69	175.13
22 664	7.25×10^{-16}	170.95	173.00	196.25

The effective wind speed seen by the optical beam increases as the elevation angle decreases. This is coherent with the considered satellite orbit, in which as the elevation increases across a pass over the OGS-OP (section 4.2), the effective distance from the OGS to the satellite decreases, causing the slew rate to increase.

Table 4.2 summarises key atmospheric parameters for each of the simulation scenarios. The coherence time τ_0 represents the characteristic timescale over which the atmosphere remains correlated. The larger the value the slower the turbulence evolves. The isoplanatic angle θ_0 defines the angular distance over which atmospheric distortions remain similar. The larger the value, the more uniform the turbulence is over a wider field of view. The Fried parameter informs on the coherence length of the wavefront. A larger value

Table 4.2: Summary of atmospheric parameters for the different SimIDs, at both the standard wavelength of 500 nm for ease of comparison and the actual seeing wavelength of 1550 nm.

Atmospheric Parameters	τ_0 (ms)		θ_0 (μ rad)		r_0 (cm)		σ_R^2	
Wavelength (nm)	**500**	**1550**	**500**	**1550**	**500**	**1550**	**500**	**1550**
SimID 30°	0.3	1.2	1.91	7.42	1.08	4.19	2.22	0.59
SimID 50°	0.4	1.5	3.78	14.67	1.39	5.41	1.01	0.27
SimID 80°	0.5	1.7	5.64	21.93	1.94	7.54	0.64	0.17

translates to better seeing conditions. The Rytov variance σ_R^2 quantifies the strength of optical scintillation caused by turbulence. The higher the value, the stronger the turbulence resulting signal fluctuations. The parameters were computed both at the seeing wavelength of 1550 nm and at the usual standard of 500 nm for ease of comparison.

The parameters summarized in Table 4.2 indicate that a stronger turbulence is in consideration. These were calculated with the plane-wave consideration and are integrated along the propagation path. In particular, the Rytov variance σ_R^2 values suggest strong scintillation conditions consistent with those around 0.1-2 reported on-sky in (Beesley et al. 2025).

4.2 OGS-OP: Optical Ground Station at DLR, Oberpfaffenhofen

The simulations in this chapter feature the AO system parameters of the OGS-OP from DLR. This OGS is located on the roof of the Institute for Communication and Navigation and features a Cassegrain telescope with 0.8 m entrance pupil diameter and a 0.3 m obscuration (Figure 4.3). The telescope has a Coudé path to the optical lab. Its initial configuration comprised of an AO system with a SH-WFS of 13 x 13 subapertures and a DM with 16 x 16 actuators. This previous setup has been successfully deployed in links with Alphasat's TDP-1 (Technology Demonstrator Payload) in February/March and April/May of 2023 as part of the PREDATOR project at DLR (Hristovski 2025).

Figure 4.3: OGS-OP Cassegrain telescope with the mirror covers and dome open. This telescope has a pupil diameter of 0.8 m and a central obscuration with 0.3 m.

The OGS-OP is currently undergoing an AO system upgrade needed for several upcoming projects. Therefore the simulations here shown feature the upgraded AO system. This includes a 29 x 29 SH-WFS with 544 valid subapertures resulting in 1088 total measurements, as well as a 32 x 32 DM with 812 active actuators. The full AO system and simulation parameters are summarized further in Table 4.4, in section 4.4.1 dedicated to end-to-end simulation parameters.

4.3 LQG regulator synthesis

In this section, three different LQG architectures are considered. All are built from zonal-based models developed from theoretically calculated covariances as explained in section 3.1.2.1. All use the measurement noise covariance matrix method described in section 3.1.2.2. The WFS matrix was calculated according to what was explained in section 3.1.2.3. Each LQG controller is based on a different state representation and therefore uses a different WFS matrix according to the chosen phase grid.

4.3.1 Oversampling and edge mitigation

As has been detailed before in section 3.1.2.3, Fried geometry is followed. As mentioned in section 4.2, the telescope features a fairly large central obscuration amounting to about one-third of the pupil diameter. The baseline choice for zonal AO control is to sample the wavefronts at the location of each actuator and making sure to include the central obscuration. The reason for this inclusion of the obscured centre is to preserve the spatio-temporal structure in the predictions so as not to loose that information which is particularly relevant in frozen flow. This regulator will be identified as **LQG1**.

It has been shown that oversampling the phase by a linear factor of two as is shown in Figure 3.6b) could significantly improve AO performance (Prengère et al. 2020). It is also possible to extend the prediction zonal grid beyond the pupil's edges. The oversampling is explained and illustrated in section 3.1.2.3. The extension of the pupil is illustrated in Figure 4.4. Extending the prediction grid allows the Kalman filter to account for correlations between partially observed regions and is expected to improve prediction quality in the absence or deterioration of data near the obscured zone. Incorporating both edge and obscuration effects ensures consistent support for the spatio-temporal structure of the disturbance, which is critical for accurate phase estimation. For ease of distinction of regulators, the oversampled regulator will be referred to as **LQG2**, and the one contemplating both the oversampling and pupil extension is reported as **LQG22**. This numenclature is summarized in Table 4.3 together with the total number of grid points.

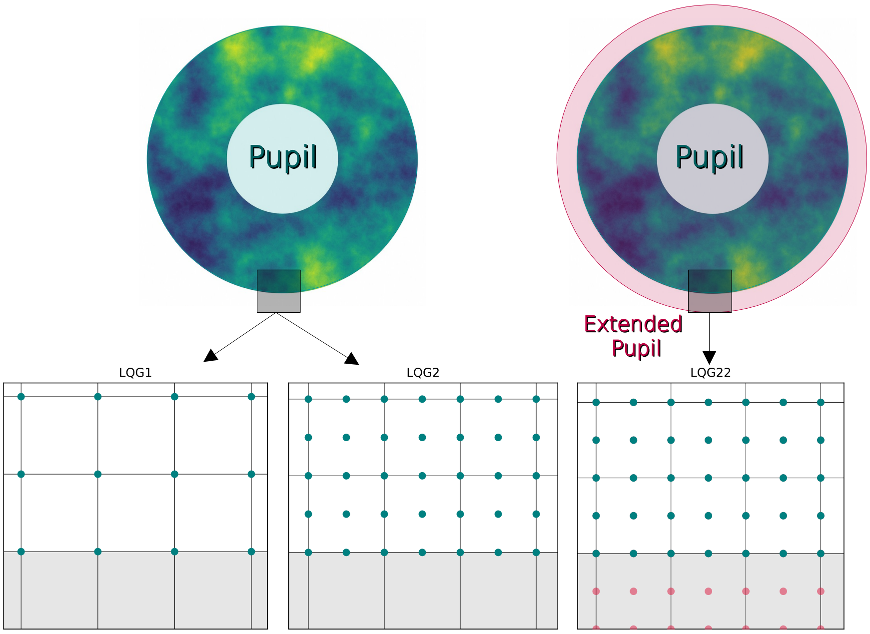

Figure 4.4: Zoom in of the phase sampling grid for each regulator superimposed to the WFS grid. White squares represent valid WFS subapertures, whilst gray ones are outside the pupil and unilluminated. Regulator LQG1 uses a phase sampling grid which corresponds to the actuator grid in a Fried configuration (actuators at the edges of the subapertures); Regulator LQG2 uses an oversampled phase points grid by a factor of 2; Regulator LQG22 is also based on a phase points grid oversampled by a factor of 2, but additionally extends phase points to an extra ring of subapertures outside the pupil.

Table 4.3: Summary of LQG regulators tested in the SimID 30° scenario, comprising a mix of simplified grid, oversampling, and edge extension, defined as the number of extra subapertures across the diameter. Central obscuration is included for all regulators.

Regulator	Oversampling	Edge	Total grid points
LQG1	1×	0	720
LQG2	2×	0	2889
LQG22	2×	2	3269

4.4 End-to-end simulations

4.4.1 Simulation parameters

Table 4.4: AO system parameters used in the end-to-end simulations. The physical AO system parameters match those of the Optical Ground Station of Oberpfaffenhofen (OGS-OP) at the Institute for Communication and Navigation (KN-DLR), detailed in section 4.2.

Parameter	Value
Telescope aperture	$0.8\,\mathrm{m}$
Central obscuration	$0.3\,\mathrm{m}$
DM	32x32 grid, 812 actuators
Shack-Hartmann WFS	29x29 subaperture grid, 1088 total measurements
Rx Wavelength	1550 nm
AO loop rate $F_s = \frac{1}{T_s}$	$2\,\mathrm{kHz}$
Delay	2 frames (1 ms)
Run duration	5 s (10,000 iterations with first 50 discarded in analysis)
Runs per case	3, different random seeds
Total duration	$15\,\mathrm{s}$ per case

In order to assess which modification brings the most benefit, the LQG architectures previously detailed are synthesized and simulated, with features summarized in Table 4.3. These regulators are then evaluated at three elevation angles (30°, 50°, and 80°), corresponding to the turbulence conditions described in Table 4.1. In each presented analysis, the regulators are compared to a tuned integrator as a benchmark. The integrator tuning is carried out with the goal of finding the optimal performance point by testing different combinations of the truncation of the SVD conditioning of the command matrix and the gain. The LQG regulators use the true priors in each case, unless explicitly stated otherwise. Moreover, all are best tuned as explained in section 3.2.3. Tuning the fudge factor enables the LQG regulator to recover a quasi-optimal performance and good robustness margins despite model mismatch and non-linearities. Table 4.4 summarizes the optical and hardware configuration and the simulation methodology used across presented results. The parameters match those of the OGS-OP AO system at DLR (section 4.2). The following sections detail the simulations and respective results.

4.4.2 LQG performance on low elevation LEO profile

In order to assess the performance of the LQG regulator structure, among LQG1, LQG2 and LQG22, that gives the best results for the reported conditions, SimID 30° was chosen as it represents the worst elevation case in consideration within the scope of this study. The priors models were built with covariances matching the parameters in SimID 30°. The tuned LQG controllers were evaluated against a tuned integrator as a performance benchmark. The performance of all regulators simulated for this scenario is summarised in Figure 4.5 for coupling loss comparisons and Table 4.5 for fade statistics analysis.

Overall, it is clear these LQG regulators ensure better performance when compared with a tuned integrator. The normalized distribution as well as the cumulative probability functions (Figure 4.5) show a clear visual distinction between integrator and LQG regulators, and more notably between LQG1 and LQG2 or

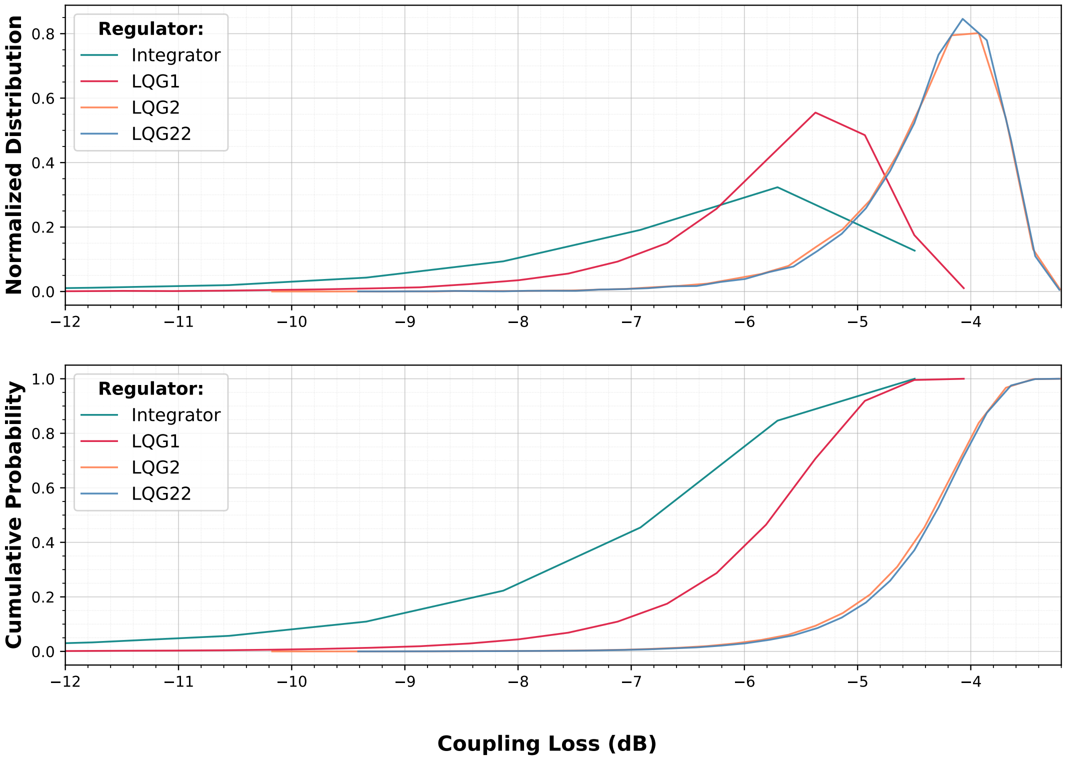

Figure 4.5: Normalized histogram (top) and cumulative probability (bottom) comparison between the integrator and the different simulated LQG regulators for SimID 30°. Each regulator was tuned to their best performance for the considered SimID case.

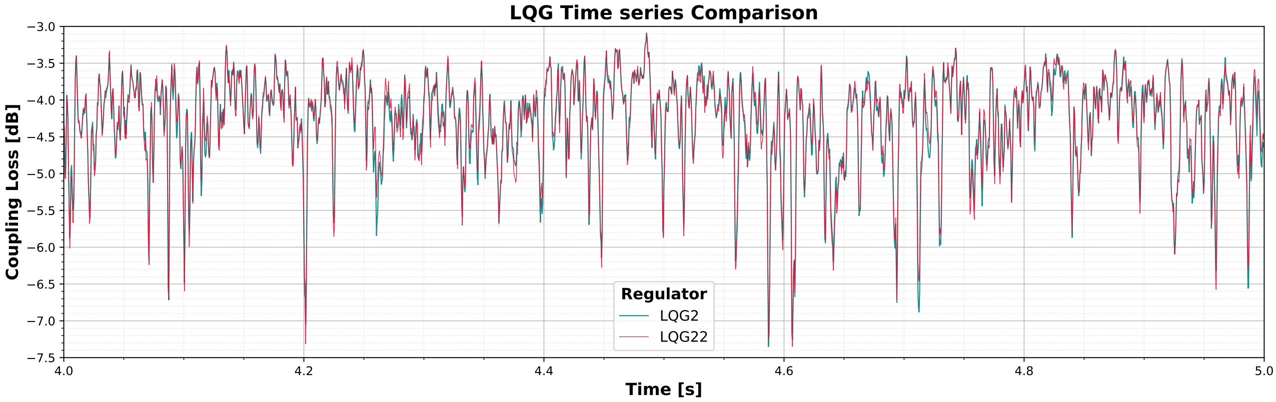

Figure 4.6: Time series comparison of LQG2 and LQG22 during 1 second in steady state performance.

LQG22. Moreover, an oversampled model for the LQG (LQG2) brings a mean improvement of 1.38 ± 0.02 dB over the non-oversampled LQG1, and a reduction of 85 % on the -3 dB fade events quantified in Table 4.5. LQG22, implementing both the oversampling and edge mitigation techniques, shows a marginal improvement over the LQG2 when it comes to mean and median coupling loss, and although the fade count is not improved, the fade duration is lowered by 0.1 ms. In Figure 4.6 the time series for both LQG2 and LQG22 are shown. This plot emphasises how similar the closed-loop responses between the two regulators are. However, it also shows that the small performance improvement observed previously in Figure 4.5 seems to come from the fact that the depth of loss during fade events is sometimes mitigated by LQG22 with regards to LQG2. This supports the use of LQG22 as the best regulator architecture, with use of a theoretical covariance calculation based on zonal priors. Therefore, the following sections use LQG22 regulator for comparison with the integrator.

Table 4.5: Performance summary for SimID 30°for all simulated regulators, resulting standard error of the mean SE±0.01 dB. Coupling loss mean and median, as well as fade statistics at thresholds of $-3\,\mathrm{dB}$, $-6\,\mathrm{dB}$, and $-10\,\mathrm{dB}$ with fade count per second (F/s) and mean fade duration (ms).

SimID 30°	**Coupling Loss (dB)**		**−3 dB**		**−6 dB**		**−10 dB**	
	Mean	**Med.**	**F/s**	**ms**	**F/s**	**ms**	**F/s**	**ms**
Integrator	-6.65	-6.15	42	1.86	15	1.33	4	1.08
LQG1	-5.75	-5.52	20	0.95	2	0.78	<1	0.50
LQG2	-4.37	-4.23	3	1.12	0	−−	0	-
LQG22	-4.35	-4.21	3	1.02	0	−−	0	-

4.4.3 LQG22 results at different elevations

In this section, the winning LQG22 architecture of previous sections is thus simulated with the remaining elevation scenarios. For each scenario, the corresponding priors were taken, built with zonal-based theoretical covariances from von Kármán statistics as explained in section 2.1.1. The resulting regulator was simulated with its corresponding atmosphere, according to the same parameters reported previously in tables 4.1 and 4.4. The resulting coupling loss time series for each of these is shown in Figure 4.7.

Table 4.6: Coupling loss and fading statistics for LQG22 on SimID 80° (SE±0.01 dB).

SimID 80°	**Coupling Loss (dB)**		**−3 dB**		**−6 dB**		**−10 dB**	
	Mean	**Med.**	**F/s**	**ms**	**F/s**	**ms**	**F/s**	**ms**
Integrator	-4.80	-4.64	3	1.76	< 1	1.00	0	-
LQG22	-3.17	-3.12	0	-	0	-	0	-

The LQG performance is best for the highest elevation corresponding to SimID 80°. With LQG, coupling loss decreases by 1.63 dB (from 33.1 % to 48.2 % efficiency), corresponding to a 45.5 % relative increase in coupled power. Furthermore, it is clear that the deeper fade statistics summarized on Table 4.6 improve drastically when compared to the case of SimID 30° from the previous section. This is indeed expected as the turbulence conditions for the higher elevation case, and specifically the scintillation, are more favourable towards the AO performance. The elevation is the closest to zenith, leading to best resulting integrated parameters, as is summarized on Table 4.2. Thus, the lower scintillation leads to lesser drastic power drops such as those counted as -6 dB and -10 dB.

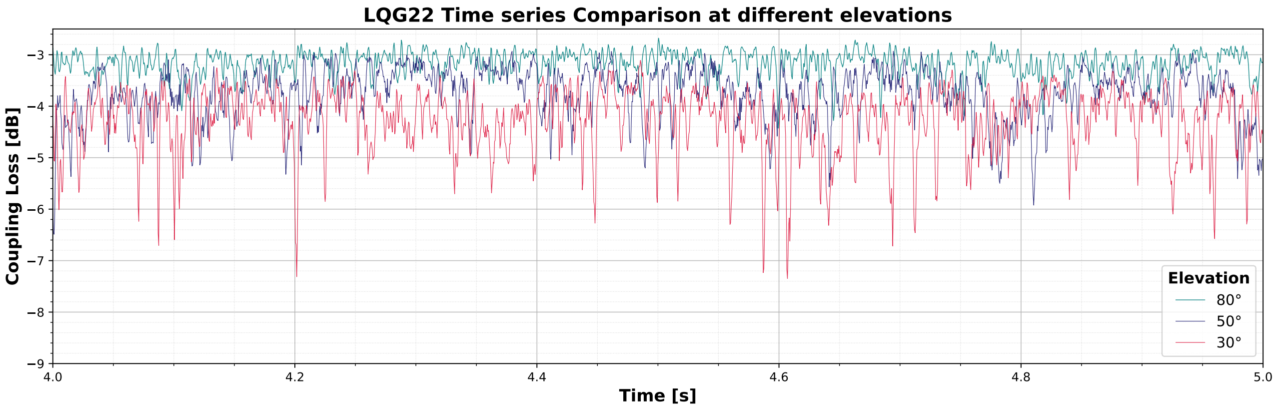

Figure 4.7: Time series for the LQG22 with the same phase screens performing at different elevations during 1 second in steady state performance.

The mean coupling performance for the atmospheric conditions corresponding to SimID 50° is decreased by about 0.79 dB with respect to the SimID 80° case. Moreover, the steady state sees more oscillation with time as is visible in the time series plot (Figure 4.7). Notably, when making the same comparison between elevations for the integrator, the loss is higher, at about 0.89 dB when compared to the integrator at 80°.

When focusing solely on the performance at 50°, coupling with LQG is improved by 1.73 dB (from 26.9 % to 40.2 % efficiency) with regards to the integrator, corresponding to a 48.9 % relative increase in coupled power. Table 4.7 summarises the fade statistics. A reduction of 68 % of the -3 dB fades with regards to the integrator is shown. The deeper fades have increased with regards the SimID 80° case. This is once again on par with the turbulence conditions worsening as the elevation is lowered (section 4.1). As the scintillation increases, so do the fade events and their duration, and more events on the deeper fade levels are reported due to more significant power drops with regards to mean loss.

Table 4.7: Coupling loss and fading statistics for LQG22 on SimID 50°, with SE±0.02dB.

SimID 50°	Coupling Loss (dB)		−3 dB		−6 dB		−10 dB	
	Mean	Med.	F/s	ms	F/s	ms	F/s	ms
Integrator	-5.69	-5.42	19	2.35	3	1.84	< 1	1.88
LQG22	-3.96	-3.73	6	2.39	< 1	0.63	0	-

Tables 4.7 and 4.6 together with Figure 4.8 show that LQG22 consistently outperforms the integrator in both coupling efficiency and fading statistics. The improvement in median coupling loss is within 31-33 %. The curves on Figure 4.8 represent the coupling loss distributions (histogram, top) and the corresponding cumulative probabilities (bottom). As expected, the distributions flatten with decreased elevation.

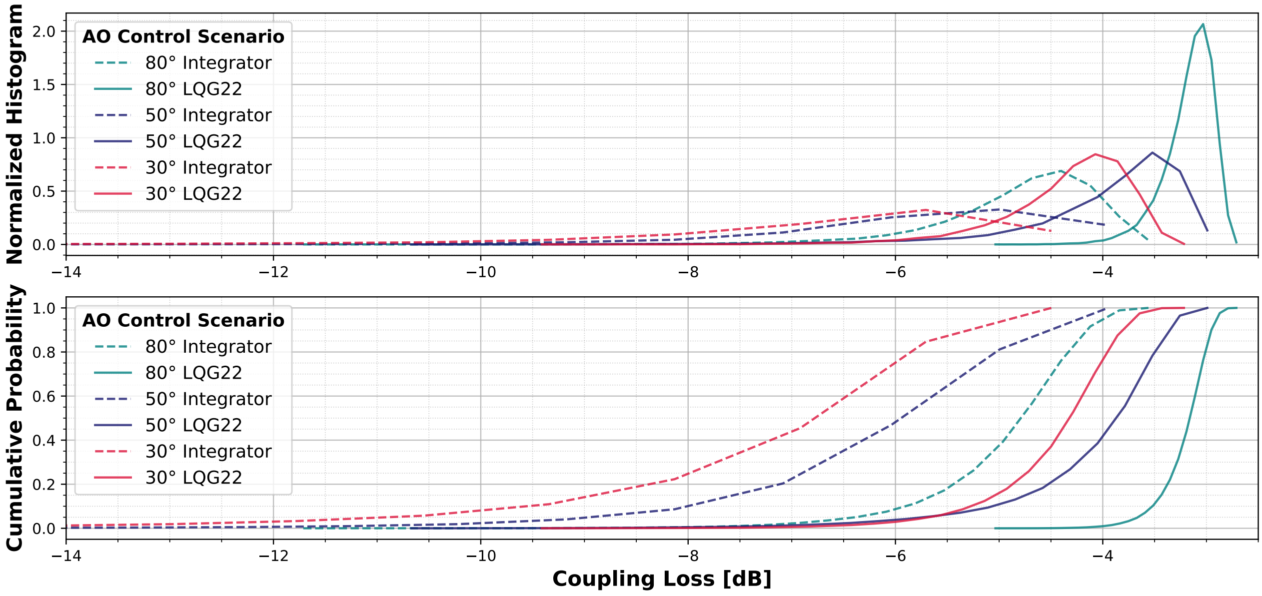

Figure 4.8: Normalized histogram (top) and cumulative probability (bottom) comparison of LQG22 with the integrator (benchmark) at the different simulated elevations.

As is also notable from the normalized histogram and cumulative probability plots, the LQG22 improves performance with elevation, following the same trend as a tuned integrator. These results are consistent with what was expected, as the diffraction-induced scintillation on the sensor is most critical at low elevations. Of note in figure 4.8 is the fact that even an integrator in its most favourable scenario (SimID 80°) under performs when compared to the LQG22 in its least favourable scenario (SimID 30°). This fact already positions the LQG regulator as a serious alternative to the integrator for LEO links.

All the simulation results so far test all the regulators at their best, i.e. model matched and tuned. In reality, especially considering a 15 min link spanning across low to higher elevation and back to low, the chosen LQG will hardly be model matched. The following section explores the robustness of the LQG to model mismatch by deploying the same LQG with the same priors to all the different operating conditions considered so far.

4.4.4 Performance robustness to elevation

In order to assess performance robustness of LQG regulators designed with turbulence profiles calculated for the wrong elevation, an LQG22 regulator synthesized with priors corresponding to the SimID 30° case was chosen and deployed at all elevations. The following results for SimID 50° and SimID 80° were thus obtained with erroneous priors corresponding to a 30° of elevation.

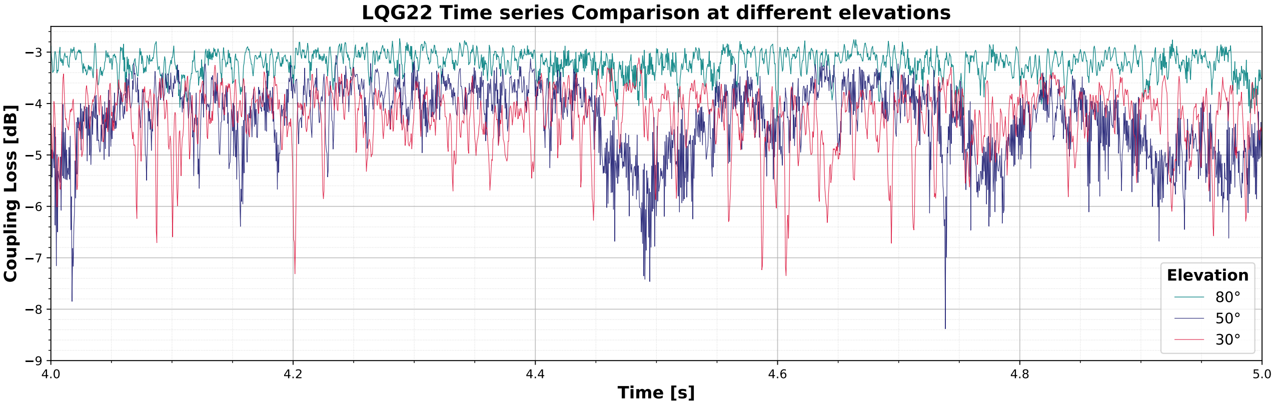

Figure 4.9: Time series for the LQG22 with priors from SimID30° only, with the same phase screens performing at different elevations during 1 second in steady state performance.

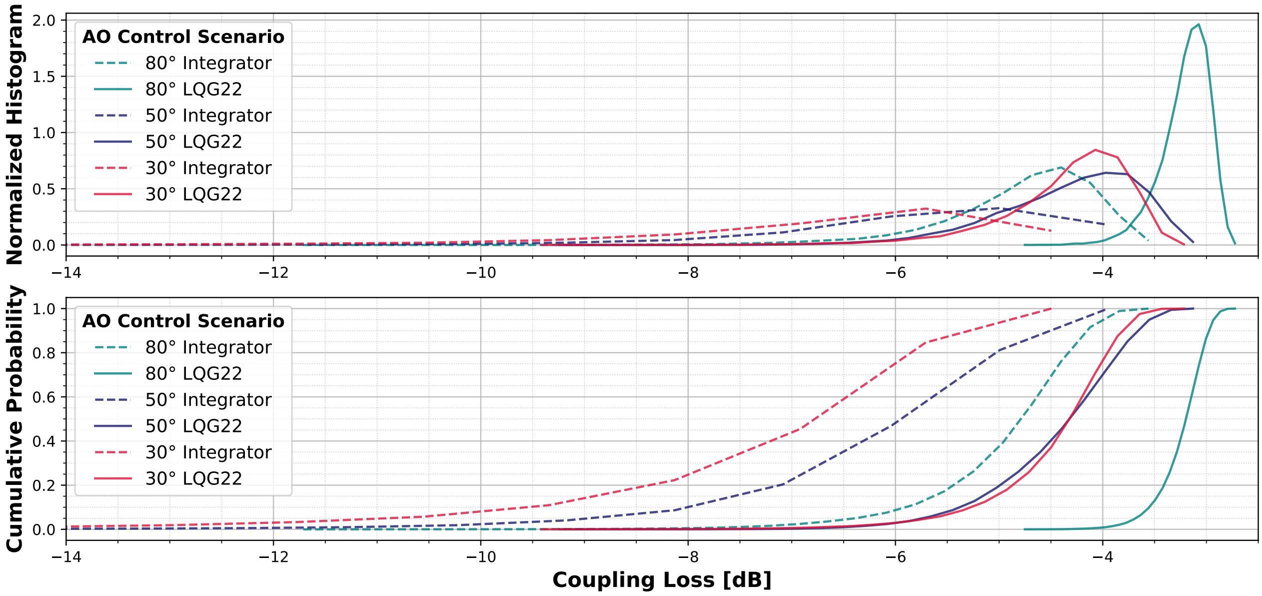

Figure 4.10: Normalized histogram (top) and cumulative probability (bottom) comparison of integrator and LQG22 keeping priors for SimID 30° but simulated at different elevations (SimID 50° and SimID 80°).

Figure 4.9 represents the time series for 1 second of data with the LQG regulator for SimID 30° deployed also for elevations corresponding to 50° and 80°. The performance for the 80° elevation case is with this imposed mismatch quite similar to the one reported in the previous section where the LQG regulator used the true priors. However the performance for 50° is visibly degraded when compared to the optimal cases represented in Figure 4.7 with its performance occasionally dropping below that of the 30°. While apparently odd, this could be attributed to the variations in the wind profiles when looking at their shapes in Table 4.1. The 4th layer, corresponding to an altitude of 12325 m is modeled with a wind velocity higher for the SimID 50° than the other two scenarios. Therefore, using the priors for SimID 30° at the elevation of 50° will result in a different overall covariance ratio, as the overall shape of the wind profile is different. Additionally, more oscillation and steady-state fluctuations are observed, and can be attributed to the imposed model mismatch.

The curves on Figure 4.10 further illustrate the aforementioned performance description, with a degradation most accentuated at 50° with regards to the optimal controller for each case shown in Figure 4.8.

Nevertheless these results highlight that LQG22 regulator outperforms the integrator, even when deployed on a scenario for which a model mismatch is imposed. This robustness to modeling errors further establishes the LQG regulator as compelling alternative to integrator control in FSOC-AO for LEO links.

Table 4.8: Coupling loss and fading statistics for LQG22 with priors from SimID30°, evaluated on SimID80° and SimID50°.

LQG22 with 30° priors	Coupling Loss (dB)		−3 dB		−6 dB		−10 dB	
	Mean	Med.	F/s	ms	F/s	ms	F/s	ms
SimID 80°	-3.20	-3.16	0	–	0	–	0	–
SimID 50°	-4.33	-4.21	2	0.58	0	–	0	–

Table 4.8 summarizes the coupling loss statistics for these simulations. The median coupling loss for SimID 80° shows a negligible loss (0.04 dB) when comparing the results to the case of LQG22 controller built with the matched priors. Furthermore, there is no change to report in the fade statistics. However, when it comes to SimID 50° a more accentuated loss of about 0.5 dB is reported. When simply comparing the fade values of Table 4.8 directly with 4.7, one could be led to the interpretation that the fade statistics improved. However, it is important to note that this drop is relative to the mean coupling loss. So in the case of LQG22 for SimID 50° with true priors the total loss drops below -6.96 dB on average 6 times per second for a duration of 2.39 milliseconds, for the LQG22 controller with 30° priors the -3 dB loss level is actually -7.33 dB. Therefore, in this case the LQG22 regulator drops on average 2 times per second for a duration of 0.58 milliseconds below -7.33 dB. However, it should be noted that even at the worst model mismatch, coupling loss is still improved by 1.21 dB, which represents an improvement of 32.1 % relative to the tuned integrator on the same conditions. This robustness is particularly attractive for FSOC-AO and a major improvement with regards to the integrator which does not provide added stability without significant performance trade-offs such as increasing the SVD truncation, lowering the gain or adding a leak.

4.5 Estimation of impact on the communication channel

Previously in section 4.4 the performance improvement that is possible with an LQG regulator with regards to an integrator control for FSOC-AO was shown and emphasized under different scenarios. Whilst the first performance goal is to minimize the coupling loss and fade events, it is interesting to get an idea of how this can tie back to channel modeling and improve the communication channel. The following sections present initial estimation approaches taken with the aim of quantifying this subject.

4.5.1 BER (bit-error-rate) estimation

Coupling loss and fade statistics reflect over the quality of the physical optical channel. Throughout the manuscript a high signal-to-noise (SNR) ratio is assumed. This assumption is often taken when dealing with FSOC systems due to the use of narrow beam divergences, high transmit powers, and sensitive receivers (Stotts et al. 2008). In order to assess how the regulator performance would translate into coding performance, a first approach to a Bit Error Rate (BER) estimation was calculated against the SNR range. The goal is to provide an estimation of the performance difference between LQG and integrator control under strong turbulence from the channel coding perspective. As such, Gray-coded Dual-Polarization Quadrature Phase-Shift Keying (DP-QPSK) modulation with coherent detection was assumed, as is one of the standards mentioned in ESTOL (European Space Agency 2023). Assuming a standard bit-wise Additive White Gaussian Noise (AWGN) model (i.e., identical and independent Gaussian noise per bit), the BER per bit can be obtained in the same manner as if binary phase-shift is used (BPSK) (Proakis 2001). Therefore the BER calculation for BPSK can be assumed to be as follows (Stotts et al. 2008)

$$\mathrm{BER} = \frac{1}{2}\,\mathrm{erfc}\left(\sqrt{2\,\mathrm{SNR}}\right) \tag{4.1}$$

where $\mathrm{erfc}(\cdot)$ denotes the complementary error function, SNR is the signal-to-noise ratio per bit, and BER is the resulting bit error rate computed under the assumption of an AWGN channel model. In order to account for the impact of the fading statistics on the curve, the fade levels were mapped to power penalties in SNR (for instance, -3 dB fades correspond to 50 % power loss)

$$\mathrm{BER}_{\mathrm{total}} = t_{\mathrm{mean}}\,\mathrm{BER}_{\mathrm{mean}} + t_{3\,\mathrm{dB}}\,\mathrm{BER}_{3\,\mathrm{dB}} + t_{6\,\mathrm{dB}}\,\mathrm{BER}_{6\,\mathrm{dB}} + t_{10\,\mathrm{dB}}\,\mathrm{BER}_{10\,\mathrm{dB}} \tag{4.2}$$

where t_{mean}, $t_{3\,\mathrm{dB}}$, $t_{6\,\mathrm{dB}}$, and $t_{10\,\mathrm{dB}}$ denote the fractional time spent under nominal conditions and during -3 dB, -6 dB, and -10 dB fading events, respectively, while $\mathrm{BER}_{\mathrm{mean}}$, $\mathrm{BER}_{3\,\mathrm{dB}}$, $\mathrm{BER}_{6\,\mathrm{dB}}$, and $\mathrm{BER}_{10\,\mathrm{dB}}$ represent the corresponding bit error rates for each condition. The total bit error rate $\mathrm{BER}_{\mathrm{total}}$ is therefore obtained as the time-weighted sum of the individual contributions. It is important to note this constitutes a very simplified approach to what is a very complex and circular problem subject to its own contemporary research, as is evidenced by Stotts *et al* in (Stotts et al. 2025).

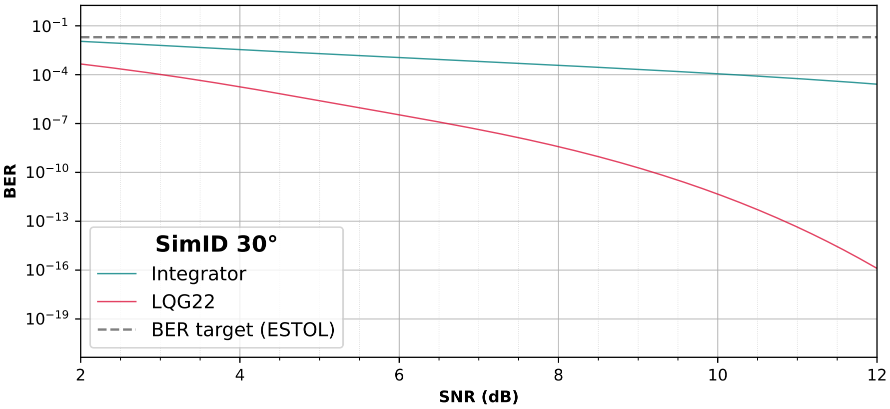

Figure 4.11: Plot capturing BER estimation versus SNR for integrator and LQG, with the BER target from ESTOL (European Space Agency 2023) shown for reference.

The resulting BER performance for both regulators under varying low-SNR conditions is plotted in Figure 4.11. The dotted line shows the ESA Specification for Terabit/sec Optical Links (ESTOL) threshold for DP-QPSK, pre-FEC BER of $2\mathrm{x}10^{-2}$ and is included as a reference value considered for the minimum value that enables LEO links. Both regulators meet this target. According to the plot, the LQG22 brings a significant improvement in estimated BER regardless of the SNR. However this effect is even more noticeable when accounting for high SNRs, where the FSOC range tends to be. For instance an SNR of 10 dB, the LQG22 regulator achieves a bit error rate of approximately 10^{-11}, compared to 10^{-4} for the integrator. Furthermore, BER is assumed to be quasi-error free when it is below than $10-9$ (European Space Agency 2023). The lower BER reduces the reliance on post-processing techniques such as forward error correction (FEC) or retransmission schemes, thereby improving the effective data throughput (Proakis 2001). Therefore, considering for instance an LQG regulator operating at an SNR of 10 dB, the BER can be considered quasi-error free before FEC, thus minimizing the need for post-processing.

It is important to caveat this observation with reiterating that BER estimation is indeed a complicated subject, and a direct comparison is difficult. Furthermore, deploying an optimal control algorithm such as LQG22 could represent an improvement in the channel and SNR, and thus change the set point of the curve with regards to the integrator which would remain at a potentially lower SNR. An improvement in the channel quality and SNR could enable different choices for the modulation, or even enable different other choices in terms of link budget calculations and hardware. This analysis is intended as a preliminary estimation to provide an overall sense of the achievable performance gains. This should be further explored to refine the relationship between control performance and BER.

4.5.2 Assessing potential impact on quantum communication

Quantum communication is an advanced technology expected to be fundamental to achieving secure satellite communications. This is in particular attributed to quantum key distribution (QKD), a method aiming to securely generate and share encryption keys by leveraging the laws of quantum physics. In QKD, information is encoded onto individual photons. The quantum properties of photons, such as polarization, are used to transmit key bits. Any attempt to intercept/measure photons disturbs their state, allowing the communicating parties to detect potential eavesdropping and ensure the security of the shared key.

Whilst quantum communication is a topic beyond the focus of this thesis, collaboration with DLR researchers responsible for the QKD study detailed in (Häusler et al. 2023) enabled performance assessment in terms of quantum bit-error-rate (QBER) and the secret key rate (SKR) metrics for a given link budget corresponding to FSOC with LEO satellites. Based on this study it is possible to evaluate how the LQG regulator could affect performance with respect to the integrator based on the mean coupling loss.

For this study, a BB84 protocol was taken as a the standard choice.The QBER measures the fraction of bits that are different between the shared keys in order to quantify the error rate in the quantum channel. It is given by a ratio between the number of erroneous bits and the total bits received and can be written as:

$$QBER = \frac{n_{\text{wrong}}}{n_{\text{right}} + n_{\text{wrong}}} \tag{4.3}$$

where n represents the bit count. The QBER does not account for any sort of post-processing and is used to estimate how much information might have leaked to an eavesdropper. Therefore a low QBER indicates high quantum channel quality. The SKR represents the rate at which the secure and usable key bits are generated and can be obtained with the calculated QBER, according to the explanation given on the appendix A of the publication from Häusler et al (Häusler et al. 2023). The SKR counts the number of truly secret bits per second that remain after processing (correcting errors, removal of bits that might be partially known to an eavesdropper). The SKR depends directly on the QBER and channel loss, as well as detector and post-processing efficiency. A higher SKR indicates better channel quality.

Here an estimate of both the QBER and SKR from link budget parameters is presented. In order to do so, the OGS-OP was considered (configuration parameters found in Table 4.4). Considering the coupling loss results detailed in section 4.4.2 it was possible to take a first step estimation of QBER and SKR for all simulated regulators at SimID 30°. The results obtained from the simulation methodology detailed in (Häusler et al. 2023) are presented in the Table 4.9.

Table 4.9: QBER and SKR performance comparison between LQG and integrator controllers, obtained with the simulation and methodology described in (Häusler et al. 2023).

SimID 30°	QBER (%)	SKR (kbit/s)
Integrator	0.793	24.84
LQG1	0.787	30.59
LQG2	0.779	42.07
LQG22	0.779	42.26

The results show a slight decrease in QBER and a significantly higher SKR with the LQG regulators compared to the integrator. Even small reductions in error probability can yield large increases in usable key rate, and this is demonstrated in the results above. This is due to the non-linear relationship between QBER and SKR. As a result, an increase in QBER leads to an amount of information that must be corrected/discarded much higher than linearly expected. Therefore, the small improvement in QBER increases the corresponding SKR by 23% with LQG1 compared to the integrator with the key rate jumping from 24.84 kbit/s to 30.59 kbit/s. The best regulator LQG22 increases the key rate to 42.26 kbit/s, corresponding to 70% improvement with regards to the integrator. The QBER and SKR values are consistent with those reported in (Häusler et al. 2023), and thus provide a valid indication of the expected impact of improved link stability on secure key generation.

This analysis constitutes a first step into QKD performance assessment when deploying AO system on the OGS with an LQG regulator instead of an integrator. These results showcase a substantial improvement in performance for QKD and provide a very compelling justification for adopting LQG control in place of conventional integral action control when it comes to FSOC-AO. This should be further investigated.

4.6 Summary

In this chapter, simulation results with LQG regulators in LEO link scenarios were presented and compared with best-tuned integrator for an AO system corresponding to the one at the OGS-OP (KN-DLR). It was shown that an oversampling of phase points by a factor of 2 leads to a performance improvement of 34.5 % with regards to an LQG regulator built from a simplified Fried geometry phase grid. Moreover, it was shown that an extension of the phase grid to outside the edge of the pupil brings only a marginal improvement when compared to what is reported in (Prengère et al. 2020). Several differences between results should however be noted. Both simulate different AO systems and different turbulence conditions, being that both the apparent wind and turbulence profile chosen here represent more severe conditions. The AO system contemplated in the paper had a pupil diameter of 1.8 m, with a central obscuration of 20 cm, a system that is recovering more light. It is also a smaller AO system resulting in lower spatial resolution, which might explain why it sees more benefits. Moreover, the simulations in the paper are done with OOMAO without angular spectrum propagation.

The LQG regulator robustness to elevation model mismatch was also studied. It was shown that the simulated regulators are very robust to inaccuracies in disturbance modeling, consistently leading to better simulated performance than the integrator in all reported cases. Furthermore, in the case where the overall wind profile shape was consistent despite the mismatch, the resulting performance degradation is minimal. This robustness paired with the substantial improvement in coupling efficiency across all simulated scenarios firmly establishes LQG regulators as a superior alternative to integrator control in the context of FSOC-AO for LEO links.

The impact of the improvement obtained with LQG control was evaluated for the first time for both the classical and quantum channel. The LQG22 leads to a significantly improved BER, which in turn enables higher throughput with potentially less post-processing of the channel. Moreover, the impact on the quantum channel is shown to be as high as 70 % in SKR with regards to the integrator under low elevation, stronger turbulence and scintillation LEO links. These results are indicative of a significant improvement on the link stability for the secure key generation.

The consistency and magnitude of the performance gains observed across all evaluation metrics strongly support the adoption of the LQG22 regulator as the preferred control approach for the context of FSOC-AO LEO links, especially in the particularly adverse case of the low elevation and stronger scintillation.

Chapter 5

Scintillation in FSOC simulation

The previous chapters focused on the performance of the LQG in a simulation environment including diffraction and the resulting scintillation on the WFS detector. In this section, the impact of the physical propagation is highlighted. An analysis on simulated data statistics for the phase are shown, specifically focusing on comparing geometric and ASP methods for both the phase structure function and angle-of-arrival of temporal power spectra. A potential model improvement is suggested.

5.1 Impact of physical propagation on data rates

This is achieved by comparing the differences between the geometric and physical (ASP) propagation methods. Figure 5.1 shows the same frame seen by the simulated refractive WFS, but with solely geometric propagation and with ASP (section 2.4.1). Whilst Figure 5.1a) shows a uniform illumination of the subapertures across the pupil, in 5.1b) it is visible that the individual PSFs on the WFS subapertures are affected by intensity fluctuations. The illumination across the pupil is not uniform, resulting in degraded or missing measurements. This further supports the results and comments initially made in section 3.3 for the horizontal link. Moreover, it supports the claim that the deployment of simulations with solely the geometric model leads to optimistic results.

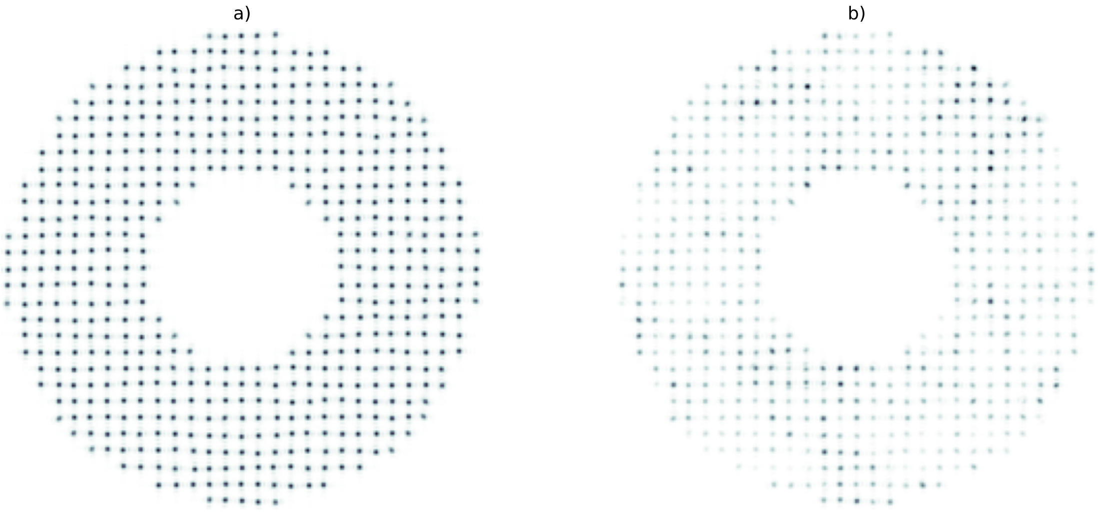

Figure 5.1: Comparison of the same frame as seen on the WFS: a) considering solely geometric propagation of light; b) considering the physical propagation method with angular spectrum propagation.

The interest in predictive control comes as a direct consequence of understanding the AO temporal error as a significant hindrance in the link budget. The alternative to predictive control would be to increase the loop frequency, which may also help mitigate the effects of scintillation. Natural questions arise then like the differences in performance between a slower LQG regulator (e.g. 2 kHz loop frequency) and a faster integrator (e.g. 5 KHz loop frequency), and the effect of propagation in this comparison.

In order to quantify these differences, a comparison between geometric and ASP was made at 30° elevation, at both 2 and 5 kHz, with LQG and integrator controllers. The results are shown in Figure 5.2.

Each plot represents 5 seconds of simulated data of the same time series (i.e. same initial phase screens) with different sampling and propagation methods, accordingly.

The results highlight the effectiveness of the predictive regulator at mitigating the fades in all cases. Focusing solely on the geometric propagation cases at 2 and 5 kHz, the LQG at 2 kHz achieves similar median coupling loss as an integrator running at 5 kHz, in agreement with (Robles et al. 2022) where the authors compare behaviors at 2 and 4 kHz in geometric propagation only. However, when considering the full physical propagation effects, the increase of severe deep fades due to scintillation is evidenced and degrade all results. Despite this, LQG median coupling at 2 kHz is still better than that of integrator at 5 kHz.

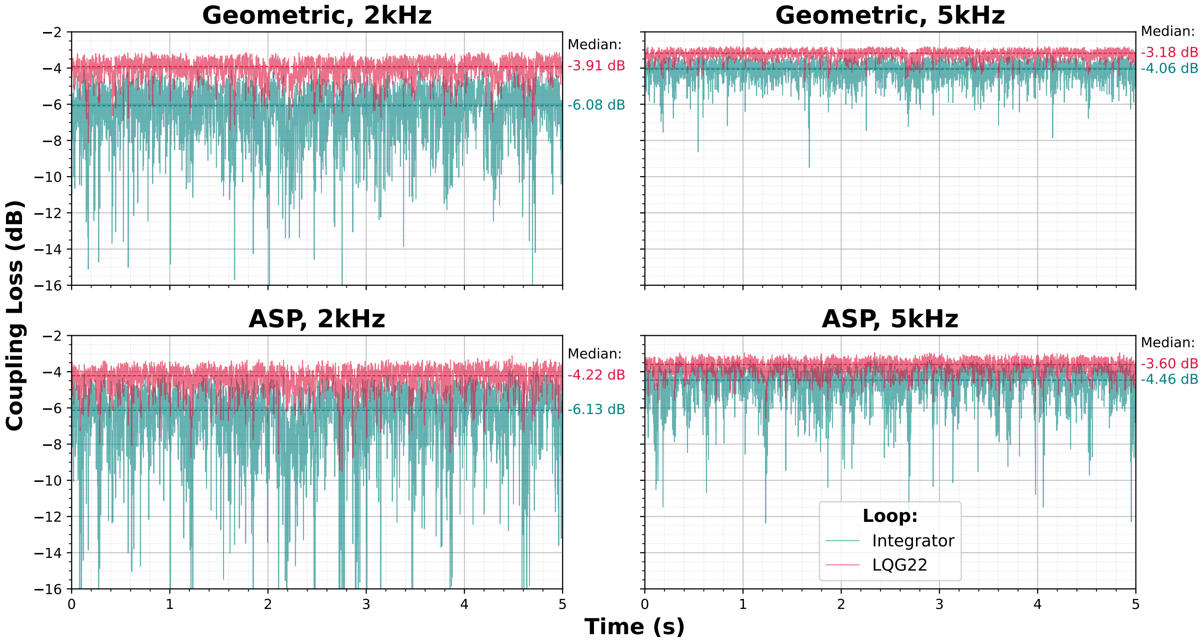

Figure 5.2: Coupling loss comparison between a tuned integrator (blue) and LQG22 (red) for SimID 30° at 2 and 5 kHz, with geometric and angular spectrum propagation methods.

The fade statistics at -3, -6 and -10 dB are shown in Table 5.1. These results support that LQG regulators are not only effective at improving median coupling efficiency but also at mitigating the fade count, depth and duration. Furthermore, whilst running the loop at higher rates decreases the fade statistics, the plot of ASP at 5 kHz shows that integrator is still affected by scintillation, as opposed to the LQG with no reported drops below 50% of the power (i.e. -3 dB fades). This suggests that simply running the integrator at higher loop frequencies is not sufficient to obtain a stable link, and an LQG regulator provides a clear advantage regardless of loop rate. This is consistent with the hypothesis that a predictive controller such as the LQG mitigates the temporal error with effective prediction when based on a relevant model.

The integrator performance at 5 kHz can be used to quantify the impact of different propagation methods. This is shown in Table 5.1. Introducing ASP increases the mean fade duration from 0.73 to 1.27 ms. Considering bandwidths of the order of 10 Tbit/s (Dochhan et al. 2019), it could represent a mean data rate loss of about 12.7 Gbit/s. This loss goes unaccounted for if only geometric simulation is used.

Finally, Figure 5.3 shows the performance of the different regulators at different loop rates for the scenarios in which physical propagation is used. The increased loop rate leads to a significant performance increase with a tuned integrator. The LQG at 2 kHz outperforms the integrator at 5 kHz due to the aforementioned ability to mitigate the fades as well as directly reduce the impact of the temporal error.

To better understand the impact of the physical propagation, the following sections provide more insight by performing an analysis to the phase statistics of simulated LEO downlink data.

Table 5.1: Fade statistics at 2 kHz and 5 kHz for integrator and LQG controllers under geometric and ASP propagation.

		−3 dB		−6 dB		−10 dB	
Controller	**Propagation**	**F/s**	**Dur.**	**F/s**	**Dur.**	**F/s**	**Dur.**
2 kHz							
Integrator	Geometric	35	1.45	6	1.13	1	0.85
	ASP	42	1.86	15	1.33	4	1.08
LQG22	Geometric	1	1.26	0	–	0	–
	ASP	3	1.02	0	–	0	–
5 kHz							
Integrator	Geometric	1	0.73	0	–	0	–
	ASP	14	1.27	2	0.62	0	–
LQG22	Geometric	0	–	0	–	0	–
	ASP	0	–	0	–	0	–

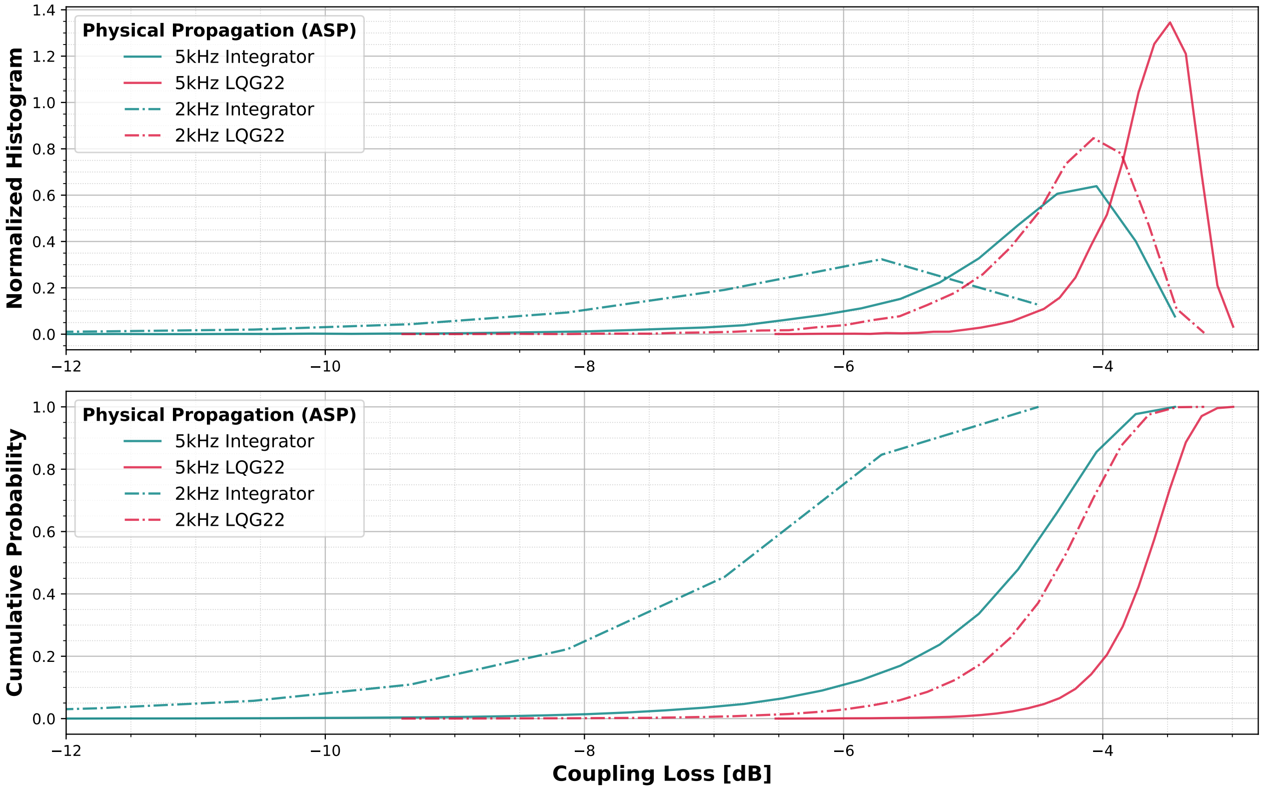

Figure 5.3: Probability density function and cumulative density function for physical propagation method controller comparison at 2 and 5 kHz.

5.2 Phase statistics analysis of simulated LEO downlink data

As has been shown before in sections 2.4.1, 3.3 and 5.1, there are significant differences between the two propagation methods. These manifest not only theoretically but also in simulation where the main consequence is to do with accounting or not for scintillation effects on the WFS. The following sections explore how different properties vary across the different propagation methods in order to better understand the spatial-temporal statistical differences in the context of FSOC downlinks.

5.2.1 Phase structure function

A phase structure function (section 2.1.1.2) expresses the squared difference of the phase with respect to the separation between two points frozen in time (section 2.1.3). In order to further assess the differences between angular and geometric propagation, phase screens were generated according to the equation (2.26) with the chosen simulation resolution of 320x320 pixels. The optical structure function was computed from the simulated phase screens by evaluating all pairwise differences within the telescope pupil. Valid points were first selected using the pupil mask, and their coordinates were extracted. The separation between each pair of valid points was calculated together with their squared phase difference. With these it was possible to represent the statistical relationship between separation in the aperture plane and phase variability. This procedure was repeated for both geometric and angular spectrum propagation. The results from this analysis are shown in Figures 5.4 and 5.5.

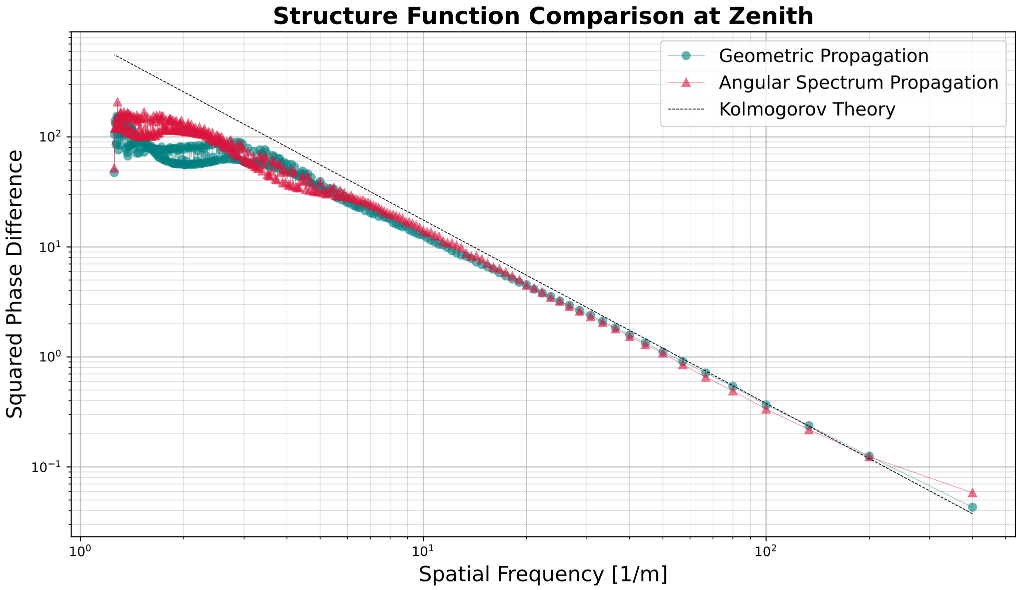

Figure 5.4: Structure Function of simulated data comparing geometric and angular spectrum propagation.

Figure 5.4 plots the occurrences of the squared phase difference over the span of resulting spatial frequencies at zenith. These results are plotted for geometric and angular spectrum propagation, and compared to the theoretical Kolmogorov decay law. The geometric curve follows a similar trend to Kolmogorov theory from about 20 m^{-1}. The structure functions demonstrate that the power-law behavior is consistent with what is expected from turbulence theory (see section 2.1.1.3). At low spatial frequencies (i.e. higher separation between considered points) the geometric and angular spectrum values decay from the Kolmogorov power law, because the phase screens were generated from von Kármán theory, which has less energy at low spatial frequencies.

Figure 5.5 plots the occurrences of the squared phase difference over the span of resulting spatial frequencies at 30°. In comparison with the previous plot, the effect of elevation on the angular spectrum propagation leads to a significant increase for higher spatial frequencies with regards to Kolmogorov spectrum at this range. At low spatial frequencies the same decay as commented above can be observed, although more marked by the strong variance for angular spectrum propagation. Over the total spectrum of spatial frequencies, the angular spectrum mode does not follow the Kolmogorov power law. As the elevation is lowered, the integrated atmospheric parameters also lower, including r_0 (as indicated in Table 4.2). Overall, this suggests that the inclusion of diffraction effects via angular spectrum propagation leads to an overall increase of the observed phase difference distribution, especially at low and high spatial frequencies. Diffraction at the aperture edges affects how phase fluctuations are transmitted, particularly at small spatial scales, which leads to departures from the ideal Kolmogorov law. Geometric models neglect diffraction and thus follow the Kolmogorov curve (besides the low spatial frequencies as mentioned above). Consequently, although geometric propagation appears to agree more closely with theory, the angular spectrum results provide a more physically realistic description of the structure function that would be observed in an optical

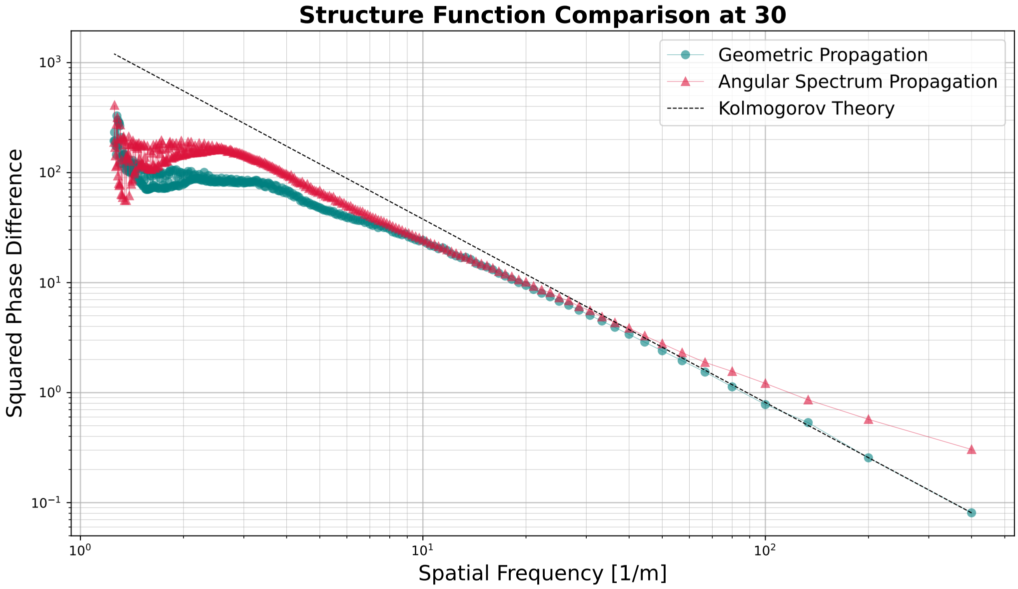

Figure 5.5: Structure Function of simulated data comparing geometric and angular spectrum propagation.

system. The inclusion of these effects is expected to better reflect the deviations seen in real optical instruments compared with the ideal Kolmogorov curve.

5.2.2 Temporal power spectra

The temporal power spectra informs on the distribution of signal power across temporal frequencies showing how different time scales contribute to power variability. The turbulence power spectral density in particular indicates which temporal frequencies dominate the wavefront fluctuations observed by the sensor. These can be obtained from open-loop SH-WFS simulated data.

For this analysis, once again the conditions described in table 4.1 were used as input parameters to the simulation engine ELSiE (see section 2.4.2) in order to obtain the phase screens. It should be noted that the phase screens for each of the turbulence layers were the same for both propagation methods (geometric and ASP, described in section 2.4.1). In order to analyse the temporal power spectra, 10 000 frames of open loop SH-WFS measurements were recorded. From these measurements, the resulting angle of arrival (AoA) was recorded. The temporal power spectra was obtained by plotting the periodogram for the AoA. This was done for the different SimIDs and displayed in Figures 5.6, 5.7 and 5.8.

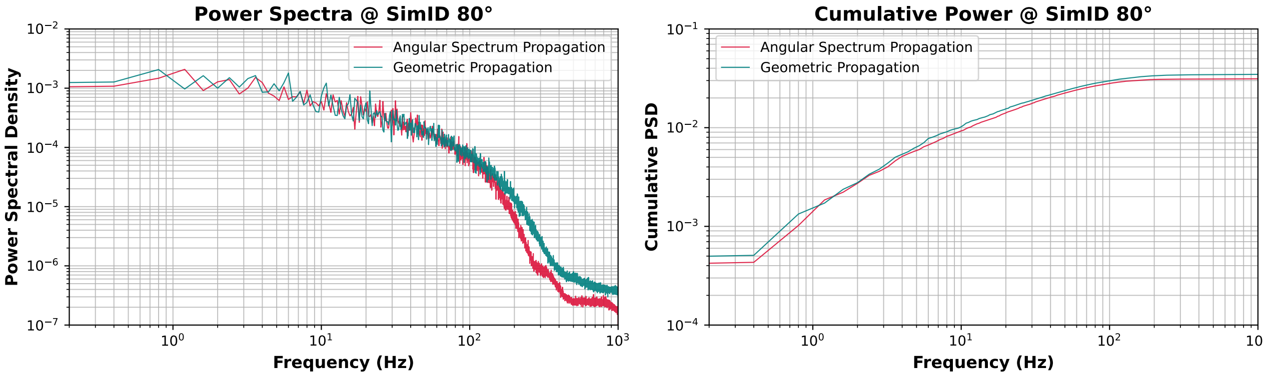

Figure 5.6: Plot of power spectral density and cumulative power spectra of angle of arrival of open-loop turbulence wavefront sensor measurements for SimID 80° with comparison between propagation methods.

Figure 5.6 shows the difference in power spectra between ASP and geometric for the case of SimID 80°. On the power spectra plot (left), at the lower frequency spectrum and up to about 150 Hz, the power distribution for both methods is very similar. However, in the high frequency regime, the power distribution resulting from ASP drops more steeply than that of geometric. Furthermore, at around 250 to 400 Hz, a "bump" appears before a plateau over the remainder of the spectra. Despite the differences at the mid-to-high frequency ranges, the cumulative power density (right) shows that both power spectral propagation methods follow a very similar energy distribution across the frequency spectrum.

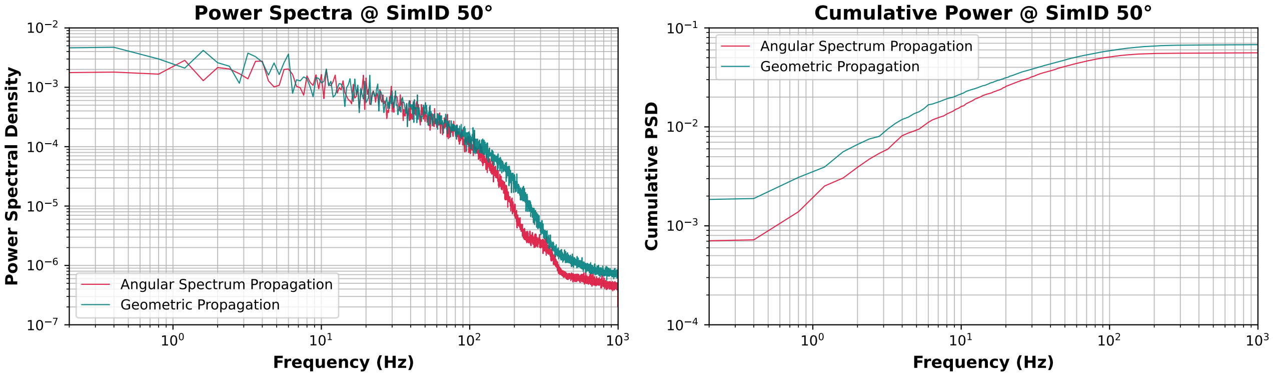

Figure 5.7: Plot of power spectral density and cumulative power spectra of angle of arrival of open-loop turbulence wavefront sensor measurements for SimID 50° with comparison between propagation methods.

Figure 5.7 shows the same comparison but for the SimID 50°. Both curves follow a similar decay law as seen for the higher elevation case. On the power spectra plot (left), at the lower frequency spectrum and up to about 100 Hz, there is once again no visible difference in the power distribution for both methods. At the high frequency regime, the power distribution resulting from ASP drops again more steeply than that of geometric, however the "bump" observed at 250 to 400 Hz range is more pronounced and leads to a plateau that is closer in energy density to the geometric distribution. The cumulative power density (right) evidences a significant difference in power level at the very low frequency spectrum (up to 1 Hz), with the distribution across the frequency spectrum accumulating at a faster rate for the ASP method than the geometric, despite the latter culminating at a slightly higher total power level.

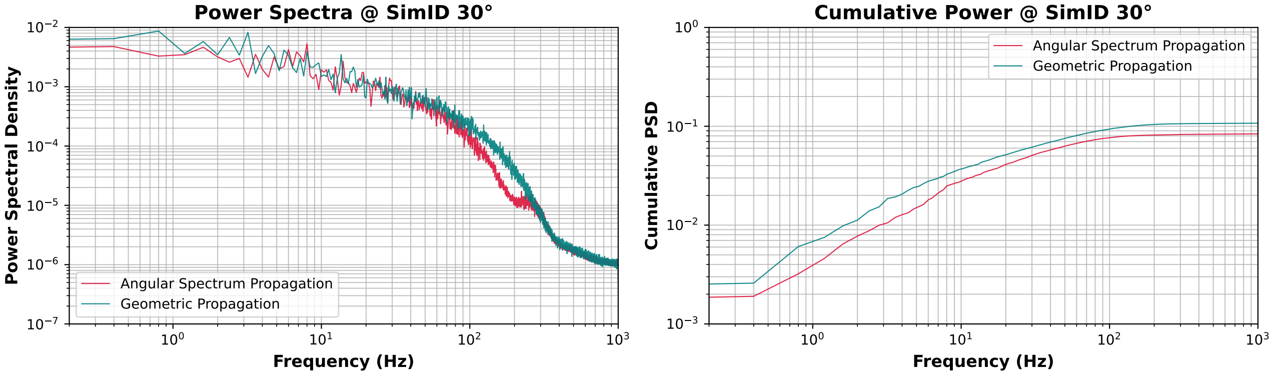

Figure 5.8: Plot of power spectral density and cumulative power spectra of angle of arrival of open-loop turbulence wavefront sensor measurements for SimID 30° with comparison between propagation methods.

Lastly, Figure 5.8 shows the same comparison but for the SimID 30°. On the power spectra plot (left), at the lower frequency spectrum and up to about 70 Hz, there is once again no visible difference in the power distribution for both methods, but the regime where ASP drops more steeply than that of geometric is visible from 70 Hz onwards up to the "bump" observed in both previous cases. Interestingly, this structural "bump" (200-300 Hz) is even more pronounced, but swiftly matches the tail end of the geometric distribution culminating at an indistinguishable energy density to the geometric distribution from 300 Hz to the end of the frequency spectrum. The cumulative power density (right) evidences a significant difference in power level at the low frequency spectrum (up to about 10 Hz), with a very similar distribution shape across the frequency spectrum for both methods, despite once again the geometric propagation curve culminating at a slightly higher total power level.

In order to ease the comparison between the behaviour of the AoA turbulent power spectral density and summarize the findings of the section so far, these same curves were gathered per method in Figure 5.9.

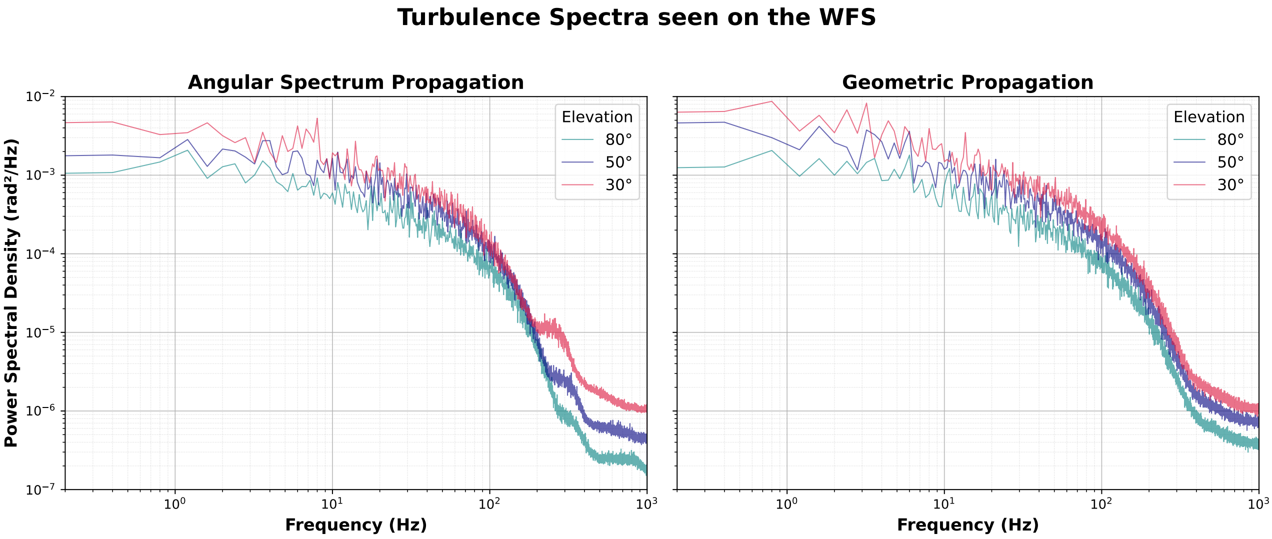

Figure 5.9: Plot of power spectral density for all considered elevation for angular spectrum propagation (left) and geometric propagation (right).

Figure 5.9 shows that the turbulence power spectra varies across elevations for both methods. In fact, as the elevation is lower, the AoA has a higher overall power distribution for both geometric and ASP. This is consistent with intuitive expectation, as the slant paths are longer and cross the turbulence structures at an angle, therefore increasing the wavefront aberrations. In the geometric case (right), the curves are in agreement with theoretical expectations (Clifford 1971).

When it comes to power distribution across the frequency spectrum for both propagation methods, a similar power decay rate is observed up to around 200 Hz, albeit with the corresponding geometric propagation scenario always reporting a slightly higher overall power distribution. This discrepancy can be understood by considering how each model handles spatial frequency content and numerical filtering. As seen in section 2.4.1, geometric propagation is solely ray-based. The power distribution is computed assuming direct propagation without accounting for phase curvature or diffraction. As a result, all spatial components are effectively preserved, leading to an idealized energy transport model that overestimates energy density in certain regions. In contrast, ASP introduces three quadratic factors to more accurately represent the propagation path of light from the source and the resulting phase and amplitude fluctuations. This method inherently acts as a spatial low-pass filter. High spatial-frequency components corresponding to fast-varying field details are naturally attenuated with distance (Goodman 2005).

The ASP plot (Figure 5.9, left) also shows the "bump" structure between about 200 to 400 Hz for all elevations. As the elevation lowers, the energy present at these frequencies is increased. Since the simulation setup and parameters to generate all plots differ only in elevation profile and propagation method, it is possible to infer that these "bumps" can represent scintillation captured by the SH-WFS. This results in subapertures being more susceptible to noise due to intensity variations, which could result in a burst of noise, changing the intensity pattern. This is consistent with the increase in scintillation as the elevation is lowered, as is represented by the Rytov variance values presented in Table 4.2. However, this mid-range frequency structure cannot be explained solely by scintillation. The ASP method is known to suffer from aliasing at high spatial frequencies (Matsushima et al. 2009). This was addressed by doubling sampling grid resolution with regards to the usual AO rule of thumb of 4 elements per r_0 or subaperture. Moreover, the presented turbulence power spectra is as measured by the simulated diffractive SH-WFS, which is known to be strongly affected by the intensity fluctuations in the detector caused by scintillation. Thus, in order to accurately assert whether this is representative of scintillation or an affect of numerical issues, further investigation is necessary.

5.2.3 Degraded measurements replacement strategy

The previous chapters highlighted the benefits of deploying an LQG regulator in FSOC for LEO links with respect to an integrator. This was illustrated on both the performance improvement at different elevations and the robustness to scintillation and model mismatch conditions. It was also shown that the performance is hindered the most at lower elevations for all regulators, although a clear advantage of LQG regulator use at worst conditions is highlighted. However, scintillation was not directly modeled onto the priors.

In this section, a possible model improvement to address the intensity fluctuations and the resulting measurement degradation on the SH-WFS is hypothesized and implemented and its impact is assessed in simulation.

The strong turbulence is expected to lead to severe scintillation on the detector subapertures, leading to fades. In turn these fades result in degraded or even missing measurements. In the context of astronomical observation, a strategy to counteract the detrimental effect of a non-circular pupil slow rotation has been proposed and validated successfully on the Gran Telescopio Canarias (GTC) AO bench (Marquis 2023) and on sky (Marquis et al. 2024). It consists in replacing degraded measurements by their prediction given by the Kalman filter which gain has been computed with an adequate noise covariance matrix that has very high values for all subapertures that are not enough illuminated (as given by the geometry of the pupil and an adequate flux threshold). The idea would be here to modify this strategy by replacing on the fly the missing measurement with its prediction given by the Kalman filter, but without updating the Kalman gain.

In order to do so, a change into the ELSiE Shack-Hartmann sensor implementation was made. The WFS was modified to admit a flux threshold, below which the subaperture in question is dismissed and its measurements at that frame are made into zero. In turn, the LQG replaces the zero measurements with the corresponding predicted measurements. This approach was then simulated for the case of SimID 30° (see Table 4.1), in the same manner as expressed in Table 4.4. The flux threshold value was tuned, i.e., several values were simulated, with the found optimal being 20% below the frame's median flux. The resulting time series was compared to that of the LQG22. This is shown in Figure 5.10.

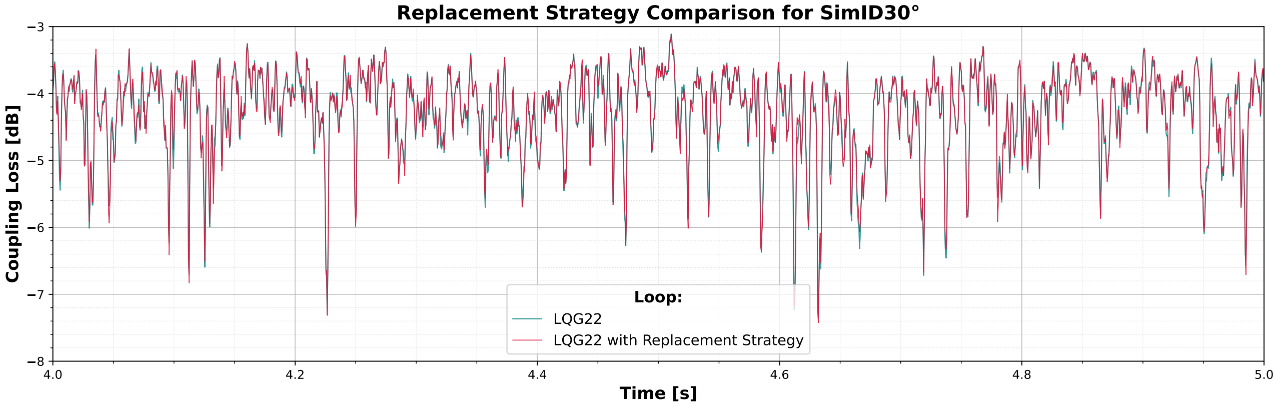

Figure 5.10: Time series comparison of LQG22 and LQG22 with replacement strategy deployed on the same phase screens over 1 second of simulated data.

From the time series, it is possible to see that the performance of the regulators is almost identical, with notable exceptions only shown at fade depth. It appears that this strategy leads to an occasional mitigation of fade depth whilst not changing the overall performance. This is further supported by observing the summary statistics in Table 5.2.

Figure 5.11 represents the normalized histogram and cumulative probability for both regulators for direct comparison. It is shown that the distributions are practically overlapping, thus supporting that no performance gain is obtained with this replacement strategy.

Table 5.2: Performance summary for SimID 30°for LQG22 with and without replacement strategy (RS). Coupling loss mean and median, as well as fade statistics at thresholds of $-3\,\mathrm{dB}$, $-6\,\mathrm{dB}$, and $-10\,\mathrm{dB}$ with fade count per second (F/s) and mean fade duration (ms).

SimID 30°	Coupling Loss (dB)		−3 dB		−6 dB		−10 dB	
	Mean	Med.	F/s	ms	F/s	ms	F/s	ms
LQG22	-4.35	-4.21	3	1.02	0	–	0	–
LQG22 w/ RS	-4.35	-4.21	3	1.03	0	–	0	–

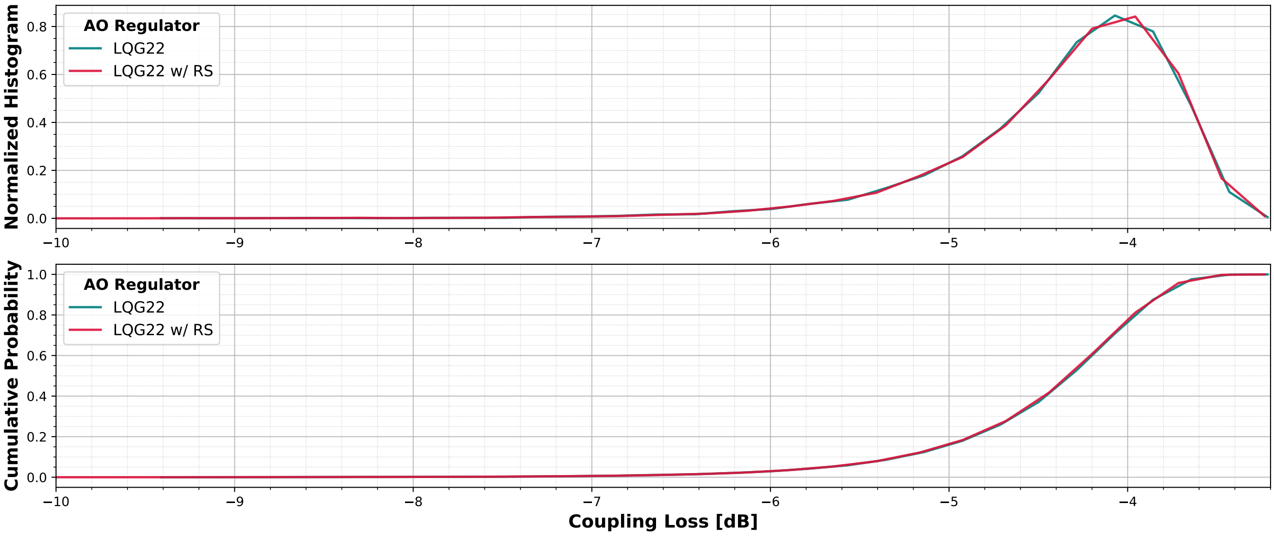

Figure 5.11: Coupling loss comparison of LQG22 and LQG22 with replacement strategy.

In summary, the replacement strategy as implemented here does not seem to bring any significant improvement in the context of LEO FSOC AO links besides the occasional fade depth mitigation. However, since fades can represent a significant drop in data-rates, that added mitigation with apparently no trade-off could prove to be useful. Furthermore, the tests here summarized represent only a "binary" threshold implementation: the subaperture flux is either above or below the 20 % threshold. More dynamic configurations remain to be explored, including a real-time Kalman gain adaptation, and could prove to be interesting. Therefore, more investigation into this technique in the scope of FSOC-AO is recommended.

5.3 Summary

In this chapter, the impact of scintillation on FSOC-AO was assessed. A comparison was made between geometric and ASP methods at both 2 and 5 kHz. It was shown that with phyisical propagation there is a significant increase in fade events which degraded all results. Despite the fades, the LQG regulator at 2 kHz outperforms the integrator at 5 kHz and was shown to effectively reduce the impact of the intensity fluctuations.

The square phase difference was plotted across the spatial frequency spectrum in order to assess the structure function difference between propagation methods. It was shown that whilst at zenith both methods lead to the Kolmogorov power decay law, at 30 ° the ASP seems to follow a different decay law.

The power spectral density at the different elevations evidenced scintillation-induced intensity fluctuations captured by the simulated SH-WFS. Additional research is required to separate true scintillation effects from residual aliasing.

Finally, a first-step towards mitigating scintillation by using a degraded measurement replacement strategy was tried. This did not yield conclusive results and more investigation into dynamic configurations for this replacement technique are recommended.

Chapter 6

Conclusion and perspectives

6.1 Conclusion

The work presented in this thesis builds upon existing research on LQG control for AO and extends it to FSOC applications, considering for the first time LEO links under low elevation and adverse scintillation conditions. A zonal-based LQG approach was chosen for its capability to preserve the underlying spatio-temporal structures of turbulent behaviour, which is especially advantageous for dominant frozen-flow effects such as the apparent wind resulting from LEO orbit. A Python package was developed in order to facilitate the development and synthesis of LQG controllers. It was developed with integration into the existing AO simulation tool in mind. The resulting simulation environment was cross-validated by replicating published results. Different LQG configurations were tested and simulated against a tuned integrator for performance comparison. The inclusion of diffraction into simulation environment was evaluated.

Initial simulations were run using a zonal-based LQG regulator, with theoretical priors generated from covariance matrices using the Yule-Walker method for an autoregressive model of the second order (Correia et al. 2015; Prengère et al. 2020), and including oversampling of the phase (Prengère et al. 2020). The regulator was simulated in a horizontal link with strong boiling turbulence. It was compared to an integrator both with and without diffraction effects, that is with angular spectrum propagation or without (so geometric propagation). The account for physical propagation in AO control for LEO satellites with an LQG regulator in the loop has not been simulated in previous works. It was shown here that the LQG controller outperformed the integrator in both simulation conditions. The inclusion of scintillation effects led to a drop in coupling efficiency of 56.4-69.8 % for each regulator under matching conditions, with the only different variable being the chosen propagation method. These results represent the first evidence that neglecting scintillation in FSOC-AO simulations may lead to unrealistically favorable outcomes when assessing control performance.

In order to approximate simulations to real conditions, a LEO orbit satellite (HyDRON) pass over the OGS-OP was considered for the atmospheric profile, corresponding to the worst case for daytime conditions (Torre et al. 2024). Different simulation conditions were then computed at three different elevations, with resulting turbulence models containing dominant frozen-flow effects. In these reported conditions, several architectures of zonal-based LQG regulators were simulated and compared to an integrator. It was shown that oversampling of the phase prediction grid in the Kalman filter led to a mean improvement of 1.38 ± 0.02 dB over the non-oversampled LQG regulator and to a reduction of 85 % on the -3 dB fade events, establishing this technique as a key factor to consider when synthesizing LQG controllers in the context of FSOC-AO, particularly for LEO links in low elevation. It was also shown that extending the pupil seems to lead to a minor improvement in the form of occasional fade depth mitigation. Thus the best performing regulator incorporated both oversampling and extending the pupil edge. Simulating such LQG controller at the different elevations experienced during a LEO link revealed that LQG significantly outperformed the integrator. In fact, the LQG controller in its worst performing scenario (low elevation) still outperformed the integrator in its best performing scenario (high elevation). Moreover, it was shown that this still holds true for the case of a model mismatch in elevation, i.e., an LQG regulator synthesized with priors for the case of low elevation deployed also on the mid and high elevations still outperforms the integrator. The LQG controller with oversampling and edge compensation led to the most significant increase in performance at a 30° elevation with respect to the integrator. In that configuration, the coupling efficiency as given by the

-3 dB fades are reduced by 93 %, and their mean duration shortened by about 45 %, whilst the deeper fade levels are fully mitigated. These original results in conditions of low elevation and strong scintillation support the proposition of LQG predictive AO control as a robust alternative to traditionally deployed integrator control capable of withstanding the adverse conditions experienced in LEO downlinks.

In order to further assess the impact of the scintillation on the LEO downlink scenario, a comparison was made between geometric and angular spectrum propagation for the case of low elevation. Including physical propagation effects in simulation was shown to lead to a significant fade count increase. This shows that the usual geometric propagation under represents the fade events by not accounting for scintillation. As a consequence, geometric simulation results were shown to be optimistic, especially at lower elevation. It was also shown that the impact likely comes from intensity variations induced on the SH-WFS leading to degraded measurements. These results go hand-in-hand with theoretical expectations (Fried et al. 1992). A further improvement was tested that targeted specifically the adverse effect of scintillation by flagging the degraded measurements and replacing them with the corresponding prediction. This was not shown to bring any improvement in its reported form. Further research into the method and potential improvements is recommended.

The hypothesis that simply increasing loop frequency could bypass the need for predictive controllers was also taken into account. In order to assess the claim, the loop frequency was increased from 2 to 5 kHz, simulating both LQG control and integrator, with and without scintillation effect. It was shown that increasing the loop frequency to 5 kHz improved performance for all regulators. However, the LQG considerably increases the median coupling and lowers fade counts, without any fade below -3 dB, which demonstrates a robustness vital for FSOC-AO. Furthermore, the LQG regulator at 2 kHz outperforms the integrator controller at 5 kHz, showing that simply increasing the loop rate is not sufficient to counteract the effect of scintillation. These results are consistent with long standing reports in astronomy AO that deploying an LQG improves the performance, bypassing the need to increase the loop rate (Conan et al. 2011). This has more recently been confirmed to also be the case for coupling efficiency in geometric propagation simulations (Robles et al. 2022). Therefore, it was shown that even when running the loop at 5 kHz there are significant advantages to deploying an LQG regulator.

Additionally, an analysis was performed on the phase statistics. The temporal power spectra of open loop simulated turbulence was computed for both low and high elevation cases, with and without scintillation. It was shown that the inclusion of scintillation causes the temporal power spectra to depart from the geometric case for the higher frequencies, an effect particularly noticeable for the low elevation case. Furthermore, the squared difference between points of the phase screen was compared against the von Kármán structure function. It was found that the low elevation case with scintillation departs from the theoretical Kolmogorov decay law and significantly overshoots it for higher spatial frequencies. This analysis was complemented with a wavefront sensing study in order to assess the implications of using an SH-WFS in strong scintillation. A comparison with open loop measurements and phase reconstruction was made. It was observed that the intensity fluctuations from diffraction seem to affect the phase reconstruction the most at lower elevations, leading to an increased error. These results were once again consistent with the hypothesis that the intensity fluctuations resulting from diffraction via angular spectrum propagation are most critical at lower elevations.

The impact of LQG control on communication channels is here addressed for the first time, both for classical and quantum communication channels. On the classical communication channel, it was shown that deploying the LQG regulator enabled a steeper decrease of the BER with the SNR increase with regards to traditionally deployed integral action control, achieving a quasi-error free BER pre-FEC, which can drastly reduce reliance on post processing. As for the potential impact on the quantum communication channel, it was found that deploying an LQG regulator enabled a modest improvement on the QBER, which in turn led to a significant improvement on SKR, increasing the key rate by 23 %. This is a fundamental first step towards enabling QKD on-sky with LEO satellites, where the stringent link budgets are expected to limit the quantum capacity. These studies suggests that QKD applications in FSOC-AO will significantly benefit from the LQG control deployment.

6.2 Comments and perspectives

The initial results presented on the horizontal link were based on particularly adverse turbulence conditions resulting in a very strong scintillation case. The horizontal link was designed to emulate worst case scenario turbulence over a GEO link. However, it's possible that this is not entirely representative of the satellite links and that this might be an edge case when it comes to very pronounced scintillation effects. Furthermore, the LQG controller used for this case was synthesized using a disturbance model more adapted to a frozen-flow turbulence scenario than to the boiling case. These results should not lead to the interpretation that an LQG controller is inadequate to such a scenario but rather that a different methodology for modeling the disturbance should be sought out. Should there be interest in pursuing further research in horizontal links, the considered scenarios should include scintillation and alternative disturbance models well-suited to the boiling can be used, as shown in (Prengère et al. 2020).

The target scenario for the controller synthesis and simulations was LEO downlinks. The HydRON LEO profiles for daylight turbulence were chosen as a representative example given the impact of the project and availability of the information. In the calculations for these profiles, the flat-Earth model was used, and the parameters were chosen as an average of several different sites across Europe. In future calculations where a more accurate model is needed for a precise location, it is recommended to use the more accurate round-Earth model, to ensure the increased propagation length at lower elevations is accounted for. These can be found for example in Andrews & Phillips (Andrews et al. 2005).

In the context of LEO satellite downlinks, oversampling of the phase grid was shown to be the most significant model improvement. Within the context of this work, only an oversampling by a factor of 2 was considered. This increases the number of phase points, and thus the calculation load of matrices. Increasing further the oversampling factor could be beneficial and deeper investigation into a trade-off is warranted. Should the vectors and matrices become too large, it is possible to deploy sparse matrix techniques, preserving only the needed information and saving computational resources. It is however important to note that when it comes to real-time computation the critical path that goes from measurements to commands application has exactly the same complexity as the integrator whatever the state size (Marquis 2023). Remaining calculations can then be done efficiently in idle time thanks to parallelization, all the more when the model is expressed in a zonal basis. The recent fully decoupled LQG AO regulator in the Fourier domain is a good example of real-time optimization and runs at 8 kHz (Poyneer et al. 2023).

Besides the reported successful model improvements, some additional strategies should be considered. A replacement strategy was tested, consisting of replacing degraded measurements by their prediction given by the Kalman filter. This did not lead to any significant performance improvement. It is however important to note that the method tested consisted of a fairly simplified binary approach with a pre-defined threshold based on the overall pupil illumination. Possible improvements to the methodology could be further investigated, such as the ones suggested in (Marquis 2023), where a dynamic approach was shown to bring significant improvement due to the pupil rotation. This would translate into a Kalman gain modification at each step, either by using a non-asymptotic Kalman filter, or by adapting the asymptotic gain according to SNR. This could become relevant when moving to bench demonstration and should therefore be kept in mind. Additionally, throughout this thesis the phase-to-commands projector goes through the measurement space ($M_{com}D$). However, it has been shown that improving the resolution of the phase estimation ahead of its projection onto the DM can significantly improve the overall LQG performance (Prengère et al. 2020). Therefore, it would be useful to finely interpolate the phase (for example using a Maximum A Posteriori estimator) before the multiplication by the WFS matrix D which also needs to be modified to account for a fine phase grid. The other possibility would be to resort to the projector $N^\dagger$, the influence matrix N being defined on a fine phase grid and obtained from a pseudo-synthetic interaction matrix identified from calibration. It is thus recommended to pursue the integration of a projector that embeds a resolution improvement of the phase, which can be done with no additional real-time cost.

The results for the LQG control in the context of FSOC-AO for LEO downlink illustrated a robustness to fades and improved median coupling loss. These significant improvements motivate the steps towards lab demonstration and on-sky implementation. While lab conditions can be controlled, on-sky conditions change quickly. The LQG controllers here considered are based on time invariant parameters with an infinite horizon criterion (residual phase variance) enabling use of asymptotic Kalman gain without loss of optimality. In practice evolving turbulent conditions require regular updates of the state model to ensure high performance. An autonomous LQG controller (with automatic controller updates) has been for example successfully validated on sky on GTC (Gran Telescopio Canarias) on the GTCAO system (Galland et al. 2024; Marquis et al. 2025). Note that this autonomous LQG regulator mixes models based on machine learning techniques and priors learned from telemetry data. This strategy can be integrated easily in the proposed state-space framework by for example mixing the zonal model which is efficient for frozen flow representation with machine learning for the ground layer model. Another interesting way of mixing boiling and frozen flow is the one proposed in (Juvénal et al. 2016) where a tuning parameter allows to balance between the two behaviours. Model mixtures for LQG regulators would definitely deserve further studies.

In LEO applications, elevation plays a crucial role in terms of AO control performance. As the elevation is lowered, so is the median coupling loss, and the fade counts increase. However, it was shown that even with incorrect elevation priors, the LQG controller has systematically outperformed the integrator. For on-sky applications where elevation will evolve rapidly, this suggests too frequent controller updates should not be needed. In the cases where it might be necessary, it is important to note that these periodical regulator updates may lead to transients in feedback loops. If these control "bumps" are present, they could potentially be detrimental to performance, and mitigation techniques should therefore be considered, such as the anti-bump adapter reported in (Raynaud et al. 2024).

When it comes to the inclusion of scintillation into simulation, this was shown to be particularly fundamental at low elevations. However, the study presented only focused on downlink. It has been shown that scintillation on the uplink is more particularly detrimental to the link channel (Andrews et al. 2000). The deployment of predictive control also considering the uplink channel has the potential to improve predistortion in the direction of the point-ahead-angle and mitigate the scintillation-induced performance loss. Additional investigation into pre-distortion with LQG regulators is encouraged.

The numerical simulations here presented and the performance improvements enabled by the LQG controller in coupling loss constitute very compelling evidence to move forward with LQG control towards bench validation and then on-sky. A successful bench validation was presented by Kyliann Robert, in which an LQG controller built from a Zernike-based AR1 model was tested with a single phase screen in the experimental bench PICOLO+LISA as a first step towards possibly testing an AR2 model (Robert et al. 2025). This further motivates the continued development of the work carried out in the context of this thesis towards on-sky.

Future development plans should start with a laboratory validation of the integration of the LQG regulator into the real-time controller at DLR. This initial validation with a controller bench environment should support the seamless integration into the OGS-OP with the ultimate goal of carrying out successful satellite links. An on-sky validation is expected to further reinforce the critical role of predictive control in FSOC-AO, particularly in enabling secure communications through QKD by supporting high secret key generation rates. Such validation could enable the use on different applications such as satellite imaging and eventually tracking of space debris.

Ultimately, the work hereby presented provides compelling evidence that FSOC-AO with predictive LQG control has the strong potential to support Europe in securing space communication infrastructure with QKD and enable higher data rates for the next generation of strategic space missions such as HyDRON and EAGLE-1 (Calistro-Rivera et al. 2024).

Publications and Workshops

Proceeding of international conference

- J. S. Torres, A. P. Reeves, C. Kulcsár, H.-F. Raynaud, R. M. Calvo, and H. F. Kelemu (2022). *Turbulence characterization of a free space optical communication link for high performance adaptive optics control*. In *Adaptive Optics and Applications*, paper OF2B–2. Optica Publishing Group.

Peer-reviewed journal

- J. S. Torres, H.-F. Raynaud, I. R. Hristovski, G. La Torre, D. Laidlaw, A. P. Reeves, and C. Kulcsár (2025). *Predictive adaptive optics optimal control for LEO communications in low elevation and strong scintillation conditions*. Published in *Optics Express*.

Workshops

- J. S. Torres. Participated in the *European Adaptive Optics Summer School 2021*, organized by Laboratoire Charles Fabry – Institut d'Optique Graduate School (LCF–IOGS), held online, 2021.
- J. S. Torres *Predictive Control Schemes for Adaptive Optics in Free Space Optical Communication*. Presented at *RTC4AO 2023 – Real-Time Control for Adaptive Optics Workshop*, Paris, France.
- J. S. Torres, H.-F. Raynaud, D. J. Laidlaw, A. P. Reeves, and C. Kulcsár. *Predictive Adaptive Optics Control in Free Space Optical Communications for LEO Downlinks*. Poster presented at *COAT 2025 – Communications and Observations through Atmospheric Turbulence*, Munich, Germany, 2025.

Bibliography

Airbus Defence and Space (2020). *Radar Constellation for Earth Observation and Defence*. Accessed: September 26, 2024. url: `https://intelligence.airbus.com/imagery/our-optical-and-radar-satellite-imagery/radar-constellation/`.

Amazon (2024). *Project Kuiper: Delivering fast, affordable broadband to unserved and underserved communities around the world*. Accessed: September 26, 2024. url: `https://www.aboutamazon.com/what-we-do/devices-services/project-kuiper`.

Andrews, L. C. and R. L. Phillips (2005). *Laser Beam Propagation through Random Media*. Bellingham, WA: SPIE Press.

Andrews, Larry C, Ronald L Phillips, and Cynthia Y Young (2000). “Scintillation model for a satellite communication link at large zenith angles”. In: *Optical Engineering* 39.12, pp. 3272–3280.

Assémat, François, Richard W Wilson, and Eric Gendron (2006). “Method for simulating infinitely long and non stationary phase screens with optimized memory storage”. In: *Optics express* 14.3, pp. 988–999.

Babcock, H. W. (1953). “The possibility of compensating astronomical seeing”. In: *Publications of the Astronomical Society of the Pacific* 65.386, pp. 229–236.

Barchers, Jeffrey D, David L Fried, Donald J Link, Glenn A Tyler, William Moretti, Terry J Brennan, and Robert Q Fugate (2003). “Performance of wavefront sensors in strong scintillation”. In: *Adaptive Optical System Technologies II*. Vol. 4839. SPIE, pp. 217–227.

Beesley, L. F., R. Griffiths, K. Hartley, O. J. D. Farley, F. Quatresooz, A. Rodríguez-Gómez, A. Comerón, M. Townson, D. Alaluf, and J. Osborn (Mar. 2025). “Demonstration of 24-hour continuous optical turbulence monitoring in a city”. In: *Opt. Express* 33.5, pp. 10140–10149. doi: `10.1364/OE.543144`. url: `https://opg.optica.org/oe/abstract.cfm?URI=oe-33-5-10140`.

Berkooz, Gal, Philip Holmes, and John L. Lumley (1993). “The proper orthogonal decomposition in the analysis of turbulent flows”. In: *Annual Review of Fluid Mechanics* 25.1, pp. 539–575.

Bonnefois, A., C. Petit, J.M. Conan, A. Durecu, F. Gustave, C. Lim, J. Montri, L. Paillier, P. Perrault, M.T. Velluet, J.B. Volatier, and N. Vedrenne (2023). “FEELINGS, ONERA’s optical ground terminal for AO pre-compensated GEO feeder links demonstration”. In: *International Conference on Space Optics — ICSO 2022*. Ed. by Kyriaki Minoglou, Nikos Karafolas, and Bruno Cugny. Vol. 12777. International Society for Optics and Photonics. SPIE, 127771P. doi: `10.1117/12.2689677`. url: `https://doi.org/10.1117/12.2689677`.

Bonnefois, A. Montmerle, J. -M. Conan, C. Petit, C. B. Lim, V. Michau, S. Meimon, P. Perrault, F. Mendez, B. Fleury, J. Montri, and N. Védrenne (2019). “Adaptive optics pre-compensation for GEO feeder links: the FEEDELIO experiment”. In: *International Conference on Space Optics — ICSO 2018*. Ed. by Zoran Sodnik, Nikos Karafolas, and Bruno Cugny. Vol. 11180. International Society for Optics and Photonics. SPIE, p. 111802C. doi: `10.1117/12.2536003`.

Born, Max and Emil Wolf (2019). *Principles of Optics: Electromagnetic Theory of Propagation, Interference and Diffraction of Light*. 60th Anniversary Edition. Cambridge, UK: Cambridge University Press. isbn: 978-1-108-47743-7.

Calistro-Rivera, Gabriela, Oliver Heirich, Amita Shrestha, Agnes Ferenczi, Alexandru Duliu, Jakob Eppinger, Bruno Femenia Castella, Christian Fuchs, Elisa Garbagnati, Douglas Laidlaw, et al. (2024). “Building Europe’s first space-based Quantum Key Distribution system–The German Aerospace Center’s role in the EAGLE-1 mission”. In: *arXiv preprint arXiv:2412.03222*.

Calvo, Ramon Mata, Juraj Poliak, Janis Surof, Andrew Reeves, Mathias Richerzhagen, Helawae Friew Kelemu, Ricardo Barrios, Carlos Carrizo, Raphael Wolf, Fabian Rein, Annika Dochhan, Karen Saucke, and Wolfram Luetke (2019). “Optical technologies for very high throughput satellite communications”. In: *Free-Space Laser Communications XXXI*. Ed. by Hamid Hemmati and Don M. Boroson. Vol. 10910. International Society for Optics and Photonics. SPIE, 109100W. doi: `10.1117/12.2513819`. url: `https://doi.org/10.1117/12.2513819`.

Chernov, L. A. (1960). *Wave Propagation in a Random Medium*. Translated from Russian by R.A. Silverman. New York: McGraw-Hill.

Clifford, S. F. (Oct. 1971). “Temporal-Frequency Spectra for a Spherical Wave Propagating through Atmospheric Turbulence”. In: *J. Opt. Soc. Am.* 61.10, pp. 1285–1292. doi: `10.1364/JOSA.61.001285`. url: `https://opg.optica.org/abstract.cfm?URI=josa-61-10-1285`.

Conan, JM, HF Raynaud, C Kulcsár, S Meimon, and G Sivo (2011). “Are integral controllers adapted to the new era of ELT adaptive optics?” In: *AO4ELT2*.

Conan, R, J Borgnino, A Ziad, and F Martin (2000). “Analytical solution for the covariance and for the decorrelation time of the angle of arrival of a wave front corrugated by atmospheric turbulence”. In: *Journal of the Optical Society of America A* 17.10, pp. 1807–1818.

Conan, R and Carlos Correia (2014). “Object-oriented Matlab adaptive optics toolbox”. In: *Proceedings of SPIE - The International Society for Optical Engineering*. Vol. 9148, p. 91486C. doi: `10.1117/12.2054470`.

Consortini, A and L Ronchi (1972). “Choice of the model of atmospheric turbulence”. In: *Applied Optics* 11.5, pp. 1205–1211.

Correia, Carlos, Henri-François Raynaud, Caroline Kulcsár, and Jean-Marc Conan (2010). “On the optimal reconstruction and control of adaptive optical systems with mirror dynamics”. In: *J. Opt. Soc. Am. A* 27.2, pp. 333–349. doi: `10.1364/JOSAA.27.000333`.

Correia, Carlos M, Kate Jackson, Jean-Pierre Véran, David Andersen, Olivier Lardière, and Colin Bradley (2015). “Spatio-angular minimum-variance tomographic controller for multi-object adaptive-optics systems”. In: *Applied optics* 54.17, pp. 5281–5290.

Dochhan, Annika, Juraj Poliak, Janis Surof, Mathias Richerzhagen, Helawae Friew Kelemu, and Ramon Mata Calvo (2019). “13.16 Tbit/s Free-space Optical Transmission over 10.45 km for Geostationary Satellite Feeder-links”. In: *Photonic Networks; 20th ITG-Symposium*, pp. 1–3.

Dray, Jonathan, Baptiste Sinquin, Morgan Gray, Benoit Neichel, Cédric Taïssir Héritier, Carlos M. Correia, Raissa Camelo, Jalo Nousiainen, Thierry Fusco, Cyril Petit, Armin Schimpf, and Julien Charton (2024). “Comparison of predictive control laws in adaptive optics for free-space optical communications”. In: *Adaptive Optics Systems IX*. Ed. by Kathryn J. Jackson, Dirk Schmidt, and Elise Vernet. Vol. 13097. International Society for Optics and Photonics. SPIE, 130977W. doi: `10.1117/12.3019728`.

Ellerbroek, Brent L. (2002). “Efficient computation of minimum-variance wave-front reconstructors with sparse matrix techniques”. In: *J. Opt. Soc. Am. A* 19.9, pp. 1803–1816. doi: `10.1364/JOSAA.19.001803`.

ESA (2020). *ARTES 4.0: Advanced Research in Telecommunications Systems*. Tech. rep. ESA Telecommunications and Integrated Applications.

— (2023). *ESA Specification for Terabit/sec Optical Links (ESTOL)*. Public Report. ESA Connectivity and Secure Communications.

European Space Agency (2023). *ESA Specification for Terabit/sec Optical Links (ESTOL)*. Tech. rep. ESA Public Report.

Fried, D. L. and G. A. Tyler (1981). *Strategic laser communications uplink analysis*. Tech. rep. Rome, New York, USA: Defense Advanced Research Projects Agency (DARPA).

Fried, David L (1982). “Anisoplanatism in adaptive optics”. In: *Journal of the Optical Society of America* 72.1, pp. 52–61.

Fried, David L and Jeffrey L Vaughn (1992). “Branch cuts in the phase function”. In: *Applied Optics* 31.15, pp. 2865–2882.

Fuchs, Christian, Florian Moll, Juraj Poliak, Andrew Reeves, and Christopher Schmidt (2023). “Optical Satellite Links for telecommunications and time-transfer”. In: *2023 IEEE International Conference on Space Optical Systems and Applications (ICSOS)*. IEEE, pp. 168–174.

Fusco, J.-M. Conan, V. Michau, L. M. Mugnier, and G. Rousset (Nov. 1999). “Efficient phase estimation for large-field-of-view adaptive optics”. In: *Opt. Lett.* 24.21, pp. 1472–1474. doi: `10.1364/OL.24.001472`. url: `https://opg.optica.org/ol/abstract.cfm?URI=ol-24-21-1472`.

Gaddis, John Lewis (2006). *The Cold War: A New History*. Penguin.

Galland, Nicolas, Lucas Marquis, Henri-François Raynaud, James Osborn, José Marco de La Rosa, Icíar Montilla, Óscar Tubío Araújo, Marcos Reyes García-Talavera, and Caroline Kulcsár (2024). “Autonomous predictive control for the Gran Telescopio Canarias Adaptive Optics (GTCAO) system within the H2020 ORP project: progress and initial results”. In: *Adaptive Optics Systems IX*. Vol. 13097. SPIE, pp. 1908–1914.

Gemini VII Mission Evaluation Team (1966). *Gemini Program Mission Report: Gemini VII*. Tech. rep. Washington, D.C.: National Aeronautics and Space Administration (NASA).

Gerard, Benjamin L., Aaron Lemmer, Bautista R. Fernandez, Xiaoxing Xia, Cesar Laguna, Mike Kim, Stephen Mark Ammons, Brian Bauman, and Lisa Poyneer (2024). “The focal-plane actualized shifted technique realized for a Shack Hartmann Wavefront Sensor (fastrSH-WFS)”. In: *Adaptive Optics Systems IX*. Ed. by Kathryn J. Jackson, Dirk Schmidt, and Elise Vernet. Vol. 13097. International Society for Optics and Photonics. SPIE, 130973T. doi: `10.1117/12.3018223`.

Goodman, Joseph W. (2005). *Introduction to Fourier Optics*. 3rd. Greenwood Village, CO: Roberts & Co.

Greenwood, D. P. (1977). “Bandwidth specification for adaptive optics systems”. In: *JOSA* 67.3, pp. 390–393.

GSMA (2023). *The State of Mobile Internet Connectivity Report 2023*. Tech. rep. Accessed: September 26, 2024. GSMA. url: `https://www.gsma.com/r/wp-content/uploads/2023/10/The-State-of-Mobile-Internet-Connectivity-Report-2023.pdf`.

Hardy, J. W. (1978). “Active optics: a new technology for the control of light”. In: *Proceedings of the IEEE* 66.6, pp. 651–697.

Hardy, John W. (1998). *Adaptive Optics for Astronomical Telescopes*. Oxford Series in Optical and Imaging Sciences. New York, NY: Oxford University Press. isbn: 9780195090192.

Harger, Robert O. (1967). “On Processing Optical Images Propagated Through the Atmosphere”. In: *IEEE Transactions on Aerospace and Electronic Systems* AES-3.5, pp. 819–828. doi: `10.1109/TAES.1967.5408870`.

Häusler, Stefanie, Davide Orsucci, Andrew Reeves, and Florian Moll (2023). “Evaluation of integration concepts of Optical Ground Stations for satellite-based Quantum Key Distribution into a quantum network”. In: *2023 IEEE International Conference on Space Optical Systems and Applications (ICSOS)*. IEEE, pp. 209–216.

Häusler, Stefanie, Davide Orsucci, Leonard Vollmann, Eltimir Peev, and Florian Moll (2024). “Measurement-based characterization of atmospheric background light in satellite-to-ground quantum key distribution scenarios”. In: *Optical Engineering* 63.4, pp. 041211–041211.

Hecht, Eugene (2017). *Optics*. 5th. New York, NY, USA: Pearson. isbn: 978-0-13-397722-6.

Heritier-Salama, Cedric Taïssir (2019). “Innovative calibration strategies for large adaptive telescopes with pyramid wave-front sensors”. PhD thesis.

Hristovski, Ilija R. (Aug. 2025). “Pre-distortion adaptive optics for free-space optical communications”. PhD thesis. The University of British Columbia (Okanagan), College of Graduate Studies, Electrical Engineering.

Hristovski, Ilija R., Adrian Romero Campelo, Bruno Femenía-Castella, Esther Doensdorf-Sternal, Alexandru O. Duliu, Stefanie Haeusler, Jonathan F. Holzman, Kai Klemich, Douglas J. Laidlaw, Thomas Marynowski, Jonas W. Muegge, Juraj Poliak, Johannes Prell, Samuele Raffa, Linus A. Reger, Jonas Rittershofer, Karen Saucke, Veronica Spirito, Joana S. Torres, Paul Wagner, and Andrew Reeves (2024a). “Pre-distortion adaptive optics: experimental results from bi-directional tracking links between DLRs TDP-1 terminal". In: *Free-Space Laser Communications XXXVI*. Ed. by Hamid Hemmati and Bryan S. Robinson. Vol. 12877. International Society for Optics and Photonics. SPIE, p. 1287718. doi: 10.1117/12.3001682. url: https://doi.org/10.1117/12.3001682.

Hristovski, Ilija R., James Osborn, Ollie J. D. Farley, Matthew J. Townson, Ramon Mata Calvo, Bruno Femenía-Castella, Joana S. Torres, Jonathan F. Holzman, and Andrew P. Reeves (June 2024b). "Pre-distortion adaptive optics for optical feeder links: simulations and performance analyses". In: *Opt. Express* 32.12, pp. 20976–20991. doi: 10.1364/OE.521494. url: https://opg.optica.org/oe/abstract.cfm?URI=oe-32-12-20976.

Juvénal, Rémy, Caroline Kulcsár, Henri-François Raynaud, and Jean-Marc Conan (2016). "LQG adaptive optics control with wind-dependent turbulent models". In: *Adaptive Optics Systems V*. SPIE Astronomical telescopes and intrumentation.

Kelemu, Helawae Friew, Andrew Reeves, Ramon Mata Calvo, Wolfgang Drewelow, and Torsten Jeinsch (2022). "Investigation of advanced control for adaptive optics in free-space optical communication". In: *Environmental Effects on Light Propagation and Adaptive Systems V*. Vol. 12266. SPIE, pp. 51–60.

Kern, Pierre, Pierre Lena, Pierre Gigan, Jean-Claude Fontanella, Gerard Rousset, Fritz Merkle, and Jean-Paul Gaffard (1989). "Come-on: an adaptive optics prototype dedicated to infrared astronomy." In: *Active telescope systems*. Vol. 1114. SPIE, pp. 54–64.

Koepf, G. A., R. G. Marshalek, and D. L. Begley (2002). "Space laser communications: a review of major programs in the United States". In: *International Journal of Electronics and Communications* 56.4, pp. 232–242.

Kolmogorov, Andrey Nikolaevich (1941). "The local structure of turbulence in incompressible viscous fluid for very large Reynolds". In: *Numbers. In Dokl. Akad. Nauk SSSR* 30, p. 301.

Kulcsár, Caroline, Henri-François Raynaud, Cyril Petit, and Jean-Marc Conan (Sept. 2012). "Minimum variance prediction and control for adaptive optics". In: *Automatica* 48.9, pp. 1939–1954. issn: 00051098. doi: 10.1016/j.automatica.2012.03.030.

Kulcsár, Caroline, Henri-François Raynaud, Cyril Petit, Jean-Marc Conan, and Patrick Viaris de Lesegno (2006). "Optimal control, observers and integrators in adaptive optics". In: *Opt. Express* 14.17, pp. 7464–7476. doi: 10.1364/OE.14.007464.

Lainiotis, DG, ND Assimakis, and SK Katsikas (1994). "New doubling algorithm for the discrete periodic Riccati equation". In: *Applied mathematics and computation* 60.2-3, pp. 265–283.

Linnik, P. (1957). "Possibility in principle of weakening the atmospheric effect on a star image". In: *Optika i Spektroskopiya* 57, p. 401.

Looze, D. P., M. Kasper, S. Hippler, O. Beker, and R. Weiss (2003). "Optimal compensation and implementation for adaptive optics systems". In: *Experimental Astronomy* 15, pp. 67–88.

Looze, Douglas P (2009). "Linear-quadratic-Gaussian control for adaptive optics systems using a hybrid model". In: *Journal of The Optical Society of America A-optics Image Science and Vision*. doi: 10.1364/josaa.26.000001.

Mahajan, Virendra N (1981). "Zernike annular polynomials for imaging systems with annular pupils". In: *Journal of the optical Society of America* 71.1, pp. 75–85.

— (1994). "Zernike circle polynomials and optical aberrations of systems with circular pupils". In: *Applied optics* 33.34, pp. 8121–8124.

Maiman, Theodore H. (1960). "Stimulated Optical Radiation in Ruby". In: *Nature* 187.4736, pp. 493–494.

Marquis, Lucas (2023). "High-performance adaptive optics control for the Gran Telescopio Canarias". PhD thesis. Université Paris-Saclay; Universidad de La Laguna.

Marquis, Lucas, Nicolas Galland, Henri-François Raynaud, José Marco de la Rosa, Iciıar Montilla, Oscar Tubio Araujo, Victor Bejar, Marcos Reyes Garcia-Talavera, Gianluca Lombardi, Manuel Huertas Lopez, Sergio Fernandez, Daniel Reverte, Hector de Paz, Alastair G. Basden, and Caroline Kulcsár (2025). "First autonomous full optimal control on a 10-m class telescope: on-sky opening movement on GTCAO". In: *AO4ELT8*.

Marquis, Lucas, Henri-François Raynaud, Nicolas Galland, José Marco de La Rosa, Icíar Montilla, Óscar Tubío Araújo, Marcos Reyes García-Talavera, Gianluca Lombardi, Manuel Huertas Lopez, Daniel Reverte, et al. (2024). "First on-sky tests of LQG control for a 10m-class telescope: prelude on the Gran Telescopio Canarias adaptive optics system". In: *Adaptive Optics Systems IX*. Vol. 13097. SPIE, pp. 1869–1875.

Matsushima, Kyoji and Tomoyoshi Shimobaba (2009). "Band-limited angular spectrum method for numerical simulation of free-space propagation in far and near fields". In: *Optics express* 17.22, pp. 19662–19673.

Maxwell, James Clerk (1865). "A Dynamical Theory of the Electromagnetic Field". In: *Philosophical Transactions of the Royal Society of London* 155, pp. 459–512.

Miller, S.E. and L.C. Tillotson (1966). "Optical transmission research". In: *Proceedings of the IEEE* 54.10, pp. 1300–1311. doi: 10.1109/PROC.1966.5118.

NASA (2019). *NASA Plan for Commercial LEO Development to Achieve a Robust Low-Earth Orbit Economy from which NASA Can Purchase Services as One of Many Customers*. Public Report. NASA.

Noll, Robert J (1976). "Zernike polynomials and atmospheric turbulence". In: *Journal of the Optical Society of America* 66.3, pp. 207–211.

Ogata, Katsuhiko (1995). *Discrete-time control systems*. Prentice-Hall, Inc.

Paschall, Randall N. and David J. Anderson (1993). "Linear Quadratic Gaussian control of a deformable mirror adaptive optics system with time-delayed measurements". In: 32.31, pp. 6347–6358.

Pearson, J. E. (1976). "Atmospheric turbulence compensation using coherent optical adaptive techniques". In: *Applied Optics* 15.3, pp. 622–631.

Perlot, Nicolas, Markus Knapek, Dirk Giggenbach, Joachim Horwath, Martin Brechtelsbauer, Yoshihisa Takayama, and Takashi Jono (2007). "Results of the optical downlink experiment KIODO from OICETS satellite to optical ground station Oberpfaffenhofen (OGS-OP)". In: *Free-Space Laser Communication Technologies XIX and Atmospheric Propagation of Electromagnetic Waves*. Vol. 6457. SPIE, pp. 28–35.

Petit, Cyril, Jean-Marc Conan, Caroline Kulcsár, and Henri-François Raynaud (June 2009). "Linear Quadratic Gaussian control for adaptive optics and multiconjugate adaptive optics: experimental and numerical analysis". In: *JOSA A* 26.6, pp. 1307–1325. doi: 10.1364/JOSAA.26.001307. url: http://josaa.osa.org/abstract.cfm?URI=josaa-26-6-1307.

Petit, Cyril, Jean-Marc Conan, Caroline Kulcsár, Henri-Francois Raynaud, and Thierry Fusco (Jan. 2008a). "First laboratory validation of vibration filtering with LQG control law for Adaptive Optics". In: *Opt. Express* 16.1, pp. 87–97. doi: 10.1364/OE.16.000087.

Petit, Cyril, Thierry Fusco, Julien Charton, David Mouillet, Patrick Rabou, Tristan Buey, Gérard Rousset, Jean-François Sauvage, Pierre Baudoz, Pierre Gigan, et al. (2008b). "The SPHERE XAO system: design and performance". In: *Adaptive Optics Systems*. Vol. 7015. SPIE, pp. 504–515.

Poliak, Juraj, Ramon Mata Calvo, and Fabian Rein (2018). "Demonstration of 1.72 Tbit/s Optical Data Transmission Under Worst-Case Turbulence Conditions for Ground-to-Geostationary Satellite Communications". In: *IEEE Communications Letters* 22.9, pp. 1818–1821. doi: 10.1109/LCOMM.2018.2847628.

Poyneer, L., S Mark Ammons, Mike K Kim, Brian Bauman, Jesse Terrel-Perez, Aaron J Lemmer, and Jayke Nguyen (2023). "Laboratory demonstration of the prediction of wind-blown turbulence by adaptive optics at 8 kHz with use of LQG control". In: *Applied Optics* 62.8, pp. 1871–1885.

Poyneer, Lisa A., Bruce A. Macintosh, and Jean-Pierre Véran (Sept. 2007). "Fourier transform wavefront control with adaptive prediction of the atmosphere". In: *J. Opt. Soc. Am. A* 24.9, pp. 2645–2660. doi: 10.1364/JOSAA.24.002645. url: https://opg.optica.org/josaa/abstract.cfm?URI=josaa-24-9-2645.

Poyneer, Lisa A. and Jean-Pierre Véran (2005). "Optimal modal Fourier-transform wavefront control". In: *J. Opt. Soc. Am. A* 22.8, pp. 1515–1526. doi: 10.1364/JOSAA.22.001515.

Prell, Johannes, Alexandru Duliu, Reeves Andrew, Ilija Hristovski, Shrestha Amita, Florian Moll, and Christian Fuchs (2023). “Optical Ground Station Oberpfaffenhofen Next Generation: first satellite link tests with 80 cm telescope and AO system”. In: *2023 IEEE International Conference on Space Optical Systems and Applications (ICSOS)*. IEEE, pp. 42–48.

Prengère, Léonard, Caroline Kulcsár, and Henri-François Raynaud (2020). “Zonal-based high-performance control in adaptive optics systems with application to astronomy and satellite tracking”. In: *JOSA A* 37.7, pp. 1083–1099.

Primmerman, Charles A., Thomas R. Price, Ronald A. Humphreys, Byron G. Zollars, Herbert T. Barclay, and Jan Herrmann (1995). “Atmospheric-compensation experiments in strong-scintillation conditions”. In: *Appl. Opt.* 34.12, pp. 2081–2088. doi: `10.1364/AO.34.002081`. url: `https://opg.optica.org/ao/abstract.cfm?URI=ao-34-12-2081`.

Proakis, John G. (2001). *Digital Communications*. 4th. McGraw-Hill.

Raynaud, Henri-François and Caroline Kulcsár (2024). “Controller switching with the anti-bump adapter”. In: *European Journal of Control* 80, p. 101116.

Reynolds, Osborne (1883). “XXIX. An experimental investigation of the circumstances which determine whether the motion of water shall be direct or sinuous, and of the law of resistance in parallel channels”. In: *Philosophical Transactions of the Royal society of London* 174, pp. 935–982.

— (1895). “IV. On the dynamical theory of incompressible viscous fluids and the determination of the criterion”. In: *Philosophical transactions of the royal society of london.(a.)* 186, pp. 123–164.

Richardson, Lewis Fry (1922). *Weather Prediction by Numerical Process*. Cambridge: Cambridge University Press.

Robert, Kyliann, Cyril Petit, Geoffrey Maulion, and Thierry Fusco (2025). “Experimental validation of VAR2 LQG-based predictive control for LEO-to-ground optical telecommunications”. In: *JRIOA 2025*.

Roberts, Lewis C, Seth Meeker, Sabino Piazzola, and J Chris Shelton (2019). “Daytime adaptive optics for deep space optical communication”. In: *Laser Communication and Propagation through the Atmosphere and Oceans VIII*. Vol. 11133. SPIE, pp. 49–57.

Roberts, Lewis C, Seth R Meeker, Jonathan Tesch, J Christopher Shelton, Jennifer E Roberts, Santos F Fregoso, Tuan Troung, Michael Peng, Kittrin Matthews, Harrison Herzog, et al. (2023). “Performance of the adaptive optics system for Laser Communications Relay Demonstration’s Ground Station 1”. In: *Applied Optics* 62.23, G26–G36.

Robles, Pablo, Cyril Petit, Jean-Marc Conan, Bouchra Benammar, and Benoit Neichel (2022). “Predictive adaptive optics for satellite tracking applications: optical communications and satellite observation”. In: *Adaptive Optics Systems VIII*. Vol. 12185. SPIE, pp. 917–931.

Roddier, François (1999). *Adaptive Optics in Astronomy*. Cambridge University Press.

Rödiger, Benjamin, Christian Fuchs, Jorge Rosano Nonay, Wolfgang Jung, and Christopher Schmidt (2021). “Miniaturized optical Intersatellite communication terminal–CubeISL”. In: *2021 IEEE International Conference on Communications Workshops (ICC Workshops)*. IEEE, pp. 1–5.

Roux, Brice Le, Jean-Marc Conan, Caroline Kulcsár, Henri-François Raynaud, Laurent M. Mugnier, and Thierry Fusco (2004). “Optimal control law for classical and multiconjugate adaptive optics”. In: *J. Opt. Soc. Am. A* 21.7, pp. 1261–1276. doi: `10.1364/JOSAA.21.001261`.

Saleh, Bahaa E. A. and Malvin Carl Teich (2019). *Fundamentals of Photonics*. 3rd. Hoboken, NJ, USA: Wiley. isbn: 978-1-119-50687-4.

Sasiela, Richard J (2012). *Electromagnetic wave propagation in turbulence: evaluation and application of Mellin transforms*. Vol. 18. Springer Science & Business Media.

Schmerbauch, AEM, MA Vasquez-Beltran, AI Vakis, R Huisman, and B Jayawardhana (2020). “Influence functions for a hysteretic deformable mirror with a high-density 2D array of actuators”. In: *Applied Optics* 59.27, pp. 8077–8088.

Schmidt, Jason D (2010). “Numerical simulation of optical wave propagation with examples in MATLAB”. In: *(No Title)*.

Sinquin, Baptiste, Léonard Prengère, Caroline Kulcsár, Henri François Raynaud, Eric Gendron, James Osborn, Alastair Basden, Jean Marc Conan, Nazim Bharmal, Lisa Bardou, Lazar Staykov, Tim Morris, Tristan Buey, Fanny Chemla, and Matthieu Cohen (Oct. 2020). "On-sky results for adaptive optics control with data-driven models on low-order modes". In: *Monthly Notices of the Royal Astronomical Society* 498.3, pp. 3228–3240. issn: 0035-8711. doi: `10.1093/MNRAS/STAA2562`. url: `https://academic.oup.com/mnras/article/498/3/3228/5897378`.

Sivo, Gaetano, Caroline Kulcsár, Jean-Marc Conan, Henri-François Raynaud, Éric Gendron, Alastair Basden, Fabrice Vidal, Tim Morris, Serge Meimon, Cyril Petit, Damien Gratadour, Olivier Martin, Zoltan Hubert, Arnaud Sevin, Denis Perret, Fanny Chemla, Gérard Rousset, Nigel Dipper, Gordon Talbot, Eddy Younger, Richard Myers, David Henry, Stephen Todd, David Atkinson, Colin Dickson, and Andy Longmore (2014). "First on-sky SCAO validation of full LQG control with vibration mitigation on the CANARY pathfinder". In: *Opt. Express* 22.19, pp. 23565–23591. doi: `10.1364/OE.22.023565`.

Stotts, Larry B, Morio Toyoshima, and Larry C Andrews (2025). "Effect of satellite slew rate on bit error rate model under atmospheric turbulence". In: *Optical Engineering* 64.5, pp. 058104–058104.

Stotts, Larry B. and Larry C. Andrews (2008). "Optical communications in turbulence: a tutorial". In: *Optical Engineering* 47.4, p. 045001. doi: `10.1117/1.2907746`.

Strohbehn, J. W. (2005). "Modern Theories in the Propagation of Optical Waves in a Turbulent Medium". In: *Laser Beam Propagation in the Atmosphere*. Springer, pp. 45–106.

— (1968). "Line-of-sight wave propagation through the turbulent atmosphere". In: *Proceedings of the IEEE* 56.8, pp. 1301–1318. doi: `10.1109/PROC.1968.6572`.

Taara (2024). *Taara Project: High-speed Connectivity Through Light*. Accessed: September 26, 2024. url: `https://x.company/projects/taara/`.

Tatarskii, Valerian Ilitch (1971). "The effects of the turbulent atmosphere on wave propagation". In: *Jerusalem: Israel Program for Scientific Translations, 1971*.

Tatarskij, Valerian Ilich (1961). *Wave Propagation in a Turbulent Medium*. McGraw-Hill Book Comp.

Taylor, Geoffrey Ingram (1938). "The spectrum of turbulence". In: *Proceedings of the Royal Society of London. Series A-Mathematical and Physical Sciences* 164.919, pp. 476–490.

Taylor, L.S. and H. Hodara (1966). "Comments on "Laser wave propagation through the atmosphere"". In: *Proceedings of the IEEE* 54.10, pp. 1461–1462. doi: `10.1109/PROC.1966.5141`.

TESAT (2024). *Kepler Partners with TESAT & Airbus to Develop In-Space Optical Communications Network for HydRON*. Accessed: September 26, 2024. url: `https://www.tesat.de/news/blog/939-kepler-partners-with-tesat-and-airbus-to-develop-in-space-optical-comms-network-for-hydron`.

Tokovinin, Andrei (2002). "From differential image motion to seeing". In: *Publications of the Astronomical Society of the Pacific* 114.800, pp. 1156–1166.

Torre, G. La, S. Raffa, J. Poliak, A. P. Reeves, and I. Hristovski (2024). "A spectral shaping approach to generate power vectors for optical ground-to-space links". In: *Proc. SPIE 13194, Environmental Effects on Light Propagation and Adaptive Systems VII*, 131940N. doi: `10.1117/12.3033903`.

Torres, J. S., A. P. Reeves, C. Kulcsár, H.-F. Raynaud, R. Mata Calvo, and H. F. Kelemu (2022). "Turbulence Characterization of a Free Space Optical Communication Link for High Performance Adaptive Optics Control". In: *Imaging and Applied Optics Congress 2022 (3D, AOA, COSI, ISA, pcAOP)*. Optica Publishing Group, OF2B.2. doi: `10.1364/AOA.2022.OF2B.2`. url: `https://opg.optica.org/abstract.cfm?URI=AOA-2022-OF2B.2`.

Vasko, Christopher A., Pantelis-Daniel Arapoglou, Guray Acar, Monica Politano, Wael El-Dali, Josep Perdigues Armengol, Harald Hauschildt, and Carlo Elia (2022). "Optical High-Speed Data Network in Space - An Update on HydRON's System Concept". In: *2022 IEEE International Conference on Space Optical Systems and Applications (ICSOS)*, pp. 7–13. doi: `10.1109/ICSOS53063.2022.9749744`.

Vidal, F., E. Gendron, and G. Rousset (Oct. 2010). “Tomography approach for multi-object adaptive optics”. In: *Journal of the Optical Society of America A* 27.26, A260000. doi: `10.1364/JOSAA.27.00A253`.

Wallner, Edward P. (1983). “Optimal wave-front correction using slope measurements”. In: *J. Opt. Soc. Am.* 73.12, pp. 1771–1776. doi: `10.1364/JOSA.73.001771`.

White, Frank M. (2003). *Fluid mechanics / Frank M. White*. eng. 5th ed. Boston McGraw-Hill. isbn: 0-07-119911-X.